Exploring structural, electronic, magnetic, and vibrational properties of nanostructures with a scanning tunneling microscope

Dissertation

zur Erlangung des Doktorgrades
der Mathematisch-Naturwissenschaftlichen Fakultät
der Christian-Albrechts-Universität zu Kiel

vorgelegt von
Martin Ziegler

Kiel, 2009

Referent: Prof. Dr. Richard Berndt
Koreferent: Prof. Dr. Stefan Heinze

Tag der mündlichen Prüfung: 27. November 2009
Zum Druck genemigt: 11. Dezember 2009

gez. Prof. Dr. Lutz Kipp, Dekan

Kurzdarstellung

In dieser Arbeit wurde spinaufgelöste und spinintegrierte Rastertunnelmikroskopie (RTM) und -spektroskopie (RTS) verwendet um die strukturellen, geometrischen, elektronischen und vibronischen Eigenschaften nanostrukturierter Objekte in Kontakt mit Festkörperoberflächen zu untersuchen.

RTS Messungen des differentiellen Leitwerts wurden bei konstantem Tunnelstrom und bei konstantem Spitze-Probe Abstand durchgeführt. Diese beiden Betriebsarten für RTS Messungen beeinflussen wesentlich die Linienform, sowie die Position von Signaturen in Spektren und Karten des differentiellen Leitwerts. Für die konstant Tunnelstrom Daten wird eine Normalisierungsverfahren vorgestellt, welches basierend auf den experimentellen Daten zu Informationen über die lokale Zustandsdichte führt.

Unter Verwendung von spinaufgelöster Rastertunnelmikroskopie werden Leitwertmessungen in Einzelatomkontakten vorgestellt, welche aus Kobalt (Co) und Chrom (Cr) Atomen, einem mit Eisen (Fe) bedeckten W(110) Substrat und einer Cr bedeckten Spitze bestehen. Spinaufgelöste Spektroskopie deutet an, dass Co (Cr) Atome ferromagnetisch (antiferromagnetisch) zum Substrat koppeln. Die Einzelatomkontakte zeigen einen klaren Spin-Ventil Effekt, wobei ein höherer Leitwert für eine parallele Anordnung der Magnetisierungen von Spitzen und Atom bestimmt wurde. Desweiteren wird gezeigt, dass sich die Richtung der Magnetisierung von Cr beschichteten Spitzen durch kontrollierten Materialtransfer von der Spitze zur Probe modifizieren lässt. Unter Verwendung des mit zwei Lagen Fe bedeckten W(110) Substrates lässt sich die Spinpolarisation der Spitze durch Spektren und Karten des differentiellen Leitwerts bestimmen. Die somit bestimmten Werte der Spinpolarisation variieren zwischen 0.23 und -0.21.

Unter Verwendung von spinintegrierter Rastertunnelmikroskopie werden elektronische und vibronische Eigenschaften einzelner magnetischer Co Atome adsorbiert auf einer Au(110) Oberfläche vorgestellt. Die Co Atome sitzen in den fehlenden Goldreihen der (2×1) Oberflächenrekonstruktion und zeigen eine Fano-Resonanz in den Spektren des differentiellen Leitwerts am Ferminiveau. Sehr wahrscheinlich ist diese Resonanz eine Folge des Kondo-Effektes mit einer Kondo-Temperatur von (85 ± 5)K. Vibrationsspektroskopie mit einer Au bedeckten W Spitze, an deren Ende ein einzelnes Co Atom sitzt, zeigt bei ± 31 meV die spektroskopische Signatur der *symmetrischen Streckmode*. Bei einer sauberen Au bedeckten W Spitze liegt das Schwingungssignal unterhalb der Detektionsgrenze.

Die Herstellung nanostrukturierter Materialien liefert einen wichtigen Beitrag zum Verständnis magnetischer Eigenschaften auf atomarer Längenskala. Deshalb wurde die rekonstruierte Au(110) Oberfläche als eine Art Schablone zur Herstellung von Co Clustern verwendet. RTM Messungen zeigen kettenartige Co Cluster innerhalb der fehlenden Goldreihen der (2×1) Oberflächenrekonstruktion. Während die Größenverteilung der Co Cluster nach einer Raumtemperaturpräparation stark variiert, wurde nach einer Präparation bei 78 K eine deutlich geringere Größenverteilung der Co Cluster gefunden. Ferner wird gezeigt, dass sich bei 78 K einzelne Co Atome in die Goldreihen der Oberflächenrekonstruktion einbetten. Die experimentellen Ergebnisse werden zusätzlich von Tight-Binding Rechnungen gestützt.

Desweiteren wurde das Adsorbatsystem Ag(111)-Cesium innerhalb dieser Arbeit untersucht. Bei niedrigen Cesium (Cs) Bedeckungen verschwindet stellenweise die atomare Auflösung des Cs Adsorbatgitters. Darüberhinaus verschmieren einzelne Cs Atome zu streifenförmigen Objekten in der Nähe von einatomar hohen Substratstufen. Mit steigender Cs Bedeckung hingegen stellt sich langreichweitig hexagonale Ordnung ein. Die experimentell beobachteten Adsorbatstrukturen konnten mit kinetischen Monte Carlo Rechnungen modelliert werden. Ferner wird gezeigt, dass einzelne Cs Atome eine Resonanz unterhalb des zweidimensionalen Oberflächenbandes induzieren. Durch RTS Messungen und theoretischer Modellierung konnten die wichtigen Beiträge zu der Linienbreite der Resonanz, sowie deren Lebensdauer bestimmt werden. Im Einzelnen sind das resonanter Ladungstransfer, ineleastische Prozesse, sowie Adsorbatvibrationen senkrecht zur Oberfläche.

Abstract

In this thesis spin-resolved and spin-integrated scanning tunneling microscopy (STM) and spectroscopy (STS) are used to explore structural, electronic, magnetic, and vibrational properties of nanostructures on surfaces.

STS of the differential conductance is performed at constant current and at constant distance. These modes of operation significantly affect peak positions and line shapes in spectra as well as patterns in spatial maps of the differential conductance. A normalization procedure for constant-current data, which relies on experimental current-distance data, is shown to yield spectral information on the local density of states.

Using spin-resolved STM the conductance of single-atom contacts comprised of Co and Cr atoms, a Fe-covered W(110) substrate, and Cr-covered tips was investigated. Spin-resolved spectroscopy suggests that Co (Cr) atoms couple ferromagnetically (antiferromagnetically) to the substrate. The single-atom contacts exhibit a clear spin valve effect with higher conductances for parallel alignment of tip and atom magnetizations. Moreover, the magnetization of the chromium-covered tungsten tip was modified by controlled material transfer from the tip to the sample. Using double-layer iron islands on W(110) the spin polarization of the probe was monitored by spectra and maps of the differential conductance and varied between 0.23 and -0.21.

Using spin-integrated STM electronic and vibrational properties of single magnetic Co atoms adsorbed on Au(110) were investigated. Cobalt atoms reside in the missing row of the (2×1) surface reconstruction and exhibit a Fano-type resonance in spectra of the differential conductance at the Fermi level. Most likely this resonance is due to the Kondo effect with a Kondo temperature of (85 ± 5)K. Vibrational spectroscopy with a Au-covered W tip, whose apex was modified by a Co atom showed the spectroscopic signature of the symmetric stretch mode at ± 31 meV. For clean Au-covered tips the vibrational signal stayed below the detection limit.

One of the scientific quest among exploring and understanding magnetic materials at the nanometer scale is to fabricate them. For this reason, the missing row reconstructed Au(110) surface is employed as a template to guide cobalt deposition. Scanning tunnelling microscopy reveals chain-like Co assemblies oriented along the missing row direction. While deposition at room temperature leads to chains with a variety of widths and lengths, deposition at 78 K gives rise to assemblies with a narrow size distribution. At 78 K single cobalt atoms incorporated in the reconstruction rows were resolved providing evidence for an initial stage of surface alloying. Additionally, the experimentally obtained results are modeled with second moment Tight-binding simulations revealing the energetics of various diffusion processes.

Moreover, Cesium adsorption structures on Ag(111) were characterized in a scanning tunneling microscopy experiment. At low coverages, atomic resolution of individual Cs atoms is occasionally suppressed in regions of an otherwise hexagonally ordered adsorbate film on terraces. Close to step edges Cs atoms appear as elongated protrusions along the step edge direction. At higher coverages, Cs superstructures with atomically resolved hexagonal lattices are observed. Kinetic Monte Carlo simulations model the observed

adsorbate structures on a qualitative level. Finally, it is shown that single Cs atoms induce a resonance appearing just below the threshold of the quasi two-dimensional Shockley-type surface-state continuum. Scanning tunneling spectroscopy analysis and theoretical modeling are used to identify the importance of various contributions to the linewidth and to the decay of this resonance: resonant charge transfer, inelastic transitions, and adsorbate vibrations perpendicular to the surface.

Contents

List of publications

The main results of this work have been already published, submitted, or prepared for publications. These publications/manuscripts are to be found in the following sections:

1. Sections 2.4 and 2.5:

   M. Ziegler, N. Néel, A. Sperl, J. Kröger, and R. Berndt,
   Local density of states from constant-current tunneling spectra,
   Phys. Rev. B **80**, 125402 (2009).

2. Section 3.4:

   M. Ziegler, N. Néel, J. Kröger, and R. Berndt,
   Tuning the spin contrast in spin-resolved scanning tunneling microscopy,
   prepared for Appl. Phys. Lett. .

3. Sections 4.2 and 4.3:

   M. Ziegler, N. Néel, J. Kröger, and R. Berndt,
   Spin Valve Effect in Single-Atom Contacts,
   prepared for Phys. Rev. Lett. .

4. Section 5.3:

   M. Ziegler, J. Kröger, and R. Berndt,
   Picking up Vibrations from a Single Magnetic Atom,
   to be published.

5. Sections 7.2 and 7.3:

   M. Ziegler, J. Kröger, and R. Berndt,
   Template-guided formation of cobalt clusters on Au(110),
   to be published.

6. Section 8.2:

   M. Ziegler, J. Kröger, R. Berndt, A. Filinov, and M. Bonitz,
   Scanning tunneling microscopy and kinetic Monte-Carlo investigation of Cesium superlattices on Ag(111),
   Phys. Rev. B **78**, 245427 (2008).

7. Section 8.3:

   M. Ziegler, J. Kröger, R. Berndt, A. G. Borisov, and J. P. Gauyacq,
   Linewidth of a Cesium Adatom Resonance on Ag(111),
   Phys. Rev. B **79**, 075401 (2009).

Chapter 1.

Introduction

The ongoing miniaturization of electronic and magnetic devices requires a consolidated knowledge of physical processes at the nanometer scale. Especially, the quest for an understanding of magnetism at an atomic length scale is a crucial example for this. Since anti- and ferromagnetism in magnetic materials originate from a large number of atoms with unpaired spins, their surface and interface properties increases with a decreasing size of the magnet. Consequently, the shape and solide-state environment of nanoscale systems has an enormous impact on their magnetism.

The continuous decrease of bit sizes in hard disk and memory devices down to today's dimensions is surely a result of the discovery of the giant magnetoresistance effect (GMR) in 1987 by *P. Grünberg and A. Fert* [1, 2]. It describes the electron mobility in magnetic structures consisting of magnetic layers separated by non-magnetic layers. The resulting conductance of such devices depends on the relative magnetization directions of the layer. Hence, by switching the magnetization of the layer the electron current is controlled. One of the most challenging tasks in modern condensed matter physics and material science is to reduce the size of those magnetic structures with the goal to create magnetic devices whose functionality can be engineered at the level of individual atomic spins. The knowledge of spin-polarized transport of electrons through atoms, atomic wires, and molecules is therefore an important step towards this goal. However, transport properties of magnetic single-atom contacts are far from being understood and inconsistent experimental results have been reported [3, 4].

One of the scientific quest among exploring and understanding magnetic materials at the nanometer scale is to fabricate them. This requires a fundamental understanding in how adsorbates interact mutually, with coadsorbates, and with the surface itself. Some central aspects of the growth process can already be gained from *simple* systems. Alkali metals with their single *s* electron at the outermost atomic shell adsorbed on noble metal surfaces are such simple systems. Consequently, for many years much research has been done to explore their structural and electronic properties. [5]

Among a variety of surface sensitive techniques of measurement, which enable to explore structural, electronic and magnetic excitations on surfaces, the invention of the scanning tunneling microscope (STM) [6] gives the opportunity to investigate lateral resolved measurements at the atomic length scale. Moreover, various spectroscopic modes of measurement have been developed to take full advantage of its capabilities (Chapter 2). In addition to the determination of band dispersion curves [7, 8] scanning tunneling spectroscopy (STS) has allowed measurements of electronic state lifetime on clean surfaces [9] as well as spatial localization of molecular orbitals [10].

The advent of spin-polarized scanning tunneling microscopy (SP-STM) allows to resolve magnetic structures at surfaces with an extremely high resolution. [11] In particular, SP-STM uses the tunneling magnetoresistance effect [12, 13], where the tunneling current increases when the the spin-polarizations of, respectively, tip and sample are parallel and

decreases when they are anti-parallel (Chapter 3).

Recently, the spin coupling of individual magnetic atoms [14] and in engineered atomic structures [15] were addressed by inelastic electron tunneling spectroscopy (IETS). Inelastically tunneling electrons whose energy exceeds the energy of a magnetic excitation modify the conductance of the tunneling junction and may give rise to a signal in I-V characteristics (I and V denote tunneling current and voltage, respectively). Originally, with a scanning tunneling microscope IETS was used to probe vibrational excitations of single molecules [16] and, more rarely, of single atoms [17]. According to the current understanding of IETS [18, 19], the vibrational excitation influences the elastic as well as the inelastic tunneling channel. If the related conductance changes happen to compensate, a vibrational signal will be absent in the acquired spectra.

One aim of this thesis is to contribute to the current understanding of magnetism in nanoscale systems. For this reason, spin-resolved and spin-integrated STM are used to explore structural, electronic, magnetic and vibrational properties of nanostructures on surfaces. In detail, this thesis is organized as follows.

To begin with, the basic aspects about scanning tunneling microscopy and spectroscopy are the subject of Chapter 2. In addition to the basic methods to analyze spectroscopic tunneling data a new normalization procedure for experimental data to yield spectral information on the local density of states is presented.

Furthermore, in Chapter 3 the obtained modifications to the apparatus to gain spin resolved contrast are discussed in detail. The capabilities of the SP-STM are tested on the adsorbate system Fe on W(110). Moreover, it is shown that by controlled tip-surface contacts the magnetization of a Cr-covered W tip may be tuned and even reversed.

In Chapter 4 spin-resolved STM and STS are used to investigate magnetic and transport properties of single Co and Cr atoms, which are respectiviley ferromagnetically and antiferromagnetically coupled to the magnetic substrate.

Moreover, a combined electronic and vibrational structure analysis of single Co atoms adsorbed on Au(110) using spin-integrated scanning tunneling microscopy with clean and chemically modified tips is presented in Chapter 5. Spectra of the differential conductance (dI/dV) recorded with a Au-covered W tip atop adsorbed atoms show the spectroscopic signature of the single-Co atom Kondo effect. While with the same tip the spectroscopic signature of the single-Co symmetric stretch mode stayed below the detection limit, Au-covered tungsten tips terminated by a Co atom provided a pronounced vibrational signal.

In Chapter 6 the computational tools are presented, which have been utilized in this thesis. In particular, precise control over the growth processes requires the knowledge of fundamental principles that govern the geometric and electronic structure of surfaces. Consequently, theoretical concepts and computational tools are necessary and relevant to approach a full description of such fundamental principles.

Furthermore, a promising candidate to investigate size- and shape- dependant magnetic properties of atom assemblies at the nanometer scale is presented in Chapter 7. Therein, the (1×2) reconstructed topmost layer of Au(110) is employed as a template to guide Cobalt deposition.

Moreover, in Chapter 8 cesium adsorption structures on Ag(111) were characterized using scanning tunneling microscopy and kinetic Monte Carlo simulations. In particular, the interplay between surface-state mediated interaction and dipole-dipole repulsion will be discussed. Finally, it is shown that single Cs atoms induce a resonance appearing just below the threshold of the quasi two-dimensional Shockley-type surface-state continuum.

Scanning tunneling spectroscopy analysis and theoretical modeling are used to identify the importance of various contributions to the linewidth and to the decay of this resonance.

Chapter 2.

Scanning Tunneling Microscopy and Spectroscopy

Tunneling experiments have been used since the work of Giaever [20] to investigate the density of electronic states. With the advent of scanning tunneling microscopy (STM), [6] tunneling data can be resolved with atomic lateral resolution and various spectroscopic modes of measurement have been developed to take full advantage of its capabilities.

In particular, scanning tunneling microscopy is based on the tunneling effect, which occurs between an atomically sharp tip and the sample separated by a vacuum gap. By applying a voltage between tip and sample a tunneling current can be detected. In quantum mechanics, a current can already be detected in a classical forbidden regime before tip and sample are in contact. This current is held constant using a feedback loop circuit, which varies the tip-surface distance. Therefore, the tip height above the surface is determined by the local geometric, as well as electronic surface structure which allows real space imaging of the surface, when the tip scans the sample.

The principle of operation is already apparent from one-dimensional Wenzel-Kramers-Brillouin tunneling theory. This one-dimensional tunneling model can be used to evaluate spectra of the differential conductance, $\mathrm{d}I/\mathrm{d}V$ (I, V denote tunneling current and voltage, respectively). As $\mathrm{d}I/\mathrm{d}V$ spectra do not directly reflect the spectral local density of states (LDOS), Stroscio *et al.* [23] suggested a normalization procedure where the differential conductance is divided by the conductance. The normalized spectrum of $(\mathrm{d}I/\mathrm{d}V)/(I/V)$, was proposed to be similar to the surface LDOS. Calculations by Lang [24] for alkali atoms on jellium with their broad LDOS features confirmed this proposal. Ukraintsev [26] presented a comparison of various normalization schemes and proposed a normalization, which relies on a tunneling probability function fitted to the spectra. Koslowski *et al.* [27] and later Passoni *et al.* [28] suggested a normalization, which requires additional experimental input data, and yields, in the case of noise-free model data, a rather precise approximation of the LDOS.

The above mentioned normalization schemes are particularly useful in evaluating $\mathrm{d}I/\mathrm{d}V$ spectra, which are recorded at a constant tip–sample distance. [23] However, it can be advantageous to record spectra at constant current, which implies varying distances. For instance, covering a wide range of voltages in a single spectrum is possible, whereas it would require an extreme dynamic range of current when measuring at constant tip-sample distance. Excessive currents during spectroscopy often damage or alter molecules at surfaces. This may be avoided by spectroscopy at constant (and low) current. Moreover, mapping of $\mathrm{d}I/\mathrm{d}V$ simultaneously with recording of a constant-current topograph can be performed conveniently. Similar maps at constant distance are sometimes difficult to achieve when the investigated surface exhibits prominent topographic features. Indeed, a number of recent publications reported constant-current spectra and analyzed these data in terms of peak positions, [29–31] line shapes or band gaps, [29, 32] assuming that constant-current $\mathrm{d}I/\mathrm{d}V$ spectra reflect the density of states. So far, no modeling has been reported to evaluate the validity or precision of this assumption.

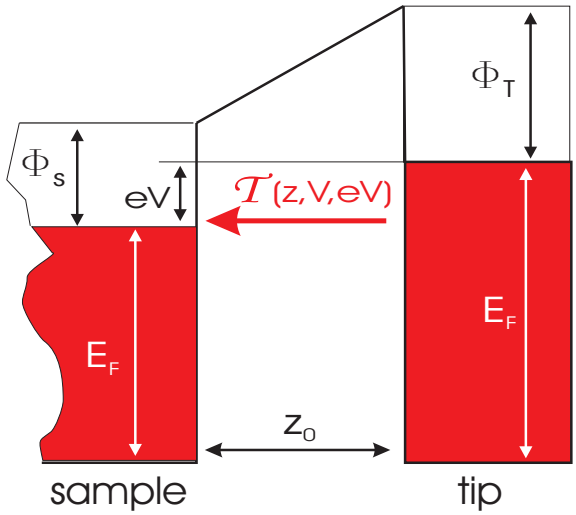

Figure 2.1.: Schematic diagram of the tunneling process between two metallic electrodes separated by a small distance z_0. These electrodes are the STM-tip with a flat ρ_T and the sample with $\rho_\mathrm{S}(E)$. When a bias voltage V is applied to the sample, electrons can tunnel from the tip to the sample with a transmission probability $\mathcal{T}$. Therefore they must overcome a trapezoidal tunneling barrier.

The purpose of this chapter is twofold. First, a short introduction to STM is given [Sec. 2.1 and Sec. 2.2], focusing mainly on the spectroscopic capabilities [Sec. 2.3]. The second part of this chapter deals with the question: How can the LDOS be extracted from spectroscopic measurements at constant-current? The purpose of section 2.4 is to answer this question to some extent. In Section 2.5 the derived normalization scheme is applied to constant current $\mathrm{d}I/\mathrm{d}V$ maps. This chapter closes with a description of contact measurements in Sec. 2.6. A summary of this chapter is given in Sec. 2.7.

2.1. Principles

As already mentioned above the principle of operation of a STM is already apparent from a one dimensional particle-in-a-box model. In particular, tip and sample are described by two ideal metallic electrodes in which the electrons are filled up to the Fermi energy E_F. Figure 2.1 schematically illustrates the two metallic electrodes which are separated by a small distance z_0. When a positive voltage V is applied to the sample the Fermi energies of both electrodes are shifted by eV relatively to each other and a tunneling current can flow through the vacuum barrier between tip and sample. From quantum mechanics the probability for an electron to penetrate the one-dimensional potential barrier of an arbitrary height $V(z)$ can be calculated by the Wentzel-Kramers-Brillouin approximation (WKB) according to

$$\mathcal{T}(z,V,E) = \exp\left\{-\frac{\sqrt{2m}}{\hbar}\int_0^{z_0}\sqrt{(V(z)-E)}\,\mathrm{d}z\right\}, \tag{2.1}$$

where m is the free electron mass and $\hbar$ Planck's constant divided by 2π. Using Simmons model of the tunneling barrier [35], the transmission probability can be estimated for a

trapezoidal tunneling barrier as

$$\mathcal{T}(z,V,E) = \exp\left\{-2\kappa z\right\}, \;\; \kappa = \sqrt{\frac{2m}{\hbar^2}\left(\phi + \frac{eV}{2} - E\right)}, \tag{2.2}$$

with ϕ the average work function from tip and sample. It is quite evident that the transmission probability defines the z resolution of the microscope which reaches the atomic scale. Using realistic values for the work function ϕ in the range of $\approx 4-5\,eV$, κ reaches values around $10\,\mathrm{nm}^{-1}$. For this reason a variation of only 0.1 nm in z leads to the change of one order of magnitude in the tunneling current.

In order to calculate the tunneling current, Bardeen [36] supposed a more realistic model from a many-particle point of view. Therein the two electrodes are described by two many-particles states and the tunneling current itself results from the overlap of their wave functions. Within this model an expression for the tunneling current from tip to sample can express as [37]

$$I = \frac{4\pi e}{\hbar}\int_{-\infty}^{+\infty} \rho_\mathrm{S}(E)\rho_\mathrm{T}(E-eV)\left[f(E-eV) - f(E)\right]\left|M(E-eV,E)\right|^2 \mathrm{d}E, \tag{2.3}$$

where ρ_T and ρ_S are the densities of states from tip and sample, respectively. Moreover, f denotes the temperature dependent Fermi-Dirac distribution for the electrons. While M is the tunneling matrix element, which describes the overlap of the tip wave function with the surface wave function. In principle, the central problem is to calculate the tunneling matrix element.

Using first-order perturbation theory Tersoff and Hamann [21] presented a calculation that gave an analytical result of the matrix element. In particular, the tip is assumed to be atomically sharp and only the last tip atom contributes to the tunneling current. Moreover, this last tip-atom is assumed to exhibit a spherical s-like orbital wave function and only energy conserving elastic tunneling processes are taken into account. The tunneling matrix element can then be written at the position of the tip r_0 as:

$$M = \frac{2\pi C\hbar^2}{\kappa m}\,\Psi_\mathrm{S}(r_0) \tag{2.4}$$

where Ψ_S denotes only the surface wave function and κ is defined as in Eq. (2.2). The tunneling current for the STM can therefore be calculated by using Eq. (2.3)

$$I = \frac{16\pi^3 C^2\hbar^3 e}{\kappa^2 m^2}\,\rho_\mathrm{T}\int_0^{eV} \rho_\mathrm{S}(E)\left|\Psi_\mathrm{S}(r_0)\right|^2 \mathrm{d}E \tag{2.5}$$

with the assumptions that the temperature is nearly zero and the tip density of states ρ_T is a constant over the energy interval of interest. If Ψ_S can be approximated as a plane wave and the tunneling barrier has a trapezoidal geometry, the square of the matrix element,

$$|M|^2 = |\Psi_\mathrm{S}(z)|^2 = |\Psi(z_0)|^2\,\mathrm{e}^{-2\kappa z}, \text{ with } \kappa = \sqrt{\frac{2m}{\hbar^2}\left(\Phi + \frac{eV}{2} - E\right)}, \tag{2.6}$$

can be directly identified with the transmission probability expressed in Eq.(2.2) derived from a simple particle-in-a-box model.

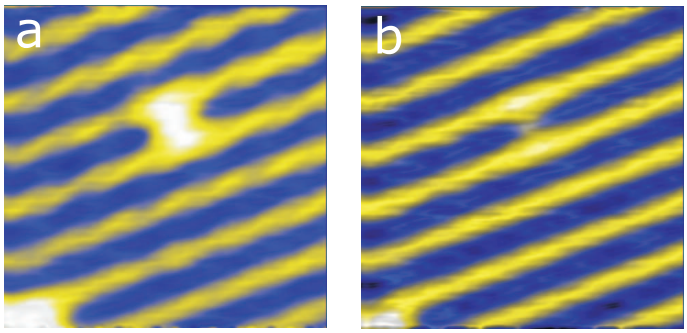

Figure 2.2.: Constant current STM images of a single Co atom at a bias voltage of (a) 60 mV and (b) 20 mV adsorbed onto a Au(110) surface. The scan size of the images is 5 nm × 5 nm and the feedback loop was closed at a current of $I = 0.1$ nA.

2.2. Imaging at the atomic scale

As shown in the last section, the tunneling current can be related to a tip-surface distance z. Moreover, a small variation of 0.1 nm in z results in a difference in one order of magnitude in the value of the tunneling current, which makes STM quite feasible to imaging surfaces at an atomic scale. Thus, when the STM-tip scans at a fixed distance to the sample laterally over the surface a modulation in the tunneling current will be detected. This mode of operation is typically called *constant-height mode*. The advantage of this mode of operation is that the tip can scan fast across the surface. But due to the quite small distances between tip and sample a small roughness of the surface can lead to crash the tip into the sample. Moreover, even small thermical or mechanical instabilities in the experimental setup can result in a tip crash. Hence, this mode of operation is only feasible on flat surfaces, small areas, and low temperatures.

The mode of operation, which ensure quite stable scanning tunneling configuration is called *constant-current mode*. Within this operation mode the tunneling current is hold constant by changing the tip-sample distance z. In order to keep a constant current a feedback loop is used, which adjusts the tip distance by varying the voltage applied to a *piezo-tube* carrying the STM-tip. By recording the change in the piezo-voltage in dependence on the lateral position of the tip a detailed information of the electronic structure of the surface is obtained.

Since the tunneling current is an integral over the local density of states (LDOS) at the tip position, the electronic structure of the tip and the sample is recorded, which makes it sometimes difficult to analyse STM images. One example is given in Fig. 2.2. Here, a single Cobalt atom on the Au(110) surface is imaged in the constant current mode at a bias voltage of 60 mV [see Fig. 2.2(a)] and of 20 mV [see Fig. 2.2(b)]. In the constant current image recorded at 20 mV, the atom seems to have almost disappeared from the scan area compared to the image acquired at 60 mV. By increasing the bias voltage back to 60 mV the atom returns to its place. The explication to this phenomenon is given by the knowledge of the LDOS. Due to a step like increase in the atom LDOS at an energy of ≈ 30 mV [for more details see Chapter 5], the constant LDOS of the bare surface is more important below 30 mV. Since the current is a voltage dependent integral over the LDOS [see Eq. (2.3)], the feedback loop has to adjust the tip closer to the surface to keep the current constant at the position of the atom. This point was early mentioned by Lang [25]

and shows the importance of the knowledge of the LDOS of tip and sample in order to analyse STM images.

2.3. Constant distance spectroscopy

The LDOS of surfaces is a fundamental quantity, which is related to their physical and chemical properties. The STM enables monitoring of the differential conductance $\mathrm{d}I/\mathrm{d}V$, which is related to the LDOS.

Within the one-dimensional model of the tunneling barrier introduced in Sec. 2.1 the tunneling current at a fixed tip-sample distance z and a bias voltage V can expressed as

$$I(z,V) \propto \int_0^{\mathrm{e}V} \varrho_\mathrm{s}(E)\varrho_\mathrm{t}(E-\mathrm{e}V)\mathcal{T}(z,V,E)\mathrm{d}E, \tag{2.7}$$

where ϱ_s and ϱ_t are the local densities of states of, respectively, the sample and the tip, and E denotes the energy of states participating in the tunneling process. While $\mathcal{T}(z,V,E)$ is the transmission factor for a trapezoidal tunneling barrier according to Eq. (2.6). In the following we assume a constant tip density of states. We then obtain for the differential conductance at constant height ($z = z_0 = \mathrm{const}$)

$$\begin{aligned}\frac{\mathrm{d}I(z_0,V)}{\mathrm{d}V} \quad &\propto \quad \mathrm{e}\varrho_\mathrm{s}(\mathrm{e}V)\mathcal{T}(z_0,V,\mathrm{e}V) \\ &\quad + \int_0^{\mathrm{e}V} \frac{\partial\mathcal{T}(z_0,V,E)}{\partial V}\varrho_\mathrm{s}(E)\mathrm{d}E.\end{aligned} \tag{2.8}$$

However, recovering the LDOS from Eq. (2.8) is an intricate task and several procedures have been reported to approximate the LDOS from spectra of $\mathrm{d}I/\mathrm{d}V$ acquired in the constant-height mode [26, 28, 47]. In particular, the second term in Eq. (2.8) is often neglected. But, Koslowski et al. [27] have recently shown that this term may become significant for elevated voltages and can in general not be neglected. Following Ref. [27] the second term in Eq. (2.8) is approximated by applying the generalized mean value theorem for integrals leading to

$$\frac{\mathrm{d}I(z_0,V)}{\mathrm{d}V} \propto \mathrm{e}\varrho_\mathrm{s}(\mathrm{e}V)\mathcal{T}(z_0,V,\mathrm{e}V) - \frac{2\sqrt{2m}\mathrm{e}z_0}{\hbar\sqrt{\phi}}I(V). \tag{2.9}$$

Solving Eq. (2.9) for ϱ_s, the LDOS is obtained from constant-distance spectra.

2.3.1. The Lock-In technique

In order to acquire spectroscopic data with a high signal-to-noise ratio a Lock-In amplifier is used in the experiment. The signal path for a Lock-In amplifier in its essential parts is schematically sketched in Fig. 2.3. In principle, the Lock-In amplifier is based on the mathematical relationship that the product of two sine functions can be written as their sum. To demonstrate this on a simple model system a sinusoidal reference signal (modulation) $V_\mathrm{m} = V_\mathrm{m}^0\cos(\omega_\mathrm{m}t + \phi_\mathrm{m})$ is modulated to a simple sinusoidal signal $V_\mathrm{s} = V_\mathrm{s}^0\cos(\omega_\mathrm{s}t + \phi_\mathrm{s})$ leading to

$$V_\mathrm{m}V_\mathrm{s} = V_\mathrm{r}^0V_\mathrm{s}^0\cos\left[(\omega_\mathrm{m}+\omega_\mathrm{s})t + \phi_\mathrm{m} + \phi_\mathrm{s}\right] + V_\mathrm{r}^0V_\mathrm{s}^0\cos\left[(\omega_\mathrm{s}-\omega_\mathrm{m})t + \phi_\mathrm{s} - \phi_\mathrm{m}\right]. \tag{2.10}$$

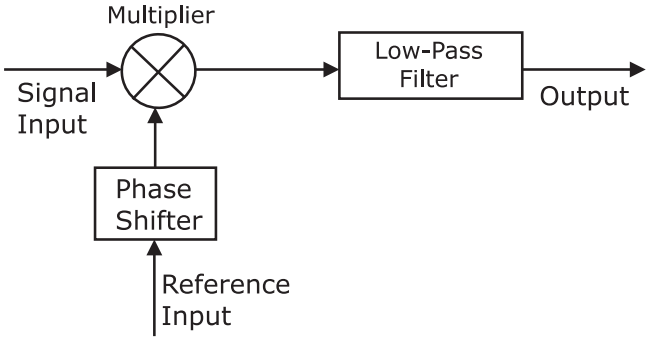

Figure 2.3.: Schematics of a Lock-In amplifier.

In order to eliminate the sum-frequency component a low-pass filter is used, which cuts well below the reference frequency ω_m. Since the cut-off frequency is well below ω_m only signals which lie close to the reference signal can pass the filter. Thus, the presented combination of reference, multiplier, and low-pass filter functions gives a response only to signals in the vicinity of the reference frequency. Moreover, from Eq. (2.10) it is visible that the the Lock-In output signal depends also on the relative phase between the input signal and the reference signal. In the case that both signals are in-phase the output signal of the Lock-In amplifier will reach his maximal value. While for the case of a phase-shift of 90° the output signal will be zero. To gain the output signal a phase shifter is useful to adjust the relative phase between both signals.

Applying a small voltage modulation V_m to the tunneling voltage V leads to an alternating tunneling current $I = I(V + V_\mathrm{m})$. Expanding the tunneling current in a Taylor series by using Eq. (2.7) for the tunneling current with the assumption of a constant transmission factor leads to

$$I(V+V_\mathrm{m}) \propto \underbrace{\int_0^{\mathrm{e}V} \varrho_\mathrm{s}(E)\mathrm{d}E}_{\approx I(V)} + \underbrace{\varrho_\mathrm{s}(eV)}_{\approx \mathrm{d}I/\mathrm{d}V} eV_\mathrm{m}^0 \cos(\omega_\mathrm{m} t + \phi_\mathrm{m}) + \mathrm{O}(\frac{\mathrm{d}^2 I(V)}{\mathrm{d}V^2}). \tag{2.11}$$

It is quite evident that within this approximation the second term corresponds to the first derivative of the tunneling current $I(V)$. Hence, the *first harmonic* of the tunneling current measured with the Lock-In amplifier gives the differential conductance $\mathrm{d}I/\mathrm{d}V$, which is related to the LDOS of the sample as described above.

2.3.2. Broadening in Scanning Tunneling Spectroscopy

Two broadening mechanisms can influence conductance spectra acquired at finite temperature by using the Lock-In amplifier, namely thermal and Lock-In instrumental broadening [65, 66]. Both broadening mechanisms are briefly discussed below.

Thermal Broadening

So far the tunneling current was assumed to be temperature independent. But even a small finite temperature can drastically broaden small spectroscopic features. The thermal broadening of the tunneling current is carried by the Fermi-Dirac function

$$f(E) = \frac{1}{1 + \mathrm{e}^{-E/kT}} \tag{2.12}$$

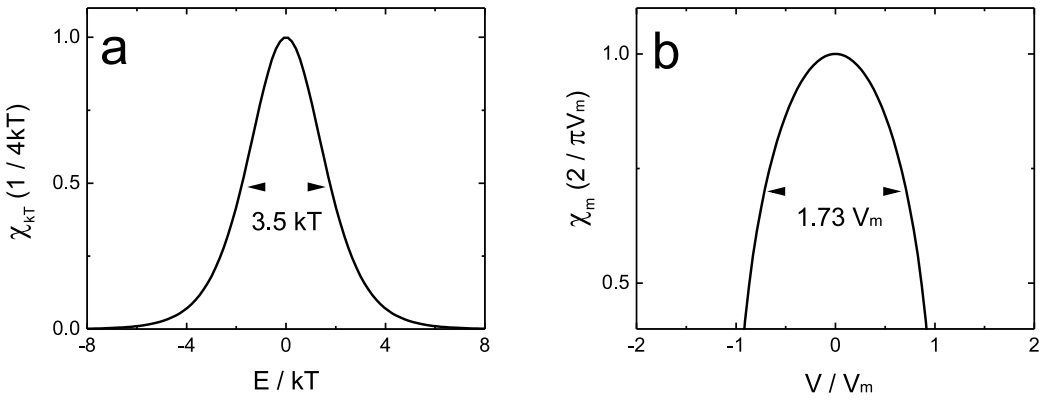

Figure 2.4.: (a) Thermal broadening function, resulting from the temperature dependence of the occupation of electron states. (b) Instrumental broadening associated with the use of a modulating voltage and Lock-In technique.

in Eq. (2.3). Using Eq. (2.8) and assuming a constant tip DOS leads to

$$\frac{\mathrm{d}I(z_0,V)}{\mathrm{d}V} \propto \int_0^{\mathrm{e}V} \varrho_{\mathrm{s}}(E)\,\frac{\beta}{4\left[\cosh(\beta(E-eV)/2)\right]^2}\,\mathrm{d}E, \tag{2.13}$$

where the transmission factor is treated as a constant and $\beta = 1/kT$. The differential conductance $\mathrm{d}I/\mathrm{d}V$ is therefore the convolution of the LDOS of the sample with the thermal broadening function χ_{kT}

$$\chi_{\mathrm{kT}} = \frac{\beta}{4}\cosh^{-2}(\beta(E-eV)/2) \tag{2.14}$$

The broadening function χ_{kT}, shown in Fig. 2.4(a), has a full width at half maximum (FWHM) of 3.5 kT. To give an example, spectra of $\mathrm{d}I/\mathrm{d}V$ acquired at a working temperature of 7K will lead to thermical broading of ≈ 2.1 mV.

Instrumental Broadening

As above mentioned a sinusoidal voltage modulation V_{m} is superimposed on the tunneling voltage V to acquire spectroscopic data with the Lock-In technique. The resulting tunneling current is a function of the time alternating with a frequency ω and the first harmonic is detected as

$$I_{1\omega} = \frac{2}{\tau}\int_0^{\tau/2} I(V + V_{\mathrm{m}}^0\cos(\omega t))\cos(\omega t)\mathrm{d}t. \tag{2.15}$$

Following Ref. [65] the average measurement time τ is chosen without loss of generality so that $\omega\tau = 2\pi$ and $V' = V_{\mathrm{m}}^0\cos(\omega t)$ is substituted as a new variable. Partial integration yields then

$$I_{1\omega} = \frac{1}{\pi V_{\mathrm{m}}}\int_{-V_{\mathrm{m}}}^{+V_{\mathrm{m}}} \frac{\mathrm{d}I}{\mathrm{d}V}(V+V')\sqrt{V_{\mathrm{m}}^2 + V'^2}\,\mathrm{d}V'. \tag{2.16}$$

Hence, the measured voltage is the differential conductivity convoluted with the instrumental function χ_{m},

$$\begin{aligned}\chi_{\mathrm{m}} &= \frac{2\sqrt{V_{\mathrm{m}}^2 - V'^2}}{\pi V_{\mathrm{m}}^2},\ |V'| \leq V_{\mathrm{m}} \\ &= 0,\ |V'| > V_{\mathrm{m}}\end{aligned} \tag{2.17}$$

The FWHM of this instrumental broadening function χ_{m}, shown in Fig. 2.4(b), is $1.7\,V_{\mathrm{m}}$.

In conclusion, the $\mathrm{d}I/\mathrm{d}V$ spectra measured with the Lock-In technique is the double convolution of the LDOS by the thermal broadening function χ_{kT} and by the instrumental function χ_{m}.

2.4. LDOS from constant-current spectra

Often, spectroscopy of $\mathrm{d}I/\mathrm{d}V$ is preferably performed at constant current. In contrast to constant-distance spectroscopy, the tip-sample distance varies. Setting a low and constant current prior to spectroscopy is advantageous for investigating, *e. g.*, the electronic properties of molecules, which may suffer configurational modifications or adsorption site changes due to elevated currents. Recent publications reported on constant-current spectroscopy and physical properties such as band gaps, [32] peak positions, [29–31] or line shapes [29] were deduced from the spectroscopic data. However, the impact of a varying tip-sample distance and a varying voltage on the derived physical properties has not been discussed yet. In this section we wants to fill this gap to some extent.

2.4.1. Model

In the constant-current mode a variation of the tip-sample distance $z(V)$ is allowed to keep the current constant. The derivative of the current with respect to the voltage reads then

$$\begin{aligned}\frac{\mathrm{d}I[z(V),V]}{\mathrm{d}V} \propto\ & \mathrm{e}\varrho_{\mathrm{s}}(\mathrm{e}V)\mathcal{T}[z(V),V,\mathrm{e}V] \\ &+ \int_0^{\mathrm{e}V} \frac{\partial\mathcal{T}[z(V),V,E]}{\partial V}\varrho_{\mathrm{s}}(E)\mathrm{d}E \\ &+ \int_0^{\mathrm{e}V} \frac{\mathrm{d}z(V)}{\mathrm{d}V}\frac{\partial\mathcal{T}[z(V),V,E]}{\partial z}\varrho_{\mathrm{s}}(E)\mathrm{d}E.\end{aligned} \tag{2.18}$$

The third term, which contains $\mathrm{d}z/\mathrm{d}V$, can be discarded since for each voltage $\mathrm{d}I/\mathrm{d}V$ is measured at a given distance, *i. e.*, $\mathrm{d}z/\mathrm{d}V = 0$. Solving then Eq. (2.18) for ϱ_{s} using the approximations introduced in Ref. [27] leads to

$$\varrho_{\mathrm{s}}(\mathrm{e}V) = \frac{1}{\mathrm{e}\mathcal{T}[z(V),V,\mathrm{e}V]}\left\{\frac{\mathrm{d}I[z(V),V]}{\mathrm{d}V} + \frac{\mathrm{e}\alpha z(V)}{\sqrt{\phi}}I_0\right\}, \tag{2.19}$$

where I_0 is the constant current set for the measurements.

Equation (2.19) suggests that the LDOS can be determined from constant-current spectra if $z(V)$ is available. While the absolute distance, $z(V)$, is not known in experiments, measuring a tip excursion, $\Delta z(V)$, is simple and can be done simultaneously with recording $\mathrm{d}I(V)/\mathrm{d}V$. As will be shown below a reference distance z_0 may be estimated to obtain

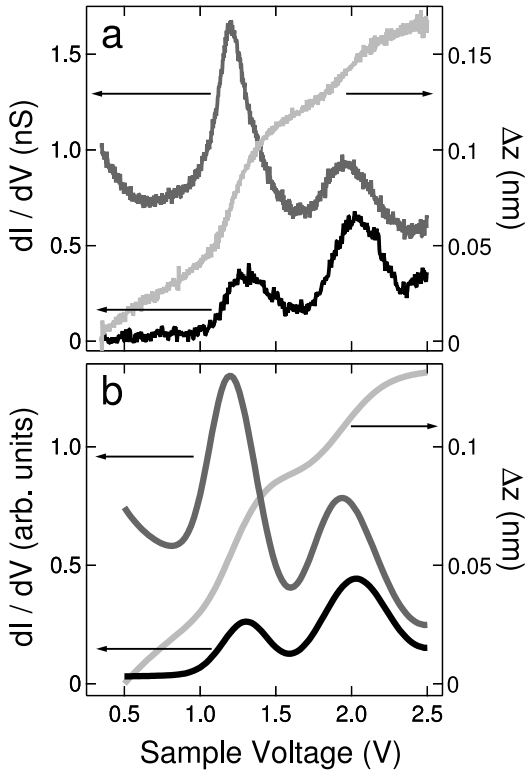

Figure 2.5.: (a) Experimental constant-distance (black) and constant-current (dark gray) $\mathrm{d}I/\mathrm{d}V$ spectra together with displacement curve $\Delta z(V)$ (light gray) atop a single C_{60} molecule on Au(111). The tunneling gap for constant-distance spectroscopy was set at 2.5 V and 1 nA, while 1 nA was used for the constant-current spectrum. (b) Calculated constant-distance (black) and constant-current (dark gray) $\mathrm{d}I/\mathrm{d}V$ spectra and $\Delta z(V)$ (light gray). For the calculations an initial tip-sample distance of 0.6 nm was used. The apparent barrier height $\phi = 7.8\,\mathrm{eV}$ was determined from experimental current-versus-distance data.

$z = z_0 + \Delta z$. To test the validity of this simple approach, we applied Eq. (2.19) to experimental constant-current $\mathrm{d}I/\mathrm{d}V$ data and compared with results from constant-distance spectroscopy. Moreover, we used typical model densities of states to numerically compare both spectroscopy modes. To simulate constant-current $\mathrm{d}I/\mathrm{d}V$ spectra and the displacement of the tip [$\Delta z(V)$ curves], z was varied for a given V until the calculated current $I(z, V)$ deviated from a set, constant value I_0 by less than 0.1 %. In the cases presented below, the normalization is useful in analysing constant-current data despite the significant approximations of the model. However, the scheme is likely to fail when the energy of the tunneling electrons approaches the apparent barrier height ϕ. Furthermore, the electronic structure of the tip is assumed to be featureless.

2.4.2. Peak-shaped spectroscopic features

For a first test experimental spectra of C_{60} molecules adsorbed on Au(111) are used [Fig. 2.5(a)]. The lowest and second-to-lowest unoccupied molecular orbitals (LUMO, LUMO+1) give rise to peaks in constant-current (gray line) as well as in constant-distance

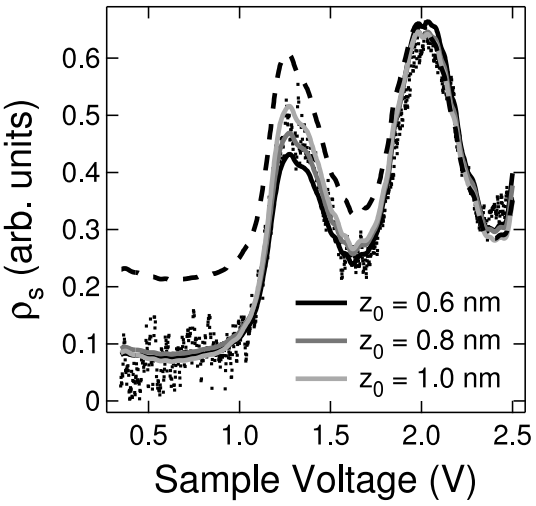

Figure 2.6.: Local density of states of a C_{60} molecule on Au(111) extracted from $\mathrm{d}I/\mathrm{d}V$ spectra at constant distance (dots) using Eq. (2.9) and at constant current for the indicated initial tip-sample distances (solid lines) using Eq. (2.19). The dashed line shows the result of dividing constant-current $\mathrm{d}I/\mathrm{d}V$ data only by the transmission factor (Eq. (2.19) without second term, see also Ref. [33]). An apparent barrier height $\phi = 7.8\,\mathrm{eV}$ was used for the calculations.

(black line) $\mathrm{d}I/\mathrm{d}V$ spectra. [40,41] Compared to the constant-distance data, the constant-current peaks are shifted by $\approx 110\,\mathrm{mV}$ and $\approx 70\,\mathrm{mV}$ toward lower voltages. In addition, the relative amplitudes of the LUMO and LUMO+1 peaks are drastically different in the two spectroscopy modes.

At the low currents used for these measurements, these differences cannot be explained by the influence of the electric field between tip and sample. [281,282] Rather, they are due to the varying tip-sample distance at constant current, which is shown as a light gray line in Fig. 2.5(a). This can be demonstrated as follows. Using experimental constant-distance $I(V)$ and $\mathrm{d}I(V)/\mathrm{d}V$ data, the sample LDOS, ϱ_s, was extracted using Eq. (2.9) and then fitted by a superposition of two Gauss-Lorentz lines. This LDOS was implemented into Eq. (2.7), which was further numerically differentiated to give the calculated constant-distance $\mathrm{d}I/\mathrm{d}V$ spectrum. The result of this procedure is shown in Fig. 2.5(b) as a black line. This optimized model LDOS was used to calculate a constant-current spectrum [gray line in Fig. 2.5(b)] via Eq. (2.7) and its numerical derivative. Figure 2.5(b) also shows the calculated tip displacement at constant current, $\Delta z(V) = z(V) - z_0$, as a light gray line. The calculated curves reproduce the experimentally observed energy shifts and line shapes of the orbital-related spectroscopic signatures. The differences between the constant-current and constant-distance data can therefore be attributed to the displacement of the tip in the course of data acquisition, as expected.

By performing similar simulations for a number of peak shapes and amplitudes, some simple rules were determined: (i) Increasing the width of a single peak leads to a larger shift between the corresponding peaks in constant-current and constant-distance spectra; (ii) an energy-independent background LDOS decreases the shift between these peaks; (iii) two identical LDOS peaks give rise to different peak heights in constant-current spectra. The closer the peaks are, the more will the high-energy peak be attenuated.

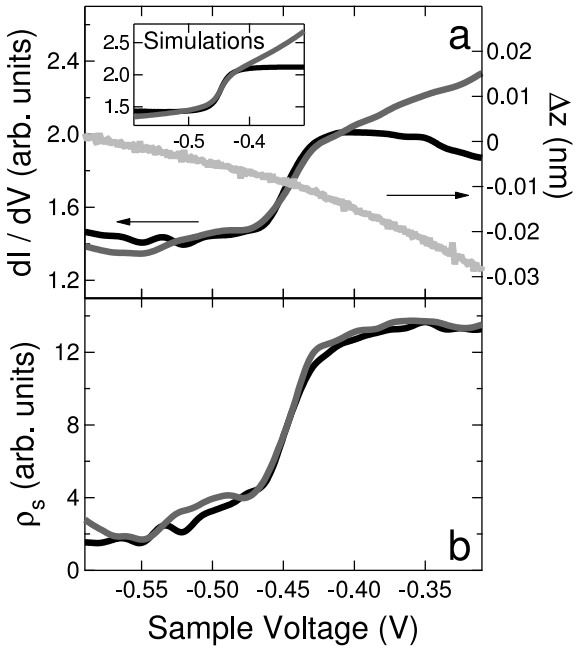

Figure 2.7.: (a) Constant-distance (black) and constant-current (gray) spectra of $\mathrm{d}I/\mathrm{d}V$ of the occupied Cu(111) surface state along with the tip displacement curve (light gray), Δz. The feedback parameters prior to spectroscopy were set to $-0.6\,\mathrm{V}$ and $1\,\mathrm{nA}$. Inset: Simulation of constant-distance and constant-current spectra for a sample LDOS according to Eq. (2.20) with parameters $E_0 = -445\,\mathrm{meV}$, $\Gamma = 24\,\mathrm{meV}$, $\phi = 4\,\mathrm{eV}$, $z_0 = 0.5\,\mathrm{nm}$. (b) Extracted sample LDOS, ϱ_s, from constant-distance and constant-current spectra shown in (a) using Eqs. (2.9) and (2.19).

Figure 2.6 shows a comparison of ϱ_s extracted from constant-distance (dots) and constant-current (lines) spectra, using Eqs. (2.9) and (2.19), respectively. Obviously, both methods lead to similar results. The constant-current data has been treated using three estimates of z_0, extending over a fairly wide range from 0.6 to 1 nm. According to Fig. 2.6 this parameter does not drastically affect the spectral shape. In particular, z_0 affects the heights of the peaks, whereas the peak positions remain almost unchanged. Taking into account only the first term of Eq. (2.19) leads to a strong deviation of the extracted local density of states from the other curves in the low-voltage region (dashed line in Fig. 2.6, 0.5 – 1 V). Consequently, the second term in Eq. (2.19) plays an important role for voltages, which involve a considerable change of the tip-sample distance. It is not sufficient to divide constant-current $\mathrm{d}I/\mathrm{d}V$ data by the transmission factor only.

2.4.3. Step-shaped spectroscopic features

Step-shaped features of the LDOS are often observed from the band edges of electronic surface states, which represent quasi-two-dimensional electron gases. Occupied and unoccupied states lead to different line shapes in constant-current spectra, which will be analysed below.

Occupied surface states occur, *e. g.*, on the (111) surfaces of noble metals. [225] Figure 2.7(a) displays constant-distance (black) and constant-current (gray) spectra of Cu(111)

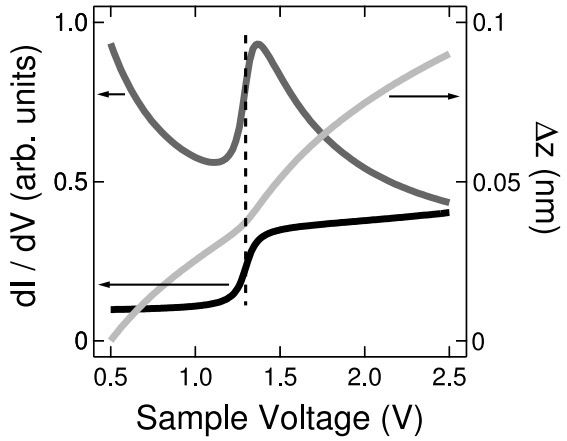

Figure 2.8.: Calculated constant-distance (black) and constant-current (gray) spectrum together with tip displacement characteristics (light gray) for a model LDOS of an unoccupied surface state [Eq. (2.20)]. The dashed line indicates the middle of the step-like onset ($E_0 = 1.35\,\mathrm{eV}$) which coincides with the inflection point of the displacement curve.

along with the tip displacement curve (light gray) acquired simultaneously with the constant-current spectrum. The band edge of this state is located $\approx -445\,\mathrm{meV}$ below the Fermi level and causes the rapid change of the conductance at the corresponding sample voltage. While the constant-distance spectrum is rather flat above this onset, the constant-current signal keeps increasing.

For modeling, the density of states of a two-dimensional electron gas with finite lifetime was used: [45]

$$\varrho_\mathrm{s}(E) = \frac{1}{2} + \frac{1}{\pi}\arctan\left[\frac{2(E-E_0)}{\Gamma}\right] + \varrho_\mathrm{b}. \tag{2.20}$$

E_0 is the energy of the band edge, Γ is proportional to an inverse lifetime and controls the width of the onset, [45] ϱ_b denotes the background LDOS of bulk electronic structure, which is assumed to be constant over the narrow relevant energy range. Calculated spectra are shown in the inset to Fig. 2.7(a) and reproduce the experimental trend.

Figure 2.7(b) compares the LDOS extracted directly using Eqs. (2.9) and (2.19) from the experimental constant-distance spectrum (black) and from the constant-current spectrum (gray). The results show the expected step-like onset and are in good agreement.

For completeness, we also include modeling results for an unoccupied surface state. Figure 2.8 shows calculated constant-current and constant-distance spectra based on a sample LDOS given by Eq. (2.20) with $E_0 = 1.35\,\mathrm{eV}$ and $\Gamma = 0.1\,\mathrm{eV}$. These parameters approximately mimick the unoccupied surface state of Pd(111) as measured by time-resolved two-photon photoemission. [46] The deviations between the constant-distance $\mathrm{d}I/\mathrm{d}V$ spectrum (black) and the constant-current $\mathrm{d}I/\mathrm{d}V$ data (gray) are rather drastic and may be understood by the displacement curve (light gray). As the voltage is increased over the band edge, the tip is rapidly retracted to keep the current constant. As a consequence, the transmission $\mathcal{T}$ is reduced and $\mathrm{d}I/\mathrm{d}V$ decreases. The different appearance of the occupied surface state in Fig. 2.7 is consistent with this interpretation. As the bias is varied from -0.6 to $-0.3\,\mathrm{V}$, the tip approaches the surface. This leads to an increase of $\mathcal{T}$ explaining the observed increase of constant-current $\mathrm{d}I/\mathrm{d}V$ data in this energy range.

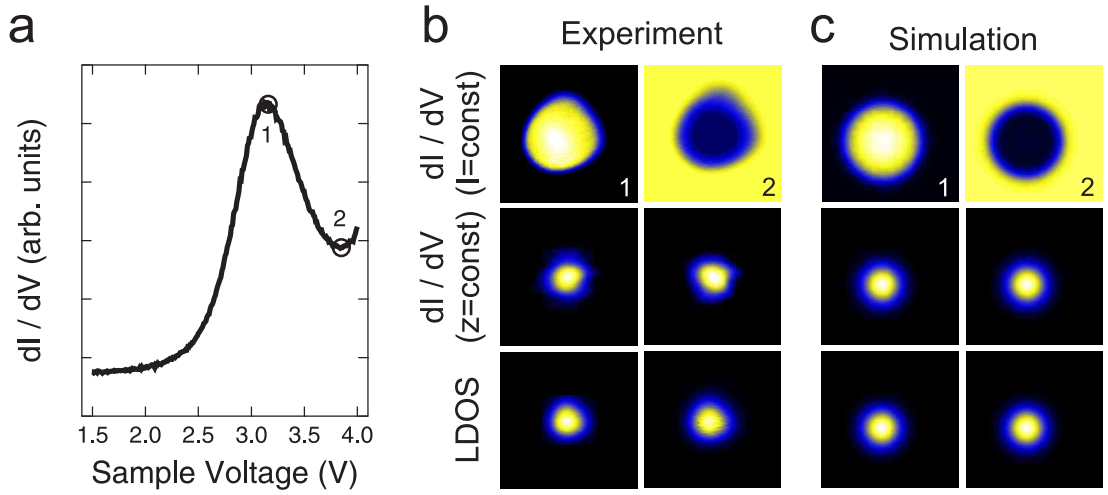

Figure 2.9.: (a) Constant-distance spectrum of $\mathrm{d}I/\mathrm{d}V$ acquired with the tip positioned above the center of a single Ag atom adsorbed on on Ag(111). The circles indicate voltages, at which maps of $\mathrm{d}I/\mathrm{d}V$ were taken. Feedback loop parameters prior to spectroscopy: 4.0 V, 10 nA. (b) Constant-current (top) and constant-distance (middle) $\mathrm{d}I/\mathrm{d}V$ maps acquired at the indicated voltages in (a). The bottom row shows maps of the LDOS extracted from constant-current STM images and $\mathrm{d}I/\mathrm{d}V$ maps using Eq. (2.19). All images have a size of $4\,\mathrm{nm} \times 4\,\mathrm{nm}$ and were taken at 10 nA. For the simulations we used $\Phi = 5\,\mathrm{eV}$, $z_0 = 0.5\,\mathrm{nm}$, $I_0 = 10\,\mathrm{nA}$. (c) Simulations of constant-current (top row) and constant-distance (middle row) $\mathrm{d}I/\mathrm{d}V$ maps based on a model LDOS of a Ag monomer (bottom row, for details see text).

2.5. Maps of the differential conductance

Constant-current mapping of $\mathrm{d}I/\mathrm{d}V$ (or I) has been discussed by Stroscio *et al.* [47,48] and by Berghaus *et al.* [49] Topographic features lead to significant variations of the $\mathrm{d}I/\mathrm{d}V$ signal and complicate the interpretation of the data. In the context of surface state scattering on flat Ag(111) surfaces, Li *et al.* [33] dealt with this problem by normalizing $\mathrm{d}I/\mathrm{d}V$ data using a transmission factor according to the first part of Eq. (2.19). To test the applicability of our normalization procedure to constant-current $\mathrm{d}I/\mathrm{d}V$ mapping at elevated voltages and with appreciable corrugations, we explored the spatial characteristics of the electronic structure of archetypical assemblies on a metal surface, *i. e.*, a single Ag atom and Ag dimer (Ag_2) adsorbed on Ag(111).

It was shown previously that the unoccupied electronic structure of silver clusters on Ag(111) is characterized by sp_z resonances whose energies depend on size and shape of the Ag assemblies. [50] The Ag monomer exhibits an unoccupied state at $\approx 3.1\,\mathrm{eV}$ according to constant-height spectra of $\mathrm{d}I/\mathrm{d}V$ [Fig. 2.9(a)]. In order to analyze the differences between constant-current and constant-distance mapping, $\mathrm{d}I/\mathrm{d}V$ maps are acquired at the indicated voltages depict in Fig. 2.9(a). Maps of $\mathrm{d}I/\mathrm{d}V$ in the constant-current mode are shown in the top row of Fig. 2.9(b), while the obtained constant-distance maps are presented in middle row of Fig. 2.9(b). Two obvious differences between the two data acquisition modes are observed. First the larger spatial distribution of the $\mathrm{d}I/\mathrm{d}V$ signal in constant current data. Taking cross-sectional profiles we found full widths at half

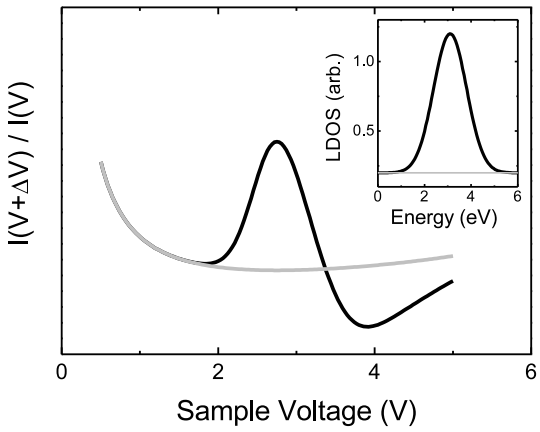

Figure 2.10.: Evolution of I(V+ΔV)/I(V) with the bias voltage for the two LDOS shown in the inset in constant current mode.

maximum ranging from 1.4 to 2.3 nm in constant-current dI/dV maps depending on the applied voltage, while constant-distance dI/dV maps exhibited a full width at half maximum of ≈ 0.8 nm, which was virtually independent of the voltage. The second striking difference is the contrast inversion between the monomer and the surface when the bias voltage is increased in the constant current dI/dV maps [Fig. 2.9(b), 1, 2]. The constant current dI/dV signal of the monomer which is larger than the surface at 3.1 V becomes lower at 3.8 V. Maps of dI/dV acquired in the constant-height mode, however, did not exhibit similar variations. Rather, the appearance of the monomer is virtually identical for all voltages between 2.5 and 5 V and thus reflects the evolution of the LDOS [bottom row in Fig. 2.9(b)], which are extracted using Eq. (2.19) for each point of the STM image. The simulated dI/dV maps for a monomer shown in Figure 2.9(c) reproduce the experimentally observed differences between constant current and constant heights data, thus excluding experimental artefact. The monomer LDOS was modeled by a Gaussian extracted from constant-distance spectra of Fig.2.9(a) using Eq. (2.9), as described in Section 2.4.2 and a background, which was described by an arc tangent function matching the step-like onset of the first image potential state ($E_0 = 4.5$ eV, $\Gamma = 0.6$ eV). The spatial distribution of the monomer LDOS was weighted by a two-dimensional Gaussian riding on a constant background. The resulting spatial distribution of this model LDOS is depicted in the bottom row of Fig. 2.9(c).

To understand the observed differences between constant current and constant distance dI/dV maps, the current evolution with the bias voltage at different positions is required. In constant distance data, only the LDOS differs with the position. Hence, at all voltages the LDOS and, consequently, the current increases when the tip moves from the surface toward the adatom. This implies that the dI/dV signal follows the spatial variations of the LDOS. In contrast, in data acquired at constant current the variations of the tip surface distance ensure a current which is constant at all points inside the scan area. In detail,

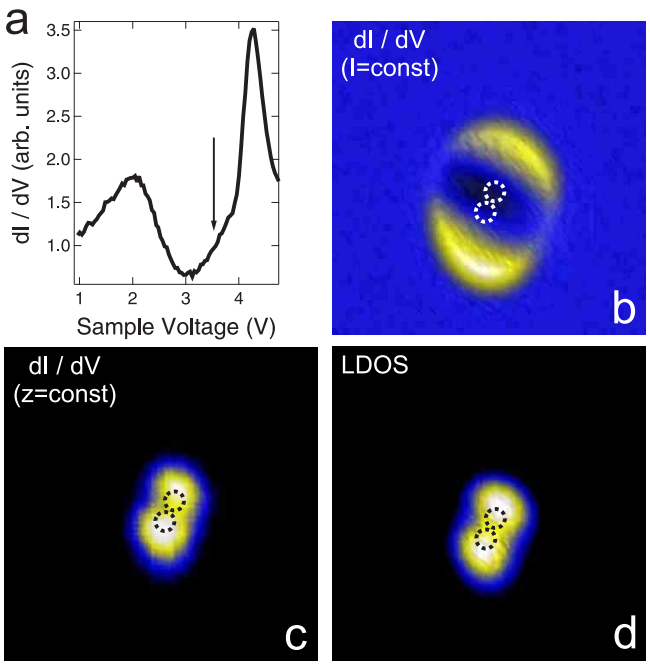

Figure 2.11.: (a) Constant-current (1 nA) spectrum of $\mathrm{d}I/\mathrm{d}V$ acquired at the center of a Ag dimer adsorbed on Ag(111). (b) Constant-current and (c) constant distance map of $\mathrm{d}I/\mathrm{d}V$ recorded at 3.5 V, 1 nA over a 3 nm × 3 nm area. Dashed circles indicate the positions of the dimer atoms. (d) Spatial map of normalized constant-current $\mathrm{d}I/\mathrm{d}V$ for the Ag dimer shown in (b) and (c), which was extracted by using Eq. (2.19) for each image point. An apparent barrier height $\phi = 5\,\mathrm{eV}$ and a tip-sample distance $z_0 = 0.5\,\mathrm{nm}$ were used for the simulations.

the derivative of the current regarding the bias voltage is expressed by

$$\frac{\mathrm{d}I}{\mathrm{d}V} \approx \frac{I(V+\Delta V) - I(V)}{\Delta V}. \tag{2.21}$$

Further in constant current data $I(V) = I_0$ at every tip position, which leads to

$$\frac{\mathrm{d}I}{\mathrm{d}V} = \frac{I_0}{\Delta V} \times \frac{I(V+\Delta V)}{I(V) - 1}. \tag{2.22}$$

Hence, the $\mathrm{d}I/\mathrm{d}V$ signal at various positions depends now on the ratio $I(V+\Delta V)/I(V)$ at all lateral positions. Within this approach the observed contrast inversion in the constant current $\mathrm{d}I/\mathrm{d}V$ maps can be linked to a lower increase of the current with the bias voltage at the adatom than at the surface above a critical voltage. This effect is general for systems which present an additional peak in their LDOS compared to the surface as illustrated in Figure 2.10. Therein a plot of the ratio I(V+ΔV)/I(V) is shown for the two LDOS presented in the inset of Fig. 2.10. The ratio, which is first higher for the peaked LDOS becomes lower above a critical voltage and gives rise to a contrast inversion in the $\mathrm{d}I/\mathrm{d}V$ signal.

Concerning the spatial distribution of the constant current $\mathrm{d}I/\mathrm{d}V$ map the calculations revealed a broadening with the ratio between the adatom LDOS and surface LDOS. For small values of the ratio, the small increase of the LDOS when moving the tip toward

the adatom induces small variation of the tip surface distance, and the constant current $\mathrm{d}I/\mathrm{d}V$ map tends toward constant height $\mathrm{d}I/\mathrm{d}V$ map. For high value of the ratio moving the tip toward the adatom results in large increase of the LDOS and high tip displacement and a much broader spatial distribution of the $\mathrm{d}I/\mathrm{d}V$ signal.

Differences between constant-current and constant-height maps of $\mathrm{d}I/\mathrm{d}V$ become even more spectacular if the electronic structure of a Ag dimer is investigated. In constant-distance $\mathrm{d}I/\mathrm{d}V$ spectra Ag_2 exhibits a sp_z resonance at $\approx 2.4\,\mathrm{V}$, [50] which shifts to $\approx 2\,\mathrm{V}$ in constant-current spectra [Fig. 2.11(a)]. Beyond $\approx 3\,\mathrm{V}$ the $\mathrm{d}I/\mathrm{d}V$ signal increases owing to a field-emission resonance. [51, 52] Within the rise a shoulder around 3.5 V [arrow in Fig. 2.11(a)] is observed, which may be assigned to an antibonding resonance of the dimer. [53] A constant-current map of $\mathrm{d}I/\mathrm{d}V$ acquired at 3.5 V is shown in Fig. 2.11(b). Sickle-shaped maxima are visible at both ends of the dimer, which is oriented along a close-packed direction of the host lattice [dashed circles in Fig. 2.11(b) indicate the positions of the Ag atoms of the dimer]. A constant-distance map of $\mathrm{d}I/\mathrm{d}V$ acquired on the dimer at the same voltage is presented in Fig. 2.11(c). Most obviously, the spatial extension of the dimer signal is strongly reduced compared to the constant-current $\mathrm{d}I/\mathrm{d}V$ map. The centers of the circularly shaped maxima of the $\mathrm{d}I/\mathrm{d}V$ map are $\approx 0.43\,\mathrm{nm}$ apart while for the constant-current $\mathrm{d}I/\mathrm{d}V$ map a distance of $\approx 1.46\,\mathrm{nm}$ is found. Simulations of constant-current and constant-distance $\mathrm{d}I/\mathrm{d}V$ cross-sectional profiles through the dimer along the close-packed Ag(111) direction reproduced these observations. [54] The comparison between constant-current [Fig. 2.11(b)], constant-distance [Fig. 2.11(c)] and normalized constant-current $\mathrm{d}I/\mathrm{d}V$ [Fig. 2.11(d)] maps demonstrates that constant-distance maps of $\mathrm{d}I/\mathrm{d}V$ are more closely related to the sample LDOS, as has been suggested previously. [55] The peculiar pattern in the constant-current $\mathrm{d}I/\mathrm{d}V$ map of the dimer arises from the presence of antibonding states at the edges of the dimer and their absence from its center. For a voltage corresponding to the antibonding state energy, the increase of the LDOS at the dimer edges gives rise to high constant-current $\mathrm{d}I/\mathrm{d}V$ signals at these positions. At the center of the dimer the antibonding state is absent, while the bonding state with an appreciably different energy of $\approx 2\,\mathrm{eV}$ [Fig. 2.11(a), Ref. [53]] is present. As a consequence, the constant-current $\mathrm{d}I/\mathrm{d}V$ signal is even lower than on the Ag(111) surface. [47]

The normalization procedure was likewise used for describing LDOS oscillations resulting from surface state scattering at step edges [33,297] and from confinement to nanostructures. [57, 257, 258, 288] A word of caution is necessary concerning a possible variation of the workfunction, ϕ, which enters as a constant in Eq. (2.19). Comparing current-distance curves acquired on bare Ag(111) and on Ag_2 we found that apparent barrier heights, which can be related at low voltages to ϕ, differ by $\approx 0.5\,\mathrm{eV}$. This deviation is rather small and does not influence the presented results significantly. However, larger deviations of the apparent barrier height have been reported for, *e. g.*, alkali metal atoms adsorbed on metal surfaces [62, 244, 286] and C_{60} molecules, [64] which thus may require spatial maps of ϕ for the normalization procedure.

2.6. Contact measurements

The capability of the STM to form a controlled single-atom contact between the last tip-atom and the sample is a powerful tool to study the electron transport through single atoms, atomic wires, and molecules on an atomic scale. Moreover, the imaging capability of the STM opens the possibility to characterize the contact area before and after the

contact. In this section a brief introduction to STM contact spectroscopy is given. For a detailed review of this topic the reader is referred to Ref. [66].

For macroscopic conductors Ohm's law is applicable to specify electron transport. This model break down in atomic-size conductors, where quantum interference effects influence transport properties. In order to calculate the conductance of a so-called *point contact* (contact whose width is comparable to the Fermi wavelength λ_F) Landauer [67] proposed a model which specifies the transmission probability $|\tau_{ij}|^2$ of an electron in mode i to transmit into mode j according to

$$G = G_0 \sum_{i,j} |\tau_{ij}|^2 , \tag{2.23}$$

where $G_0 = 2e^2/h$ is the quantum of conductance, with $-e$ the electron charge, and h Planck's constant. Following Büttiker [68], the transmission probability can be transformed into a set of eigenchannels $|\tau_{ij}|^2 = T_i \delta_{ij}$, with the assumption that no scattering processes within the quantum point contact can mix the modes $i = 1 \ldots n$. Moreover, the transmission probability will be either 1 or 0, if the cross-section of the contact varies slowly [69]. Hence, by neglecting further finte temperature effects, spin degeneracy, as well as inelastic processes the sum of the transmission probability will be a multiple of G_0.

2.6.1. Conductance-versus-Displacement curves

In order to measure the contact conductance with the STM a linear voltage ramp is applied to the piezo tube, which carries the STM-tip. A a result, the tip is displaced towards the surface, and simulateously the current is recorded. Since the feedback loop was opened prior to spectroscopy, a curve is obtained including conductance values depending on the applied displacement of the tip. While the absolute distance z from the tip to the surface is not known in the experiment, zero displacement is defined for the voltage and the current at which the feedback loop was opened. An example for a conductance-versus-displacement spectrum is presented in Fig. 2.12. This curve is acquired on top of a gold row at the clean Au(110) surface by using an Au covered tip. Following the definition from Ref. [264] the conductance curve can be divided in three parts (labeled as I, II, III in Fig. 2.12).

As the tip is approached towards the surface in the tunneling regime the conductance increases expontially (part I in Fig. 2.12). From spectra taken in the tunneling regime the tunneling barrier can be obtained. By using the above-mentioned one-dimensional description of the tunneling current [Eq. (2.7)] the apparent barrier height ϕ may be extracted from

$$\phi[\mathrm{eV}] = 0.952 \left(\frac{\mathrm{d} \ln I}{\mathrm{d}\, \Delta z[\mathrm{Å}]} \right)^2 \tag{2.24}$$

with the assumptions of a small bias voltage and a constant DOS of tip and sample, and where Δz denotes the tip-displacement in Å.

In part II of the conductance curve the value of conductance increases rapidly, which is linked to the transition from tunneling to contact. As pointed out in Ref. [264] the transition to contact can occur differently. A sharp jump to contact, random in nature, is observed on compact Cu(111) and Ag(111) surfaces, where during the approach the last tip-atom is transferred to the surface. The conductance over single adatoms is found to be reproducible and a smooth transition is observed. This behavior can be understood

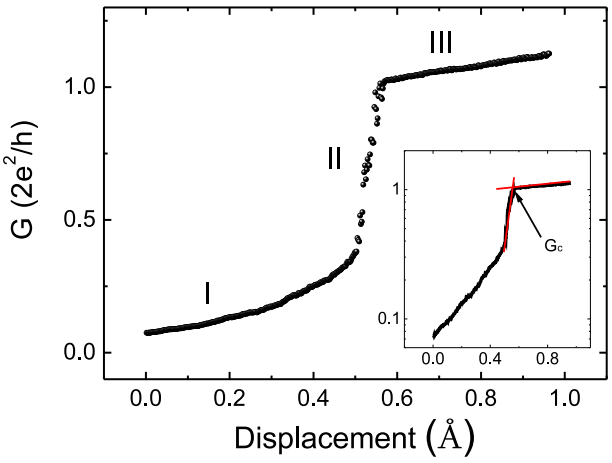

Figure 2.12.: Conductance-versus-displacement curve acquired on top of a gold row at the clean Au(110) surface. The conductance G is plotted in units of the quantum of conductance. The tunneling gap at zero displacement is defined by the feedback parameters of $1\,\mu A$ and $0.18\,V$. Three regimes are denoted in the plot: Tunneling (I), transition (II), contact (III). Inset: The conductance curve is plotted on a logarithmic scale in order to extract the contact conductance G_c, while linear fits to the data in the transition and tunneling regime are used to define G_c according to Ref. [264].

from numerical simulations [264], which predicted a larger stiffness of the adatom bound to the surface as a consequence of the additional dipolar bonding between the adatom and the surface. In sharp contrast, on Au(110) instead of a jump from tunneling to contact a smoother transition is observed with intermediated points between tunneling and contact, where typical no material from the tip-apex are transferred to the surface and therefore the conductance is found to be more reproducible.

Part III of the conductance curve defined the contact regime. Following Refs. [64, 264] the point of intersection between the transition and contact region defines the contact conductance G_c. From the experimental curve a contact conductance of $G_c \approx 1.0\,G_0$ is found. This finding is in good agreement with experiments on Au atoms adsorbed on the Au(111) surface and numerical calculations [66], which predict for the sp_z orbital a transmission probability of ≈ 1. However, it is important to notice that on Au(111) a horizontal plateau builds the contact regime, while a further increase in the conductance value in contact is observed on the (110) facet of Au. Since both surface orientations are chemically identic, the observed difference originates most likely from crystallographic differences.

2.7. Summary

In conclusion, a brief introduction to the principle concepts of scanning tunneling microscopy and spectroscopy was given in this chapter. Since the focal points of this thesis are obtained with the help of spectroscopic measurements, the measurement technique

and the physical interpretation of the acquired data are discussed in detail.

Furthermore, the advantage to record spectra at constant current, which implies varying tip sample distances, are discussed. In particular, constant-current $\mathrm{d}I/\mathrm{d}V$ spectra are assumed to reflect the density of states. However, no modeling has been reported to evaluate the validity or precision of this assumption so far. In this chapter this gap was filled to some extent. It was found that spectra of $\mathrm{d}I/\mathrm{d}V$ at constant current can be used to obtain information about the LDOS of structures at surfaces. The excursion of the tip during constant-current data acquisition leads to significant deviations compared to constant-distance data. A simple normalization scheme was proposed, which takes into account experimental current-distance characteristics. For a number of density of states features, which are often observed in experiments, the normalization yields a quantity which is close to the LDOS.

Chapter 3.

Spin-polarized Scanning Tunneling Microscopy

Observing and controlling of magnetism at the atomic length scale is undoubtedly crucial for the understanding of nanomagnetism and for the design of future magnetic media and devices. Consequently, soon after the invention of the scanning tunneling microscope the possibility to make the STM tip sensitive to the spin of tunneling electrons was discussed [71]. In fact, SP-STM uses the *tunneling magnetoresistance effect* (TMR) [12, 13], where the tunneling current increases when the the spin-polarizations of respectively tip and sample are parallel and decreases when they are anti-parallel. In a first experimental investigation by Wiesendanger et al. [11] in 1990 spin-selectivity has been obtained by using tips manufactured of ferromagnetic materials, which exhibits an intrinsic spin-polarization at the Fermi level. Alternatively, the use of semiconducting tips has been proposed [71]. By irradiation a GaAs tip with circularly polarized light the spin-orbit splitting at the Γ-point of the valence band can be used to populate conductance bands with spin-polarized electrons [72]. Therefore it seems to be rather straightforward to realise SP-STM investigations. However, it took about 15 years until SP-STM became a mature technique [80]. In particular, it was found that by choosing the appropriate material for the magnetic film of a coated W tip, sensitivity to either the in-plane or perpendicular magnetization component of the sample can be achieved [80, 83].

At present spin-resolved scanning tunneling microscopy and spectroscopy are the only techniques, which enable the investigation of the magnetic structure of surfaces at the atomic scale. Such a performance relies to a major extent on the quality of the spin-polarized probe, which has to be characterized using a surface with defined magnetic properties. An *in situ* optimization of the spin contrast by a controlled modification of the probe status is therefore highly desirable. Further, to discriminate magnetic from electronic properties the *in situ* magnetization reversal of the probe would be extremely helpful, in particular if applying external magnetic fields is not part of the experimental setup.

This chapter begins with a summary of the main aspects of spin-polarized STM by focusing mainly on the for this thesis important aspects. Subsequently, we present that the magnetization of a chromium-covered tungsten tip can be modified and even reversed by controlled material transfer from the tip to the sample. In detail, in Sec. 3.1 the milestones in spin-polarized tunneling are presented. In Sec. 3.2 the general principle behind SP-STM, as well as the basic aspects in the design of spin-polarized tips focusing mainly on suitable tip materials are discussed. Furthermore, in Sec. 3.2.2 the obtained modifications of the apparatus to realize a spin polarized scanning tunneling microscope are discussed. In order to proof the capabilities of the SP-STM the well characterized system of Fe layers on W(110) has been investigated and results are presented in Sec. 3.3. Finally, Sec. 3.4 is dealing with the tuning of the magnetization of a chromium-covered tungsten tip.

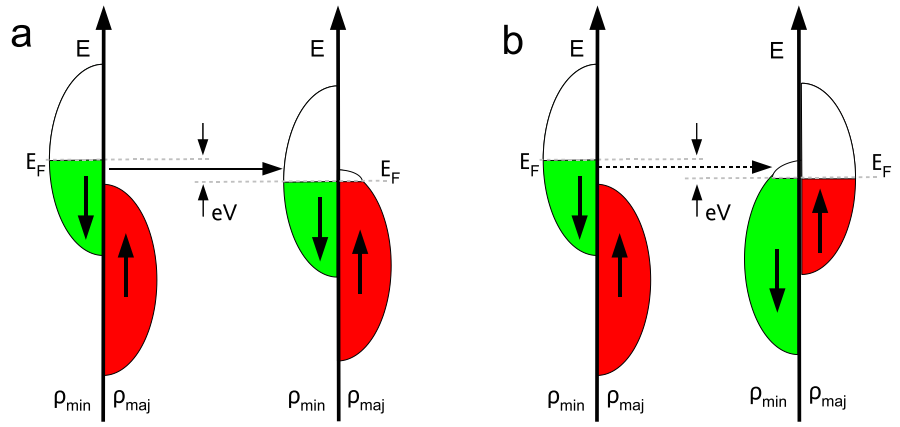

Figure 3.1.: Principle of spin-polarized tunneling between magnetic electrodes in the case of a parallel (a) and an antiparallel orientation of their magnetization axes. Since the spin is conserved during the tunneling process, spin-up electrons that tunnel out of the occupied states of the first electrode can only enter empty spin-up states of the second electrode. Hence, the tunneling current is smaller in the case of an antiparallel orientation as in the case of a parallel orientation.

3.1. Basic aspects

Ferromagnetic materials (*i.e.* Co, Ni, Fe) can be characterized by their spontaneous magnetisation, which appears without a magnetic field below a critical point, the so-called *Curie-temperature* T_C. The underlaying physics can be understood in the framework of the model of a nearly free electron gas, if we allow that the electron bands can spontaneously split into bands of up and down spins electrons according to

$$E(\mathbf{k}) = \frac{\hbar^2 \mathbf{k}^2}{2m^*} + \begin{cases} +\Delta\ n^{\uparrow}/n \\ -\Delta\ n^{\downarrow}/n \end{cases}, \tag{3.1}$$

where Δ denotes the Stoner parameter which is a measure of the strength of the exchange correlation and $n = n^{\uparrow} + n^{\downarrow}$ is the number of electrons. This formalism has been predicted by Stoner [73]. In particular, Stoner shows that the partition of spin up and spin down electrons in different bands which are energetically shifted to each other is fulfilled, if the relative gain in exchange interaction (the interaction of electrons via the Pauli exclusion principle) is larger than the loss in kinetic energy. Therefore, the ground state of a metal can be described by the relative number of spin up $n^{\uparrow}$ and spin down $n^{\downarrow}$ electrons. In fact, there is a larger number of electrons from one spin direction in magnetic metals. For this reason, it makes sense to differentiate between minority and majority electrons. By summing the above mentioned formula for $E(\mathbf{k})$ over all wave vectors $\mathbf{k}$ a criterion for ferromagnetism can be established as $\rho(E_F)\Delta > 1$, where $\rho(E_F)$ is the density of states at the Fermi energy.

With the help of the Stoner model it can be easily recognized that the value of the tunneling current in a tunneling experiment which use ferromagnetic electrodes should depend on the relative orientation of the magnetization axes of the electrodes, as schematically represented in Fig. 3.1. Since due to the Stoner model the density of states at the Fermi energy depends on the spin orientation, the spin-polarization at the Fermi energy

can be described as

$$P(E_\mathrm{F}) = \frac{\rho^\uparrow(E_\mathrm{F}) - \rho^\downarrow(E_\mathrm{F})}{\rho^\uparrow(E_\mathrm{F}) + \rho^\downarrow(E_\mathrm{F})}, \tag{3.2}$$

where $\rho^\uparrow$ and $\rho^\downarrow$ are the density of states of majority and minority electrons, respectively. In fact, this simple model requires some assumptions, which are complied when the tunneling process of spin up and spin down electrons can be regarded as independent and no spin flip occurs during the tunneling process. Indeed, it turned out that the tunneling current must be dominated by elastic processes. However, it is important to note that experimental obtained values and therotical calculated values can differ due to the fact that electrons from different bands can unequally contribute to the tunneling current. Steans argues that especially strong localized bands with a higher effective mass only weakly contribute to the tunneling current and can therefore be neglected [74]. It is therefore useful to describe the spin-polarization at the Fermi level by the wave vectors **k** of respectively minority and majority electrons rather than by their density of states.

In pioneer experimental works by Tedrow and Mersevey [12] and later Julliere [13] spin-polarized tunneling through planar junctions were successfully performed. In particular, the tunneling resistance in such junctions are found to be dependent from the relative orientation of both electrodes to each other, where the resistance is smaller in the case of a parallel orientation than in the antiparallel case. This effect is usually called tunneling magnetoresistance (TMR) and can be described by

$$R_\mathrm{TMR} = \frac{R_{\uparrow\downarrow} - R_{\uparrow\uparrow}}{R_{\uparrow\uparrow}}, \tag{3.3}$$

where $R_{\uparrow\downarrow}$ ($R_{\uparrow\uparrow}$) are the resistance in the case of a parallel (antiparallel) orientation of both electrodes. In order to describe this experimental observation Julliere introduced a simple *two-channel* model [13], which assumes that the conductivity of the junction at zero bias is proportional to the product of the spin dependent density of states and can be written as

$$\frac{\mathrm{d}I}{\mathrm{d}V} \propto \rho_\mathrm{S}^\uparrow(E_\mathrm{F})\rho_\mathrm{T}^\uparrow(E_\mathrm{F}) + \rho_\mathrm{S}^\downarrow(E_\mathrm{F})\rho_\mathrm{T}^\downarrow(E_\mathrm{F}), \tag{3.4}$$

where $\rho_{\mathrm{T(S)}}$ denotes the density of states of the ferromagnetic electrodes of the junction (*i.e.* tip and sample). In order to extract the spin polarization of the junction Eq. (3.2) is inserted in Eq. (3.3) leading to

$$R_\mathrm{TMR} = \frac{2P_\mathrm{T}P_\mathrm{T}}{1 + P_\mathrm{T}P_\mathrm{T}}. \tag{3.5}$$

The TMR-ratio is therefore an intrinsic property of the ferromagnetic electrodes, whereby characteristics of the tunneling barrier are not taken into account. At this point a more detailed analysis of the TMR-ratio including characteristics of the tunneling barrier has been done by Slonczewski [75] and later by Bratkovsky [76].

3.2. Spin-polarized tunneling with the STM

The aim of this section is twofold: First, we want to discuss the general principle behind SP-STM, as well as the basic aspects in the design of spin-polarized tips focusing mainly on suitable tip materials. For a detailed review on this topic the reader is referred to [77]. Secondly, the obtained modifications of the apparatus to realize a spin polarized scanning tunneling microscope are presented.

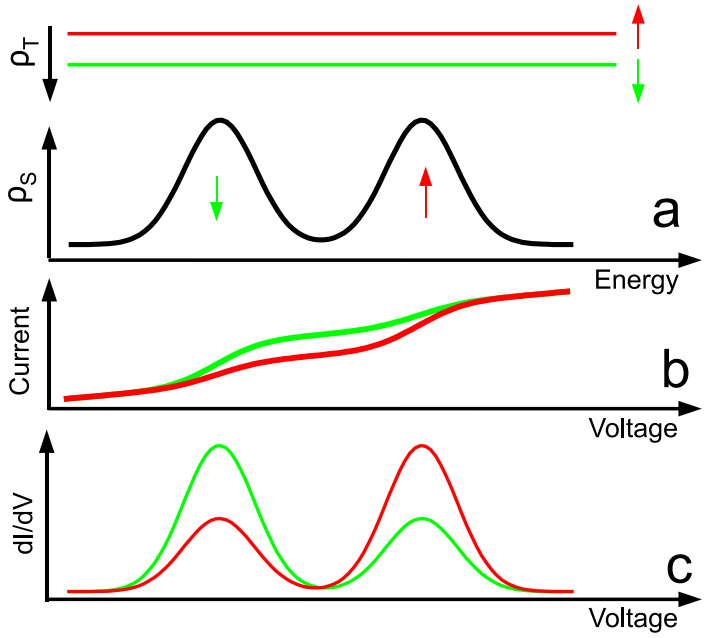

Figure 3.2.: The principle behind SP-STM: (a) For the illustration a model sample DOS with an exchange-split surface-state and a tip with a constant spin polarization is used, where two spin polarisations of the tip are assumed [*up* (red) and *down* (green)]. (b) Due to the spin value effect the tunneling current increases when the spin-polarizations of respectively tip and sample are parallel and decreases when they are anti-parallel. (c) At the positions of the sample surface-state this leads to a reversal in the $\mathrm{d}I/\mathrm{d}V$ signal.

3.2.1. SP-STM using magnetic probe tips

SP-STM uses the above mentioned phenomena that the tunneling current increases when the spin-polarizations of respectively tip and sample are parallel and decreases when they are anti-parallel, as schematically presented in Fig. 3.2. In a pioneering contribution by Pierce [71] the use of ferromagnetic tips in order to reach magnetic sensitivity was already discussed in 1988.

The general principle behind SP-STM is the same as for spin integrating STM, which has been described at length in Sec. 2.1. If we consider that in SP-STM, both spin up and spin down channels will contribute to the total tunneling current, the tunneling current at a tip-sample distance z and a bias voltage V can be expressed in the limit of very low temperatures ($T \to 0$) as

$$I(z,V) \propto \int_0^{eV} \left(\rho_{\mathrm{S}}^{\uparrow}(E)\rho_{\mathrm{T}}^{\uparrow}(E-eV) + \rho_{\mathrm{S}}^{\downarrow}(E)\rho_{\mathrm{T}}^{\downarrow}(E-eV)\right) \mathcal{T}(z,E,V)\,\mathrm{d}E, \tag{3.6}$$

where $\rho_{\mathrm{S}}^{\uparrow(\downarrow)}$ and $\rho_{\mathrm{T}}^{\uparrow(\downarrow)}$ are the spin up (spin down) LDOS of, respectively, the sample and the tip, E denotes the energy of states participating in the tunneling process, and $\mathcal{T}(z,E,V)$ is the transmission factor as defined in Sec. 2.1. From this equation it is clear that the tunneling current is the sum of the convolution of the spin up LDOS of sample and tip plus the convolution of the spin down LDOS of sample and tip. Hence, what is really being measured in SP-STM is a quantity proportional to the convolution integrated non-

spin-polarized and spin-polarized LDOS of sample and tip. Consequently, it is not always feasible to separate spin-polarized from non-spin-polarized contributions to the overall tunneling current.

However, Wortmann et al. [78] have shown in a theoretical investigation, that the tunneling current can be separated in a non-spin-polarized current I_0 and in a spin-polarized current I_{SP} according to

$$\begin{aligned} I(\mathbf{r}_{\mathrm{T}}, V, \theta) &= I_0(\mathbf{r}_{\mathrm{T}}, V) \; + \; I_{\mathrm{SP}}(\mathbf{r}_{\mathrm{T}}, V, \theta) \\ &\propto \rho_{\mathrm{T}} \tilde{\rho}_{\mathrm{S}}(\mathbf{r}_{\mathrm{T}}, V) + m_{\mathrm{T}} \tilde{m}_{\mathrm{S}}(\mathbf{r}_{\mathrm{T}}, V), \end{aligned} \tag{3.7}$$

where ρ_{T} is the non-spin-polarized LDOS at the position of the tip $\mathbf{r}_{\mathrm{T}}$, $\tilde{\rho}_{\mathrm{S}}$ is the energy integrated LDOS of the sample, and $\mathbf{m}_{\mathrm{T}}$ and $\tilde{\mathbf{m}}_{\mathrm{S}}$ are the corresponding vectors of the spin-polarization of the LDOS. The latter is given by an energy integral of the local magnetization DOS, $\mathbf{m}_{\mathrm{S}}$:

$$\tilde{m}_{\mathrm{S}}(\mathbf{r}_{\mathrm{T}}, V) = \int_0^{eV} \mathbf{m}_{\mathrm{S}}(\mathbf{r}_{\mathrm{T}}, E)\, \mathrm{d}E, \tag{3.8}$$

with

$$\mathbf{m}_{\mathrm{S}}(\mathbf{r}_{\mathrm{T}}, E) = \sum_{\mu} \delta(E_\mu - E) \mathbf{\Psi}^{\dagger}(\mathbf{r}_{\mathrm{T}}) \sigma \mathbf{\Psi}(\mathbf{r}_{\mathrm{T}}), \tag{3.9}$$

where $\mathbf{\Psi}$ denotes the spinor of the sample wave function and σ is Pauli's spin matrix.

In a pioneering experimental investigation by Wiesendanger et al. [11] spin-polarized imaging of the Cr(001) surface with the STM was successfully performed. In particular, the Cr(001) surface was theoretically predicted to be a topological antiferromagnet [79] resulting in a non uniform step height between adjacent surface terraces. By applying the constant current mode of the STM in order to imaging the Cr(001) surface Wiesendanger et al. found a uniform step height of 0.14 nm by using a W tip, but two different apparent step heights of 0.12 nm and 0.16 nm, alternately, when a CrO_2 ferromagnetic tip was used in the experiment.

It was not all clear why spin-polarized tunneling could be performed successfully, since the magnetic corrugation is assumed to be very small compared to the geometrical corrugation of most surfaces. Moreover, the SP-STM is only sensitive to the energy-integrated local magnetization DOS $\tilde{\mathbf{m}}_{\mathrm{S}}$, which can lead to a reduction of I_{SP} if the spin polarization of the relevant electronic states changes their sign within the voltage interval between the Fermi level and the applied bias voltage. However, Wortmann et al. [78] have been shown that the STM allows to make images of even complicated periodic surface spin structures, if the constant-current mode is used in the experiment. This can be understood by regarding the 2D Fourier expansion of the change in the tunneling current with respect to the reciprocal surface lattice. In particular, any magnetic superstructure lowers the translational symmetry, where especially smaller reciprocal lattice vectors become relevant. In the constant current mode the change in the tip-sample distance is determined by the corresponding exponential change in the tunneling current, where it can be shown that their Fourier expansion coefficient decays exponential in lateral direction with increasing length of the reciprocal lattice vector [78]. Therefore the tunneling current is dominating from the smallest nonvanishing reciprocal lattice vectors, where the contributions of the spin-polarized part are exponentially larger than those of the unpolarized part. As a result the constant current SP-STM images reflect the magnetic superstructure of the surface.

In order to overcome the difficulties of separating topographic and magnetic information the local differential conductance $\mathrm{d}I/\mathrm{d}V$ has to be measured. By using Eq. (3.7) the differential conductance can be calculated as

$$\mathrm{d}I/\mathrm{d}V(\mathbf{r}_\mathrm{T}, V) \propto \rho_\mathrm{T}\rho_\mathrm{S}(\mathbf{r}_\mathrm{T}, V) + m_\mathrm{T}m_\mathrm{S}(\mathbf{r}_\mathrm{T}, V). \tag{3.10}$$

As described in Sec. 2.3 for non-magnetic tips, spectra of $\mathrm{d}I/\mathrm{d}V$ can be acquired by fixing the tip-sample distance, superimposing a sinusoidal voltage modulation on the sample voltage and measuring the current response with a lock-in amplifier. Indeed, this method allows to measure spectra corresponding to the energy resolved LDOS as long as the applied voltage is sufficiently small compared to the substrate work function.

Constant-current mapping of $\mathrm{d}I/\mathrm{d}V$ are typically used to resolve lateral magnetic superstructures on the surfaces. For instance, in a first experiment the lateral magnetic structure of Gd(0001) thin films are resolved with this method [80]. It is often noticed that maps of $\mathrm{d}I/\mathrm{d}V$ recorded at constant current display the magnetic structure of the surface. However, it is important to recognize that in Eq. (3.10) the tunneling coefficient is assumed to be constant within the applied voltage interval. Concerning our analysis of $\mathrm{d}I/\mathrm{d}V$ maps recorded at constant current for non-magnetic tips the validity or precision of this assumption is generally not fulfilled and the influence of the change in the transmission probability due to the varying tip-sample distance has to be taken into account (see discussion in Sec. 2.4). Moreover, additional variation of spin-average surface electronic properties can also lead to contrast differences in spin-polarized measurements. For this reason, measurements with non-magnetic tips have to be performed additionally in order to identify the difference between magnetic and electronic properties clearly.

3.2.2. Tip design

The tip for SP-STM has an important function, since it must fulfill various conditions: First of all, the ideal SP-STM tip has to exhibit a high spin-polarization, which ensures a good signal-to-noise ratio. Secondly, stray fields, as i.e. created by dipolar interaction between tip and surface atoms, have to be as low as possible in order to not influence the sample's intrinsic magnetic structure. Thirdly, a possibility to reverse the magnetization direction is useful in order to separate magnetic from electronic and topographic contributions. Finally, it is necessary to control the orientation of the magnetization direction of the tip to be sensitive to the spin-polarization of magnetic structures of the sample.

After first SP-STM investigations at air with rather inert tip materials, like CrO_2 [11], which are used to avoid contermination problems, Wiesendanger et al. used tips from polycrystalline bulk materials [81] into UHV systems. In particular, bulk tips are manufactured easily and rather robust against tip crashes and contaminations since these tips have enough material to be recovered by voltage pulse procedures, or controlled tip-surface contacts. However, in view of stray field minimization bulk tips made of ferromagnetic 3d transition metals are an unfavorable choice, since their high saturation magnetizations are destined to create a magnetic stray field, which cannot be neglected.

In order to estimate the magnitude of the expected magnetic stray field the theoretical approach from Wadas and Hug [82] is used. In particular, these authors have been shown that magnetic potential outside the magnetized tip can be described by the assumption of magnetic scalar potentials due to surface magnetic charges according to

$$\phi(\rho) = \int \frac{\mathbf{M}\mathbf{n}}{\rho}\,\mathrm{d}s, \tag{3.11}$$

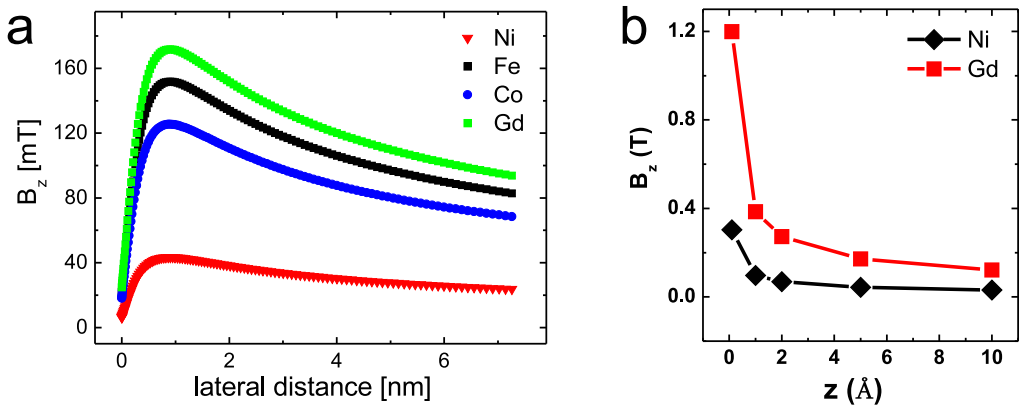

Figure 3.3.: (a) The z component of the lateral stray field on the sample at a distance z of 0.5 nm from the tip-apex as function of the lateral distance for typical ferromagnetic materials. (b) Magnitude of the magnetic stray field as function of z for Gd and Ni.

where ρ is the distance from the surface charge, **M** is the isotropic value of the tip magnetization, and **n** his unit vector. The value **Mn** therefore represents the surface charge density. The tip itself is modeled by an atomic pointed cone described in cylindrical coordinates by

$$\phi(\rho,\phi,z) = M\int_0^{2\pi} \mathrm{d}\theta \int_0^{R} \mathrm{d}R_s \frac{R_s}{\sqrt{(L\frac{R_s}{R}+z)^2 + r^2 + R_s^2 - 2R_s r\cos\theta}}, \tag{3.12}$$

where z is the tip-sample distance, L the height of the cone, R its radius, and r the lateral distance on the surface. By using for $L = 3\,\mathrm{nm}$, $R = 1.4\,\mathrm{nm}$, and $z = 0.5\,\mathrm{nm}$ the stray magnetic field was evaluated by $B = -\mathrm{grad}\,\phi$. The obtained results for the different types of ferromagnetic materials which were are summarized in Fig. 3.3. As a result we found that that these stray fields are highly localized, but their magnitude can easily reach several mT at typical tunneling distances [Fig. 3.3(a)]. These values are in good agreement with findings in Ref. [83]. Moreover, by lowering the tip-surface distance these values can be drastically enhanced [Fig. 3.3(b)]. In particular, for Gd tips the magnitude of the stray field at distances less then 0.01 nm is found to be 1.2 T close to the highest value possible at a Gd surface, $\vec{B}_{\max} = \mu_0 M\,/\,2 \approx 1.3$ T. Indeed, this high value is resulting from the relative high saturation magnetization of $M_{\mathrm{Gd}} = 1980\,\mathrm{G}$ of Gd compared to materials like Ni, which exhibits a relative low saturation magnetization of $M_{\mathrm{Ni}} = 510\,\mathrm{G}$. Therefore, as long as bulk tips are utilized the stray field can be reduced by using a material exhibiting a low saturation magnetization or by using antiferromagnetic bulk tips [77].

In order to overcome the stray field induced limitations thin film tips with a film thickness comparable to or lower than the tip-sample distance can be used as first described in Ref. [80]. In particular, to manufacture these tips an electrochemically etched polycrystalline W wire is heated up to 2200 K in the UHV chamber. After these treatments the tips are magnetically coated with a magnetic film with a thickness of several monolayers. This procedure has the additional advantage that in contrast to bulk tips the magnetization direction can be adjusted by choosing an appropriate film material, as well

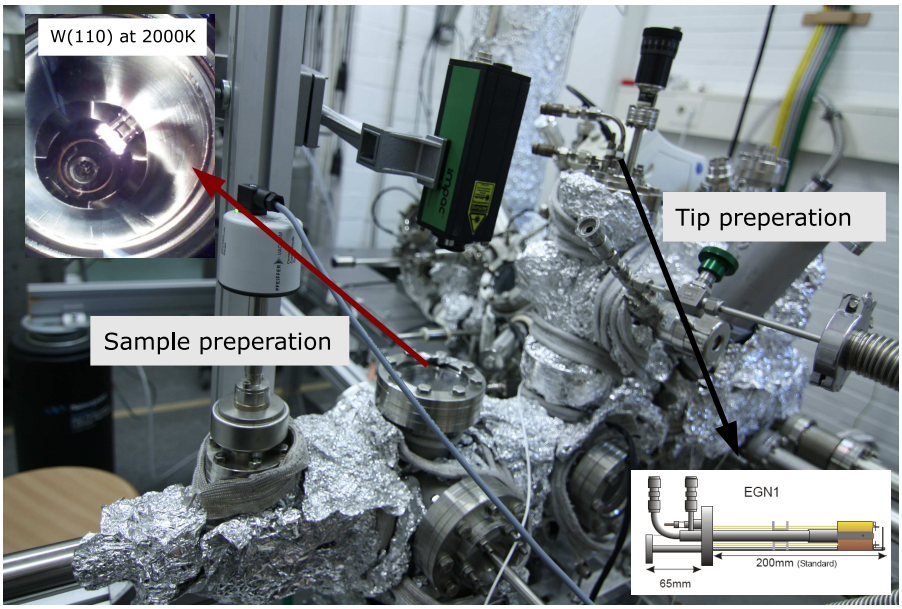

Figure 3.4.: Overview of the UHV chamber, which provides the needed tools for the preparation of spin-polarized experiments. Inset top: W(110) sample at 2300 K at the preparation station. Inset bottom: Blueprint of the electron beam evaporator adapted from [86].

as the film thickness. In detail, 3-10 ML Fe are sensitive to the in-plane component of the magnetization of the sample, where 25-80 ML Cr are usually sensitive to the out-of-plane component. However, Kubetzka et al. [83] showed that under critical conditions even small stray fields from ferromagnetic coated tips can substantially affect the magnetic structure of the sample. In order to avoid such effects these authors proposed to use antiferromagnetic Cr tips. Furthermore, as will be discussed in detail below Cr covered tips are found to allow to reverse magnetization direction by a controlled material deposition from the tip apex, and they are therefore a good choice for SP-STM investigations.

3.2.3. Experimental setup

Spin-polarized experiments were performed on a homemade low temperature STM operated at 7 K and in ultrahigh vacuum (UHV) with a base pressure of 10^{-9} Pa. This apparatus was designed by Jörg Kröger and is divided into two main parts consisting of a chamber for experimental preparation and an analysis chamber, where the microscope is located. For further details the reader is referred to [84, 85].

During this thesis a third chamber was developed, which provides tools for the preparation of spin-polarized experiments. In order to give a brief overview a photograph of this chamber is depicted in Fig. 3.4. In detail, the chamber can be separated from the preparation chamber with a gate valve (*VAT*, Switzerland), where the UHV inside the chamber is generated by a turbomolecular pump (*Pfeiffer Vacuum*, Asslar). Additionally, a titanium sublimation pump (*VACOM*, Jena) and a cold trap (*Pink*, Wertheim) are

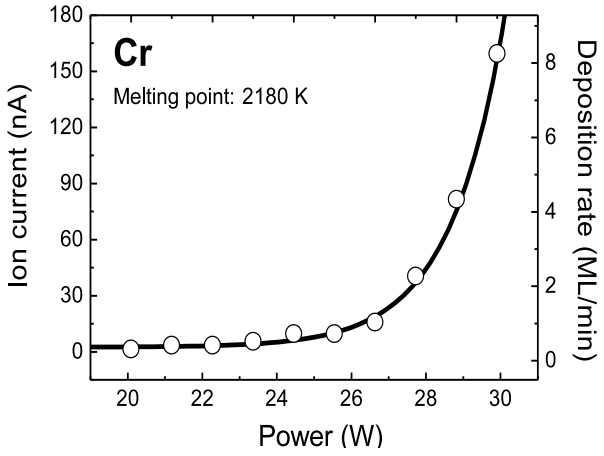

Figure 3.5.: Relationship between the experimental settings of the Cr e-beam evaporator and the obtained deposition rate: The rates were judged from the deposition time and corresponding STM images (circles). To guide the eyes an exponential function is fitted to the experimental data (black curve).

mounted, which allows the whole setup to reach easily a low pressure of less than 10^{-8} Pa. Furthermore an iongetter pump (*Meca 2000*, France) is installed, which enables to keep the UHV in the chamber when the turbomolecular pump is shut down, as it is the case during measurements. For the transfer of sample and tips from the chamber to the microscope a magnetic motion drive (*Huntington*,USA) as well as a wobble stick (*Ferrovac*, Switzerland) is mounted.

In order to obtain tips, which exhibit an intrinsic spin polarization at the Fermi level electrochemically etched polycrystalline W wires with a diameter of 0.25 mm are used. They are cleaned by a high temperature flash and coated with magnetic material. An *Oxford Applied Research* electron beam evaporator is employed to deposit magnetic films onto the tip to this end. The tip preparation station is indicated in Fig. 3.4. As tip material antiferromagnetic Cr was used in the experiment, as discussed in detail in the previous section. The relationship between the experimental settings of the evaporator and the obtained deposition rate are presented in Fig. 3.5, where this rate was judged from the deposition time, as well as from corresponding STM images.

As it will be discussed in the following, the preparation of substrate surfaces used in this thesis to fabricate samples with a high magnetic signal requires a preparation temperature of more than 2300 K. To this end a homemade preparation station was developed which allows to reach such high temperatures. In detail, the preparation station has two electrical contacted pins to take a sample, as well as a removable filament. In order to obtain the needed temperature stability which allows preparation temperatures of more than 2300 K the prefabricated parts were manufactured from molybdenum. The sample annealing is carried out by using electron bombardment, where a high voltage of 2000 V is applied to the sample. The obtained temperatures can be recorded with the help of an external pyrometer (Impac Electronic, Frankfurt). Finally, a gas line and a leak valve (*Pfeiffer Vacuum*, Asslar) are mounted to the chamber, which allow to insert gas into the UHV chamber.

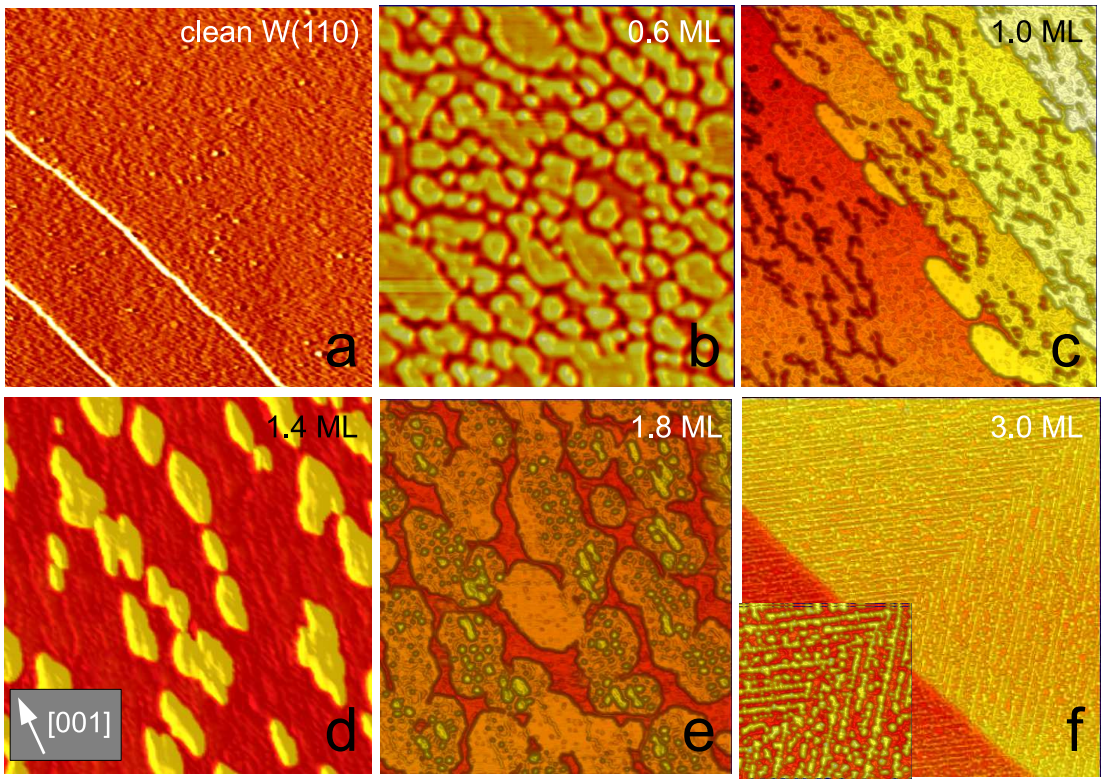

Figure 3.6.: (a) STM image of clean W(110). (b-f) Fe films on W(110) grown at 300K: (b) 0.6 ML, $40 \times 40\,\mathrm{nm}^2$, $I = 0.1\,\mathrm{nA}$, and $V = 300\,\mathrm{mV}$. (c) 1.0 ML, $110 \times 110\,\mathrm{nm}^2$, $I = 0.1\,\mathrm{nA}$, and $V = 200\,\mathrm{mV}$ (d) 1.4 ML, $100 \times 100\,\mathrm{nm}^2$, $I = 1\,\mathrm{nA}$, and $V = 700\,\mathrm{mV}$. (e) 1.8 ML, $100 \times 100\,\mathrm{nm}^2$, $I = 0.1\,\mathrm{nA}$, and $V = 750\,\mathrm{mV}$. (f) 3.0 ML, $200 \times 200\,\mathrm{nm}^2$, $I = 0.1\,\mathrm{nA}$, and $V = 400\,\mathrm{mV}$. Inset (f): close-up view ($50 \times 50\,\mathrm{nm}^2$).

3.3. Previous results: Fe on W(110)

The magnetic properties of the substrate system Fe/W(110) were intensely studied for the last decade of years [88–93], since it turned out that $1 - 2\,\mathrm{ML}$ Fe epitaxially grown on W(110) is an extremely interesting system in order to study 2D ferromagnetism at an atomic scale. Moreover this system exhibits a clear spin-polarized electronic structure with different magnetization states, and is therefore a powerful test system to characterise the magnetic state of SP-STM tips. In this section a short overview of the topographic, electronic, and magnetic structure of Fe on the W(110) surface will be given, focusing mainly on those aspects which are important for this thesis.

3.3.1. The W(110) surface

Tungsten has the highest melting point (3700K) of all the non-alloyed metals and the second highest of all the elements after carbon. The crystal structure of tungsten is body-center-cubic (bcc) with a lattice parameter of 3.165 Å. Since tungsten is very unlikely to alloy with d-transition metals, it is an ideal substrate to stabilize thin magnetic films.

In order to clean the W(110) surface from its main impurity carbon a cleaning procedure has been realized consisting of oxygen annealing (duration $d = 30\,\mathrm{min}$, $T = 1500\mathrm{K}$)

and subsequent high temperature flashs ($T = 2300$K). By gradually reducing the oxygen pressure between subsequent annealing cycles down to 2×10^{-8} mbar in the final cycle a density of impurity atoms of only 2×10^{-3} can be obtained [87]. In order to demonstrate the outcome of this cleaning procedure a constant-current STM image of the W(110) surface recorded after several dozens of such cleaning cycles is shown Fig. 3.6(a). In particular, the roughness of the clean W(110) surface is relatively strong compared to noble metal surfaces, *i. e.* Au, Cu, and Ag.

3.3.2. Ultrathin Fe film growth on W(110)

The growth of thin Fe films on W(110) is presented in Fig. 3.6(b)-(f). Therein, constant-current STM images of ultrathin Fe films on W(110) in the coverage range of $0.6 - 3.0$ monoatomic layer (ML) are depicted. These Fe films are grown on clean W(110) at room temperature using a growth rate of 0.1 ML/min. In order to avoid temperature induced modification of the growth process the W(110) surface is held into UHV after the last preparation cycle for 60 min before Fe is deposited.

The growth of the first monoatomic Fe layer is dominated by the large lattice mismatch of 9.4 % between Fe (lattice constant $a_{\mathrm{Fe}} = 2.867$ Å) and W (lattice constant $a_{\mathrm{W}} = 3.165$ Å), which leads to a pseudo-morphologically growth of Fe nanoislands [88], as shown in Fig. 3.6(b). At a coverage regime of ≈ 1 ML a second layer starts to nucleate on an almost closed first monolayer [see Fig. 3.6(c)].

The second layer nucleates in islands which are surrounded by the monolayer sea, as shown in Fig. 3.6(d). These islands show a preferred growth direction along [001] leading to a length of approximately 30 nm and width of 10 nm on average. At a coverage of about 1.8 pseudomorphic ML, a network of dislocation lines appears indicating a local onset of relaxation by an introduction of additional rows of atoms [88]. The third layer starts to nucleate on top of these dislocation lines before the second layer is closed, as shown in Fig. 3.6(e).

These dislocation lines can be used to guide the deposition of the third Fe layer. As presented in Fig. 3.6(f), we found stripes of third layer islands along the dislocation pattern of the second ML.

The morphology of Fe on tungsten can be modified by various parameters such as the growth temperature and the surface orientation. In fact, using a vicinal W(110) surface and elevated growth temperatures of $T = 550$K, stripes or nanowires along the substrate step edges can be obtained [89].

3.3.3. Magnetism of Fe islands studied by SP-STM

As already above-mentioned thin Fe layers on W(110) exhibit an extremely interesting playground to demonstrate the capability of SP-STM, as it will be done next.

As early investigated by Kerr effect measurements [90, 91] DL Fe islands surrounded by a close Fe ML exhibit a perpendicular anisotropy. While the Fe ML preferentially keeps a magnetization within the Fe film plane [91], at the DL islands a out-of-plane magnetization can be observed [90, 92]. The different orientations of the island magnetization are readily probed by the Cr-covered tip with sensitivity for out-of-plane magnetizations. In Fig. 3.7(a) Fe islands with magnetization direction parallel (antiparallel) to the tip magnetization appear with higher (lower) contrast. To maximize the contrast difference, $\mathrm{d}I/\mathrm{d}V$

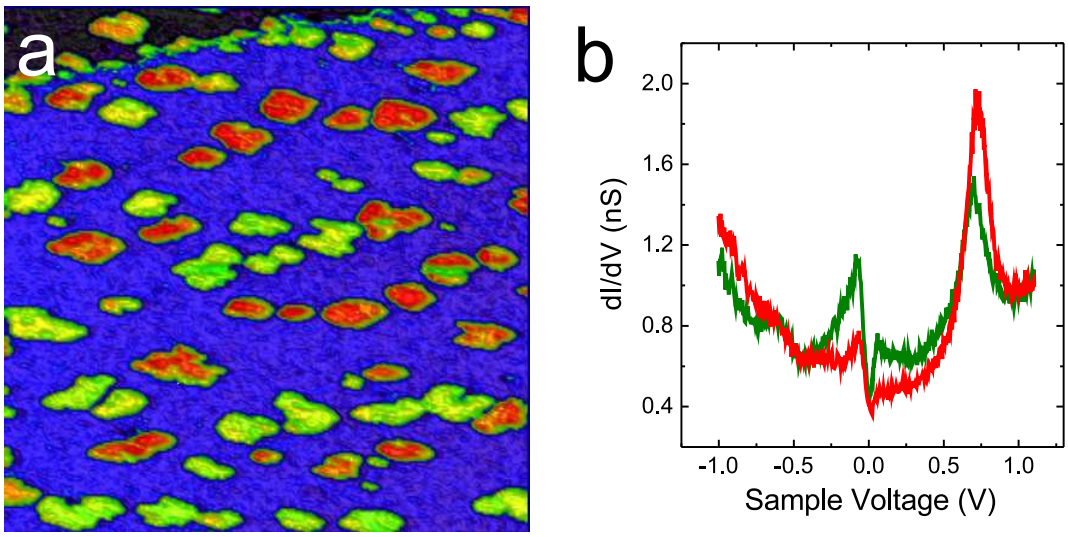

Figure 3.7.: (a) Map of dI/dV and (b) spectra of dI/dV measured with a Cr covered tip on Fe double-layer islands surrounded by a closed ML Fe/W(110) preperared at 300K by evaporation of 1.5 ML Fe on clean W(110).

maps were recorded at a voltage which corresponds to the energy of a spin-polarized minority d_{z^2} state of the islands [93].

The spectroscopic signature of this state is presented in 3.7(b), which shows dI/dV spectra recorded on opposite magnetized DL Fe islands. At ≈ 0.7 V both islands exhibit a strong spectral feature. It was shown in Ref. [92] that the difference between the opposite magnetized DL Fe islands arise from spin-polarized tunneling. Calculated local density of states for a Fe film with a thickness of two atomic layers on W(110) revealed that peaks at ≈ -0.08 and ≈ 0.7 V represent d_{z^2} minority states, while the enhancement of local density of states around 0.05 V was assigned d_{xy+xz} or d_{z^2} orbital character [93]. The origin of the signature in the dI/dV signal around zero voltage, however, is not clear at present. In particular, calculations in Ref. [93] do not reproduce this spectroscopic feature. At negative bias voltages the spin polarization of the Cr tip is reversed and the spectra are dominated by the density of states of the tip [92]. In order to avoid such tip induced modifications of the spin-polarized tunneling signal we focus on the bias range of the d_{z^2} minority state at ≈ 0.7 V in the following.

In order to demonstrate the high spatial magnetic resolution of SP-STM, tunneling spectroscopy is used in the following to obtain images of magnetic domain walls. Following Ref. [77] such an analysis can be done on constricted islands. In Fig. 3.8(a) such an island is presented. This island may originate from the nearby nucleation of two individual DL islands in the early stage of the growth process. As it can be recognized directly, compared to the left part of the Fe island a higher dI/dV signal is found in the right part. Between these two parts, where the assembly becomes the narrowest, a *Bloch* domain wall is located [see Fig. 3.8(b)], which allows the domain wall energy to be minimized (for more details see [77] and references therein). In order to analyze this experimental finding in some more detail, a cross-sectional profile along the indicated line in Fig. 3.8(a) is taken and presented in Fig. 3.8(c). Moreover, this profile has been fitted by a domain wall profile as

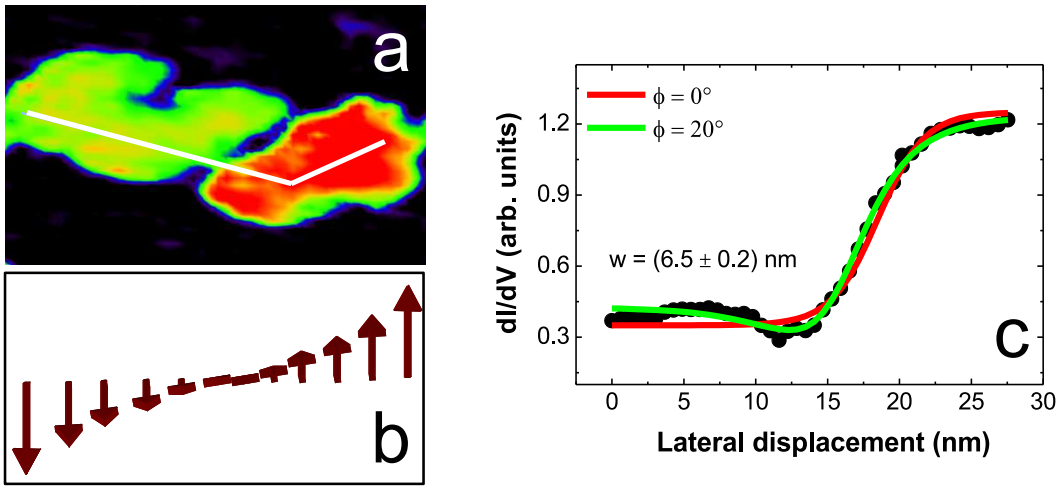

Figure 3.8.: (a) $\mathrm{d}I/\mathrm{d}V$ map measured with a Cr covered tip on a restricted double-layer Fe islands. A domain wall is located at the narrowest part of the island. (b) Sketch of the domain wall (a *Bloch* domain wall is assumed according to Ref. [77]). (c) Cross-sectional profile along the line marked in (a). The colored solide lines are fits to the experimental data according to Eq. (3.13) (red line) and according to Eq. (3.14) (green line), which take an angle between the magnetization direction of the tip apex and the easy axis of the sample into account. Both fits result in a domain wall width of $6.5 \pm 0.2\,\mathrm{nm}$.

described by micromagnetic theory [94]:

$$\frac{\mathrm{d}I}{\mathrm{d}V}(x) = y_0 + y_{\mathrm{sp}} \tanh\left(\frac{x - x_0}{\omega/2}\right), \tag{3.13}$$

where x_0 is the position of the domain wall, ω is the domain wall width, and y_0 and y_{sp} are the spin-average and spin-polarized $\mathrm{d}I/\mathrm{d}V$ signal, respectively. As a result a domain wall width of $\omega = (6.5 \pm 0.2)\,\mathrm{nm}$ is found (red line in Fig. 3.8(b)) in agreement with findings in Ref. [77].

Following Ref. [77, 92] the domain wall value ω can be estimated using the equation $\omega = 2\sqrt{A/k}$, where k is effective anisotropy of the Fe DL ($k_{\mathrm{DL}} = 1 \times 10^6\,\mathrm{Jm}^{-3}$) and A the exchange stiffness ($A = 1 \times 10^{-11}\,\mathrm{Jm}^{-1}$). As a result a value of $\omega = 6\,\mathrm{nm}$ is obtained, which is in good agreement with previous SP-STS investigations [77].

Furthermore, a possible angle ϕ between the magnetization direction of the tip apex and the easy axis of the sample can be taken into account by the extended domain wall profile [77]

$$\frac{\mathrm{d}I}{\mathrm{d}V}(x) = y_0 + y_{\mathrm{sp}} \cos\left\{\arccos\left[\tanh\left(\frac{x - x_0}{\omega/2}\right)\right] + \phi\right\}. \tag{3.14}$$

Applying this formular as a fit function to the extracted coss-sectional profile shown in Fig. 3.8(b) an angle of $\phi = 20°$ is found to be reproduced as the best the experimental profile (green solide line in Fig. 3.8(c)). However, the y-scale of the profile plot indicates that at the position of the domain wall the $\mathrm{d}I/\mathrm{d}V$ signal changes by a factor of three, which corresponds to an effective spin-polarization of the junction of more than 50%. Compared to previous investigations on this system [92] such a high spin-polarization of the junction indicates a nearly perfect parallel (antiparallel) alignment between the

magnetization direction of, respectively, tip and sample. The observed value for ϕ can more likely be explained with the fact that small Fe islands with a diameter between 2 and 3 nm are reoriented to an in-plane magnetization due to exchange coupling to the first Fe layer, because the width at the domain wall position on the Fe island is only ≈ 2.5 nm. In particular, Kubetzka et al. [92] have described this behaviour by a reorientation transition to an in-plane magnetization, driven by exchange coupling to the in-plane magnetized ML.

In summary, Fe island grown on a first Fe layer on W(110) exhibit a out-of-plane magnetization. While small islands with a diameter between 2 and 3 nm are reoriented to an in-plane magnetization due to exchange coupling to the first Fe layer, Fe islands with a minimum width of 5 nm exhibit a stable out-of-plane magnetization. For the following SP experiments, double-layer Fe islands on W(110) are used as a magnetic substrate.

3.4. Tuning the spin contrast in SP-STM

In the following, we show that by controlled tip-surface contacts and concomitant material transfer from the tip to the surface, the magnetization of a Cr-covered W tip may be tuned and even reversed. Further, spin contrast results from spin-polarized states of the magnetic nanostructure investigated. This preparation procedure enables addressing magnetic properties without applying external magnetic fields.

In order to characterize the magnetization of the probe, W(110) covered with ≈ 1.4 ML of Fe is used as a substrate system, which was discussed in detail above. An estimate for the spin polarization of the tunnel junction [80] may be provided by the voltage dependent asymmetry

$$A(V) = \frac{[\mathrm{d}I/\mathrm{d}V(V)]_p - [\mathrm{d}I/\mathrm{d}V(V)]_a}{[\mathrm{d}I/\mathrm{d}V(V)]_p + [\mathrm{d}I/\mathrm{d}V(V)]_a}, \tag{3.15}$$

where p (a) referred to Fe islands with a magnetization direction parallel (antiparallel) to the tip magnetization appears with higher (lower) contrast. Indeed, this method include a certain ambiguity. For example, when extracting the sample polarization from the SP-STS data one encounters the problem that for a given bias voltage the tip-sample distance (and so the tunneling probability) is different for the p and a Fe islands, similar to our discussion in Sections 2.4 and 2.5 of $\mathrm{d}I/\mathrm{d}V$ maps recorded at constant current for non-magnetic tips. However, since we were interested in a general trend of the spin polarization with varying tip status, we did not consider more sophisticated definitions of the asymmetry. In particular, normalization of dI/dV by the transmission coefficient of the tunnel barrier [95, 96] was neglected since apparent height differences of opposite magnetized islands were rather low. In constant current STM images recorded at 1.1 V, i. e., at the voltage at which the feedback loop was opened prior to spectroscopy [Fig. 3.7(b)], the difference in the apparent height between opposite magnetized islands is less than 10 pm.

The tip was then modified by tip-surface contacts as previously reported for non-magnetic tips. [66, 264] While for voltages around 100 mV in most of the contacts single atoms were transferred from the tip to the surface, the probability of cluster transfer increased for voltages exceeding 500 mV. Figure 3.9 shows that upon transfer of a single Cr atom a possible change of the spin contrast is below the detection limit. Prior to atom transfer [Fig. 3.9(a)] the asymmetry was ≈ 0.18, as evaluated from the spin-resolved $\mathrm{d}I/\mathrm{d}V$ map depicted in the inset of Fig.3.9(a). After atom transfer [see arrows in Fig.3.9] the asymmetry of the tunnel junction has not changed.

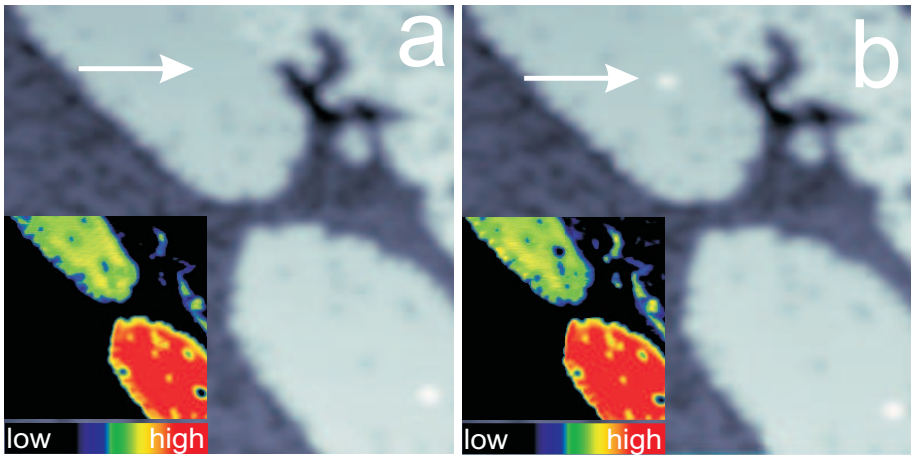

Figure 3.9.: STM images of two Fe islands on W(110) (0.7 V, 1 nA, 20 nm × 20 nm). Between these two images a single Cr atom is transferred from the tip apex by controlled tip-surface contacts at 100 mV. Insets: Simultaneously recorded maps of $\mathrm{d}I/\mathrm{d}V$, which show no change in the spin contrast.

As observed in a few tens of measurements the transfer of Cr clusters, however, did modified the asymmetry. Using the apparent dimensions of the clusters in STM images, the average number of Cr atoms inside the clusters was estimated to $70 - 100$. The top panel of Fig. 3.10 shows a sequence of spin-resolved maps of $\mathrm{d}I/\mathrm{d}V$ of the same Fe islands, which were recorded with different asymmetries of the tunnel junction. In particular, the asymmetries were calculated from $\mathrm{d}I/\mathrm{d}V$ maps, which include equal areas on different magnetized islands. Such areas are analyzed by counting the pixels ($\mathrm{d}I/\mathrm{d}V$ signals) and display this count in the form of histograms [bottom panel of Fig. 3.10]. As a result three peaks appear in the histograms. The first peak corresponds to the area on the first ML, while the other peaks of these histograms are correspond to the areas on different magnetized DL islands. The asymmetries were estimated then by using Eq. 3.15, where the $\mathrm{d}I/\mathrm{d}V$ values are obtained by fitting a superposition of three Gaussian lines to the $\mathrm{d}I/\mathrm{d}V$ values in histogram. Starting with a Cr-covered tip, which provided an asymmetry of ≈ 0.23 at ≈ 0.7 V [Fig. 3.10(a)] this tip was prepared according to the above-mentioned procedure. As a result, the asymmetry was reduced to ≈ 0.09 at the same voltage [Fig. 3.10(b)]. After another preparation step, the asymmetry was decreased to ≈ -0.21 [Fig. 3.10(c)], i. e., the magnetization of the tip was almost reversed compared to the tip magnetization presented in Fig. 3.10(a). Most likely, in the course of tip preparation the magnetization direction of the tip apex was modified, i. e., the angle enclosed by the tip and island magnetizations changes from 0° [Fig. 3.10(a)], via almost 90° [Fig. 3.10(b)] to nearly 180° [Fig. 3.10(c)]. A possible change of the exchange-split band structure of the Cr film, which likewise could alter the asymmetry via the tip polarization is rather unlikely. Further, a modification of the electronic or magnetic structure of the Fe islands can be ruled out since the tip was prepared several hundreds of nanometers apart from the Fe islands shown in Fig. 3.10 and since the magnetic stray field of the antiferromagnetic tip vanishes. [83]

Two previous works reported the manipulation of the tip magnetization. In Ref. [97] a voltage pulse was applied to a clean W tip atop thin Mn layers on Fe(001), which according to Yamada et al. [97] most likely led to a *tip crash* or local melting of the

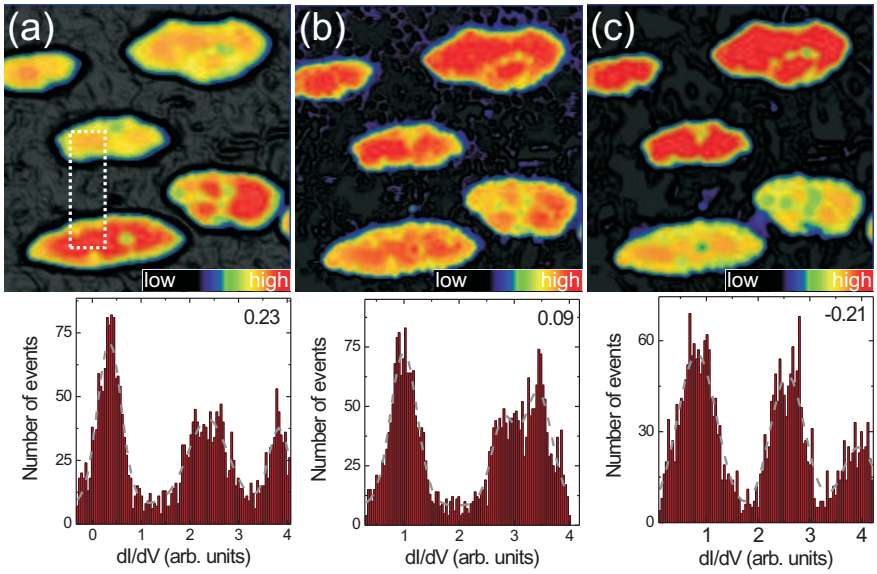

Figure 3.10.: Spin-resolved maps of dI/dV of the same Fe islands on W(110) recorded with different Cr-covered tips at the voltage of 0.7 V. While in (c) a contrast reversal compared to (a) occurred, i. e., the tip magnetization was reversed, in (b) the spin-polarized contrast contrast was nearly vanished. At this voltage the asymmetries [Eq. (3.15)] are determined from histograms, which count the observed frequency of $\mathrm{d}I/\mathrm{d}V$ values of equal areas on different magnetized islands [see frame in Fig. 3.10(a)]. Dashed gray lines are fits to determine the values of $\mathrm{d}I/\mathrm{d}V$.

tip-sample contact area. Such tips showed magnetic contrast owing to Mn, which covered the tip apex during the preparation procedure. In another experiment [98] clean W tips were most likely covered by Dy clusters upon indenting the tip several nanometers into a Dy film epitaxially grown on W(110). Strong magnetic contrast was then achieved by highly spin-polarized unoccupied states of the Dy cluster. The authors [98] remark that the Dy-covered tip properties seemed to be less controllable than those of Cr-coated tips.

Chapter 4.

Spin Valve Effect in Single-Atom Contacts

The spin valve effect is at the heart of the giant magnetoresistance, which was discovered in layered magnetic materials [1, 2]. It describes the electron mobility, which depends on the relative orientation between the spin of the electron and the magnetization of the layer the electron passes through.

Current research is aiming at reducing the size of spin valves. Indeed, an emerging field is the investigation of molecules and atoms acting as spin valves. For instance, strong variations of the conductance have been reported for spin transport through carbon nanotubes between ferromagnetic electrodes [99, 100]. Magnetoresistive effects were also reported in Ni and Co quantum point contacts [101, 107, 111]. However, transport properties of magnetic single-atom contacts are far from being understood and inconsistent experimental results have been reported [3, 4]. Some of the inconsistencies may be related to contaminants at the junction [102] or to the lack of characterization of the atomic details of the junction.

In this chapter, we show that single magnetic atoms, which are adsorbed on ferromagnetic nanostructures and in contact with the spin-polarized probe of the scanning tunneling microscope may act as spin valves controlling the spin-polarized current, which is ballistically transferred through the atoms. To this end the electronic and magnetic structure of Fe islands adsorbed on W(110) and of individual Co and Cr atoms adsorbed on the Fe islands were characterized by spin-resolved scanning tunneling microscopy (STM) and spectroscopy, as described in Sec. 4.2. Ferromagnetic and antiferromagnetic coupling of, respectively, Co and Cr atoms to the Fe islands was found. As a consequence, the relative orientation between the magnetization of the Cr-coated W tip and of the adsorbed magnetic atom is known. Sec. 4.3 is dealing with contact measurements. Junction conductances of $\approx 0.5\,G_0$ ($G_0 = 2e^2/h$: quantum of conductance with $-e$ the electron charge and h Planck's constant) were observed for antiparallel alignment of the magnetizations, while conductances of $\approx 0.7\,G_0$ were measured for parallel alignment. In a simple model, these contact conductances may be understood by considering ballistic electron transport through spin-polarized *sp* and *d* channels. Before investigating the properties of single magnetic atoms a brief introduction to the basic aspects of giant magnetoresistance is given in Sec. 4.1

4.1. From giant to ballistic magnetoresistance

In this section a brief introduction to the magnetoresistance effects will be given. For a more detailed review the reader is referred to [4, 103].

Electron scattering at magnetic interface in a magnetic layered structure depends on whether electron spin is parallel or antiparallel to the magnetic moment of the layer. This effect is called *giant magnetoresistance effect* (GMR) and was discovered in 1987 by *P.*

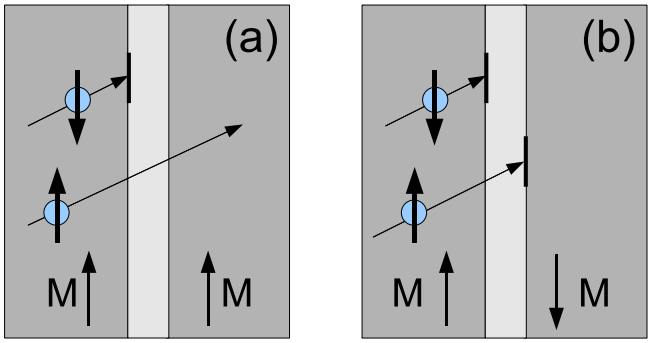

Figure 4.1.: Schematics of the GMR effect: (a) Two ferromagnetic layers are separated by a very thin non-ferromagnetic layer, which are parallel magnetized. The probability of electrons which spin parallel to the magnetization direction of the layers to be scattered is small and the electrons can pass the interfaces in the magnetic layered structure unhampered. (b) The magnetization direction in one of the magnetic layers is reversed. More electrons are scattered and the measured resistance of the layered structure increases.

Grünberg and *A. Fert* [1, 2] and is schematically drawn in Fig. 4.1. Therein two ferromagnetic layers are separated by a very thin non-ferromagnetic layer, which are parallel magnetized in Fig. 4.1(a) and antiparallel magnetized in Fig. 4.1(b). In particular, the probability of scattering depends strongly on the relative direction of the spin of an electron and the orientation of the magnetisation inside the layer. If the spins of the electrons are parallel to the magnetization direction in the two layers, the probability to be scattered is small and the electrons are nearly free in their random walk. As a result, these electrons can pass the interfaces in the magnetic layered structure unhampered, as shown in Fig. 4.1(a). This situation is changed if the magnetization direction in one of the magnetic layers is reversed. In fact, more electrons are scattered and they are prevented from their random walk. Hence, the measured resistance of the layered structure increases, as schematically drawn in Fig. 4.1(b).

Among the GMR the most known magnetoresistance effects are the tunnel magnetoresistance (TMR), which was already discussed in detail in Sec. 3.1, and the anisotropic magnetoresistance. The AMR effect in ferromagnetic materials describes the dependence of the resistivity on the angle between the current and the magnetization, when an external magnetic field is applied. However, the relative change in the magnitude of the resistance due to the GMR compared to the anisotropic magnetoresistance is huge, which has led to the term giant. Generally, magnetoresistance is the property of a material to change the value of its electrical resistance when an external magnetic field is applied to it. The magnetoresistance ratio is defined to be the ratio of the resistivity change to the resistivity in the magnetically parallel configuration,

$$R_{\mathrm{MR}} = \frac{R_{\uparrow\downarrow} - R_{\uparrow\uparrow}}{R_{\uparrow\uparrow}}, \tag{4.1}$$

where $R_{\uparrow\downarrow}$ and $R_{\uparrow\uparrow}$ respectively are the resistance of parallel and antiparallel magnetization of two separated magnetic layers.

The GMR occurs when an antiferromagnetic (AF) alignment is changed by an applied external magnetic field into a ferromagnetic (F) alignment. In order to fabricate such magnetic devices F/AF/F layered structures can be used, as well as with F/non-magnet/F

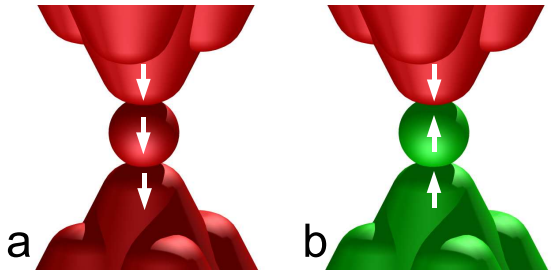

Figure 4.2.: Schematics of the BMR effect: Electrons are transferred in channels through the junction without scattering. (a) Magnetization across point contact parallel in direction gives rise to a low magnetoresistance. (b) Magnetization across point contact opposite in direction gives rise to a high magnetoresistance.

layers it is possible to obtain a GMR. In particular, by depositing one ferromagnetic film directly on a substrate and the second on top of the non-magnetic interlayer one film is more strained than the other, which leads to a higher coercivity. If an external magnetic field is applied to the whole structure one magnetic film reverses later than the other, which leads to an antiparallel alignment in a small range of the applied magnetic field. This device is sometimes also called a *spin valve*. The spin-valve GMR can also be generated by pinning the magnetization of one layer by using an antiferromagnic material in direct contact, known as *exchanging bias*. The free ferromagnetic layer in this structure can be switched by a small applied external magnetic field, while the magnetization of the pinned ferromagnetic layer is fixed due to the interface induced exchange-biased effect.

In the last decade of years both methods to obtain an antiferromagnetic alignment have been applied to use the GMR effect in information and communication devices. In fact, today's dimensions of bit sizes in hard disk and memory devices are a result of the discovery of the giant magnetoresistance. However, the change of the resistance is achieved by modifying the magnetization within a distance of the order of 100 nm, over which conduction electrons keep memory of their spin orientation. Therefore, magnetoresistive effects in such materials may be understood within a *diffusive* conduction model, which considers spin-dependent scattering in the bulk and at the interface [104–106], as discussed above. The ongoing miniaturization of electronic devices fueled the investigation of the conductance of magnetic junctions at the atomic scale, which are characterized by *ballistic* electron transport, *i. e.*, electrons are transferred through the junction without scattering. Several publications reported ballistic magnetoresistive effects [107–111], which are based on different reflection probabilities for spin-up and spin-down electrons impinging on a magnetic domain wall, which is localized at the point contact. In Fig. 4.2 a schematic drawing of the BMR is presented. While magnetization across point contact parallel in direction gives rise to a low magnetoresistance [Fig. 4.2(a)], magnetization across point contact opposite in direction gives rise to a high magnetoresistance [Fig. 4.2(b)]. However, an understanding of extraordinarily high changes of the magnetoresistance [109,110] is still a controversial subject [4, 112, 113]. For instance, magnetorestriction may mimic ballistic magnetoresistance in experiments with external magnetic fields.

Another effect of nanometer-scaled junctions is the ballistic anisotropic magnetoresistance, which has been predicted for ideal infinitely long wires of Ni and Fe [114]: a rotation of the magnetization leads to abrupt changes in the wire conductance due to additional

band crossings at the Fermi level. The interpretation of experimental observations along these lines [115–117] is vividly debated [118–120]. Abrupt changes of the point contact conductances observed in the experiments may be due to sudden changes in atomic configurations [118], to giant orbital moments in the contacts [119] or to spin-orbit coupling together with the reduced symmetry of the contact geometry [120].

In the following the conductance of single-atom contacts comprised of Co and Cr atoms, a Fe-covered W(110) substrate, and Cr-covered tips is investigated using spin-resolved spectroscopy.

4.2. Spin polarization of single atoms

Before investigating transport properties of single magnetic atoms, an unambiguous characterization of magnetic and electronic properties of the contacting electrodes had to be provided. To this end, clean W tips were coated with a Cr film, whose thickness was chosen such as to exhibit a sensitivity for out-of-plane magnetization [83], as described in detail in Sec. 3.3. The in Sec. 3.3 presented Fe islands on W(110) surrounded by a closed atomic layer of Fe were used as magnetic substrate [92]. These islands are single-domain particles, and exhibit an out-of-plane magnetization parallel and antiparallel to the surface normal. Measurements were performed on Fe islands with a minimum diameter of 5 nm, since for island widths between 2 and 3 nm a reorientation to an in-plane magnetization due to exchange coupling to the first Fe layer occurs [83]. Iron islands with different magnetization orientations appear with a maximum contrast difference in maps of $\mathrm{d}I/\mathrm{d}V$ acquired at $\approx 0.7\,\mathrm{V}$ [Fig. 4.3(a)]. This voltage corresponds to the energy of a spin-polarized island state (see below), which is less pronounced if the magnetization directions of tip and island are antiparallel. Consequently, islands appear bright for parallel alignment and dark for antiparallel alignment of the magnetizations. In the following these islands are referred to as p and a islands, respectively. On these islands single Co and Cr atoms were adsorbed. Since Cr atoms were transferred from the tip, they were readily discriminated from Co atoms. Moreover, in constant-current STM images recorded at 0.7 V [Fig. 4.3(b)] Cr atoms appear higher than Co atoms, *i. e.*, the chemical identity of the imaged atom was determined.

Figure 5.6 shows spin-resolved spectra of $\mathrm{d}I/\mathrm{d}V$ of p and a islands [Fig. 4.4(a)] together with spectra acquired on Co [Fig. 4.4(b)] and on Cr [Fig. 4.4(c)] adsorbed on these islands. At $\approx 0.7\,\mathrm{V}$ both islands exhibit a strong spectral feature, which is more pronounced for p than for a islands. It was shown in Ref. [92] that this difference between p and a islands arises from a magnetic effect, caused by spin-polarized tunneling. Calculated local density of states for a Fe film with a thickness of two atomic layers on W(110) revealed that peaks at ≈ -0.08 and $\approx 0.7\,\mathrm{V}$ represent d_{z^2} minority states, while the enhancement of local density of states around 0.05 V was assigned d_{xy+xz} or d_{z^2} orbital character [93]. The origin of the strong depletion of the $\mathrm{d}I/\mathrm{d}V$ signal around zero voltage, however, is not clear at present. In particular, calculations in Ref. [93] do not reproduce this spectroscopic feature.

Spectra of $\mathrm{d}I/\mathrm{d}V$ acquired atop single adsorbed atoms (adatoms) strongly modify the pure Fe island spectra. The most striking changes are observed for the unoccupied d_{z^2} peak, which shifts from $\approx 730\,\mathrm{mV}$ [Fe island, Fig. 4.4(a)] to $\approx 690\,\mathrm{mV}$ [Co adatom, Fig. 4.4(b)] and to $\approx 630\,\mathrm{mV}$ [Cr adatom, Fig. 4.4(c)] and simultaneously broadens. While both adatom spectra exhibit spin-dependent electronic structure, the Co adatom spectrum

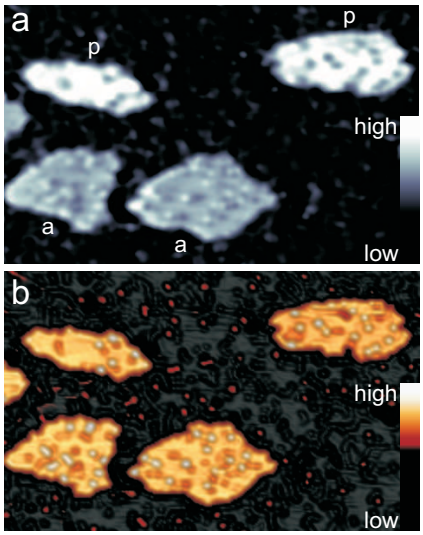

Figure 4.3.: (a) Spin-resolved constant-current map of $\mathrm{d}I/\mathrm{d}V$ of Fe islands on Fe-covered W(110). Bright and dim island reflect parallel (p) and antiparallel (a) alignment of tip and island magnetization. Additional structure on the islands is due to adsorbed Co and Cr atoms. (b) Constant-current STM image of the Fe islands shown in (a). Bright dots on the islands and on the first Fe layer are images of Co and Cr adatoms (0.7 V, 1 nA, 45 nm × 30 nm).

appears to follow the same spin polarization as given by the Fe island, while for Cr this polarization seems to be inverted.

To see this more clearly, normalized differences of the $\mathrm{d}I/\mathrm{d}V$ spectra are compared in Fig. 4.5. As already demonstrated in Sec. 3.4 spectroscopic differences are best seen by the voltage dependent asymmetry

$$A(V) = \frac{[\mathrm{d}I/\mathrm{d}V(V)]_{i,p} - [\mathrm{d}I/\mathrm{d}V(V)]_{i,a}}{[\mathrm{d}I/\mathrm{d}V(V)]_{i,p} + [\mathrm{d}I/\mathrm{d}V(V)]_{i,a}} \tag{4.2}$$

(i = Fe, Co, Cr). Figure 4.5 shows the voltage dependent asymmetry for Fe islands (dashed line), Co (gray) and Cr (light gray) adatoms. Between ≈ 0 and ≈ 150 mV the normalized difference is negative for the Fe islands and the Co adatoms, while it is positive in the in roughly the same voltage interval for the Cr adatoms. From ≈ 620 to ≈ 900 mV Fe islands and Co adatoms share the same positive sign of the normalized difference, while the normalized difference of the Cr adatoms is negative up to ≈ 1000 mV. Consequently, Fe islands and Co adatoms exhibit the same trend of the sign of the voltage dependent asymmetry, while the opposite trend is observed for Fe islands and Cr adatoms. We may be interpret this observation as the ferromagnetic (antiferromagnetic) coupling between Fe islands and Co (Cr) adatoms. A similar interpretation based on normalized $\mathrm{d}I/\mathrm{d}V$ differences has been reported for the ferromagnetic (antiferromagnetic) coupling between Fe (Cr) adatoms on Co islands on Cu(111) [123]. Our observations are also in agreement with an investigation of electronic and magnetic properties of single Ni, Co, Cu, Fe, Cr atoms adsorbed on Co islands on Cu(111), which were demonstrated to locally modify the spin polarization of the Co islands [125].

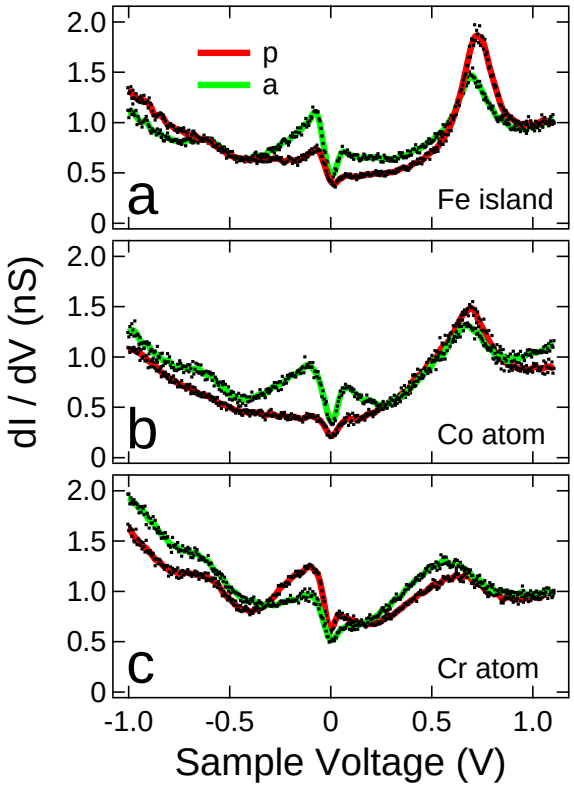

Figure 4.4.: Spin-resolved $\mathrm{d}I/\mathrm{d}V$ spectra recorded (a) on double-layer Fe islands on W(110), (b) on Co and (c) on Cr atoms adsorbed on Fe islands. Spin contrast is obtained by parallel (p) and antiparallel (a) alignment of tip and island magnetization. The feedback loop was opened at 1.1 V and 1 nA for all spectra.

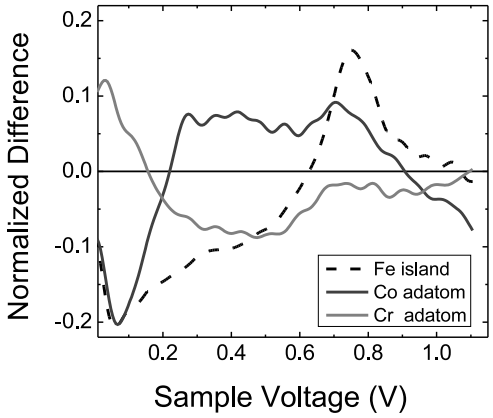

Figure 4.5.: Normalized difference of $\mathrm{d}I/\mathrm{d}V$ spectra shown in Fig. 4.4 for positive voltages. The normalization was performed by calculating the voltage dependent asymmetry according to Eq. (4.2). Prior to normalization, raw data were smoothed.

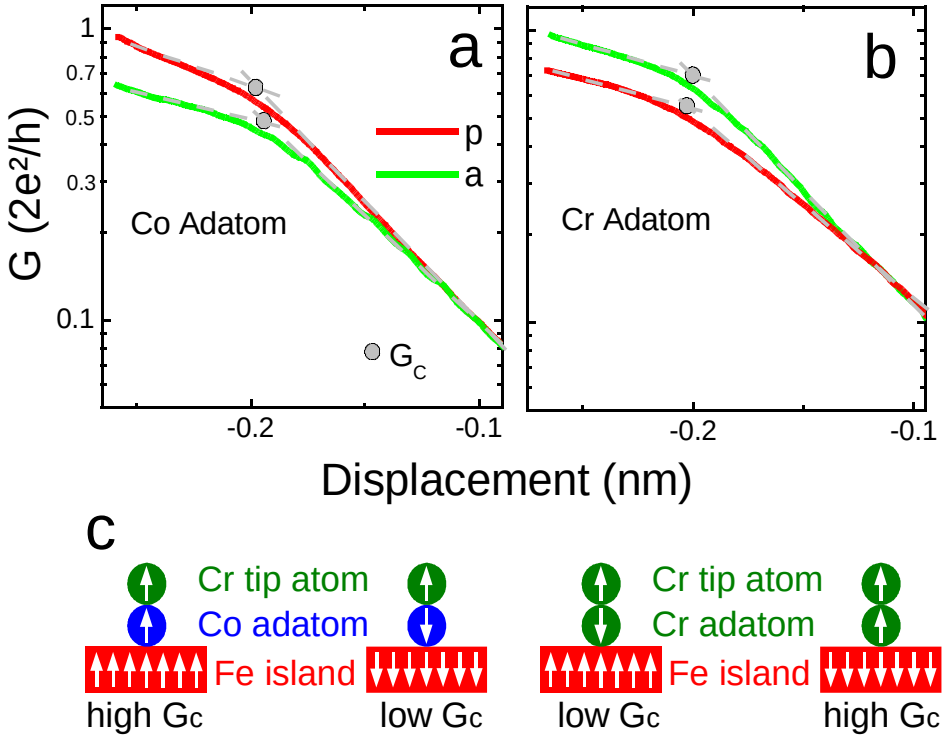

Figure 4.6.: Conductance-displacement curves of (a) Co and (b) Cr adatoms on Fe islands on W(110) with antiparallel (a) and parallel (p) magnetizations with respect to the tip. The tip-adatom distance decreases with decreasing displacement. Zero displacement corresponds to feedback loop parameters of 55 mV and 100 nA. (c) Sketch of junctions.

4.3. Spin polarization in single-atom contacts

In a next step, Co and Cr adatoms on p and a Fe islands were controllably contacted to obtain the electrical conductance of the single-atom magnetic junction. With the established ferromagnetic and antiferromagnetic coupling (see above) the relative orientation of tip and adatom magnetization is either parallel (p) or antiparallel (a). Typical conductance curves are presented in Figs. 4.6(a),(b) for Co and Cr adatoms with parallel and antiparallel alignment of the magnetizations.

Typical conductance curves are presented in Figs. 4.6(a),(b) for Co and Cr adatoms. Deviating from previously reported single-atom contacts [66, 121, 264] the transition from tunneling to contact is considerably less abrupt for Co and Cr adatoms on Fe islands. Therefore, to define the contact conductance, G_c, we determined the intersections of linear fits to conductance data in contact and tunneling regimes rather than in contact and transition regimes [*cf.* conductance curve of Co adatom on p island in Fig. 4.6(a)]. This method gives rise to an accuracy margin of $\approx 0.03\,G_0$.

At 50 mV Co adatoms exhibited a conductance of $\approx 0.64\,G_0$ in case of a parallel alignment between tip and adatom magnetization, while a conductance of $\approx 0.47\,G_0$ was ob-

	50 mV		100 mV	
	G_c^p	G_c^a	G_c^p	G_c^a
Co	0.64 ± 0.05	0.47 ± 0.05	0.46 ± 0.05	0.48 ± 0.05
Cr	0.52 ± 0.05	0.75 ± 0.05	0.53 ± 0.05	0.54 ± 0.05

Table 4.1.: Contact conductances, G_c, in units of $2e^2/h$ for Co and Cr adatoms with parallel (p) and antiparallel (a) orientation of adatom and tip magnetizations.

served for antiparallel alignment. At 100 mV contact conductances are similar ($\approx 0.46\,G_0$ for parallel and $\approx 0.48\,G_0$ for antiparallel alignment). The same trend was observed for Cr adatoms, whose contact conductances are summarized in Table 8.2. The most striking result, which may be inferred from the conductance data is the increase of the conductance by $\approx 36\,\%$ ($\approx 44\,\%$) for Co (Cr) by changing from an antiparallel to a parallel alignment of tip and adatom magnetization. These results demonstrate spin valve behavior of single-atom junctions, *i. e.*, high (low) junction conductance for parallel (antiparallel) alignment of tip and adatom magnetizations. The role of the ferromagnetic Fe islands is to fix the adatom magnetization and to provide the electronic bands for electron transport through the junction.

From Figs. 4.6(a),(b) one additionally infers that conductance traces obtained from adatoms on p and a islands deviate from each other before reaching the contact regime. These deviations may be caused by electrode relaxations due to magnetic forces between probe and adatom, which are different for parallel and antiparallel alignment of the magnetizations. Similar conclusions have been drawn for Fe-coated probes and Fe monolayers on W(001) using magnetic exchange force microscopy [124].

The contact conductances may be interpreted in a minimal model by considering electron transport through two spin-polarized channels. We notice that current-voltage characteristics acquired at contact (not shown) exhibit a similar spin polarization as observed in the tunneling regime. In the model, majority (maj) and minority (min) electrons are considered separately and the spin is preserved during transport between exchange-split electronic bands of the electrodes. Considering sp and d bands as the relevant transport channels in contact and writing the contact conductance as

$$G_c = G_c^{\mathrm{maj}} + G_c^{\mathrm{min}}, \tag{4.3}$$

the conductance due to majority electrons may be identified as

$$G_c^{\mathrm{maj}} = G_{sp}^{\mathrm{maj}} + G_d^{\mathrm{maj}}, \tag{4.4}$$

while for minority electrons the conductance reads

$$G_c^{\mathrm{min}} = G_{sp}^{\mathrm{min}} + G_d^{\mathrm{min}}. \tag{4.5}$$

Calculations of the electronic structure of a Fe double-layer film on W(110) predict that only a minority d band exists at the surface Brillouin zone center around 50 meV above the Fermi level. Therefore, we set $G_d^{\mathrm{maj}} = 0$ and only consider a spin-polarized minority channel with conductance G_d^{min}. All spin-polarized transport channels have a maximum conductance of $G_0/2$. Assuming now a spin-polarized current, the equations for the conductance of a single Co adatom read

$$G_c^{\mathrm{maj}} = 0.47\,G_0 = G_{sp}^{\mathrm{maj}} \tag{4.6}$$

and

$$G_c^{\min} = 0.64\,\mathrm{G}_0 = G_{sp}^{\min} + G_d^{\min}. \tag{4.7}$$

Following Ref. [126], the conductances due to *sp* bands can be expected to be similar for both *p* and *a* alignments, $G_{sp}^{\mathrm{maj}} \approx G_{sp}^{\min}$. To this end, $G_{sp}^{\mathrm{maj}} = G_{sp}^{\min} = (0.47 \pm 0.10)\,\mathrm{G}_0$ and $G_d^{\min} = (0.17 \pm 0.10)\,\mathrm{G}_0$ were obtained. For Cr the results are $G_{sp}^{\mathrm{maj}} = G_{sp}^{\min} = (0.52 \pm 0.10)\,\mathrm{G}_0$ and $G_d^{\min} = (0.23 \pm 0.10)\,\mathrm{G}_0$. At 100 mV Co and Cr adatoms exhibit a contact conductance of $\approx 0.5\,\mathrm{G}_0$, irrespective of the relative magnetization orientation between tip and adatom. This observation may be explained by the absence of *d* bands at 100 meV above the Fermi level [93]. The *sp* channels have to carry the electron flow with a conductance of $G_{sp}^{\mathrm{maj}} = G_{sp}^{\min} \approx \mathrm{G}_0/2$ to obtain the measured contact conductances. Consequently, with the above assumptions the conductance of the single magnetic atom junction may be explained by invoking a majority and minority *sp* and a single minority *d* transport channel. However, energy-dependent transport channel calculations, which consider the fully relaxed magnetic single-atom contact will provide more insight in the number of transport channels and their transmission probabilities.

Summarizing, single magnetic atoms adsorbed on ferromagnetic nanostructures act as spin valves and exhibit high (low) electrical conductance if their magnetization is set parallel (antiparallel) to the magnetization of the contacting electrode. The observed contact conductances were explained by electron transport through spin-polarized *sp* and *d* channels.

Chapter 5.

Picking up Vibrations from a Single Kondo Impurity

The investigation of electronic and vibrational properties of single atoms adsorbed on surfaces has attracted considerable attention recently since a wealth of information may be inferred from these properties. Single adsorbed atoms (adatoms) owing to their attractive potential induce a bound state in a quasi-two-dimensional electron continuum, which is the subject of Sec. 8.3. The spectroscopic lineshape of this state provides access to, *e. g.*, the charge transfer between adatom and substrate or the decay processes of the bound state.

Magnetic adatoms exhibit the Kondo effect, which results from the exchange interaction of the spin of the local magnetic impurity with surrounding conduction electrons. The spectroscopic signature of the Kondo effect is the Abrikosov-Suhl resonance at the Fermi level, which in scanning tunneling spectroscopy appears as a Fano profile [129, 145].

Vibrational spectroscopy using the scanning tunneling microscope has been reported predominantly for molecules [16, 132–137], while only a single study for vibrational modes of single hydrogen and deuterium atoms is available [17]. Inelastically tunneling electrons whose energy exceed the energy of a vibrational mode modify the conductance of the tunneling junction and may give rise to a signal in current-voltage characteristics. According to our current understanding of inelastic electron tunneling spectroscopy (IETS) [18, 19], the vibrational excitation influences the elastic as well as the inelastic tunneling channel. If the related conductance changes happen to compensate, a vibration signal will be absent in the acquired spectra. Modeling IETS data obtained with an STM [18, 19] is based on the Tersoff-Hamann approach [21], which employs an s wave representation of the tip. Up to now, the observation of vibrational signals in IETS is exclusively discussed in terms of a favorable combination of adsorbate and substrate electronic structure [19]. The influence of the electronic structure of the tip to the vibrational signal, however, has not been considered yet.

In this chapter a combined electronic and vibrational structure analysis of single Co atoms adsorbed on Au(110) is presented. In Sec. 5.1 a brief introduction to the basic concepts of IETS is given. Sec. 5.2 is dealing with aspects of the Kondo effect of single adatoms, which are relevant for this thesis. Two novel findings are reported in Sec. 5.3. First, the Co adatoms exhibit the Kondo effect with a Kondo temperature of $(85 \pm 5)\,\mathrm{K}$. Second, the impact of the tip's electronic structure on the observability of vibrational modes in IETS is shown. While the spectroscopic signature of the single-Co symmetric stretch mode stays below the detection limit if gold-covered tungsten tips are used, it appears as a pronounced signal upon utilizing a chemically modified tip with a characteristic electronic structure.

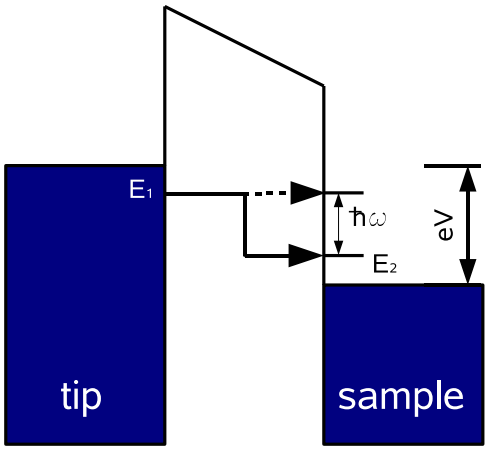

Figure 5.1.: Schematic energy diagram for inelastic electron tunneling between energy level E_1 in the tip and energy level E_2 in a sample. The electron loses energy $\hbar\omega$ to excitation of an oscillator in the barrier region. This can only occur if $eV \geq \hbar\omega$. The Fermi energies are related by $(E_{\mathrm{F}}^{\mathrm{tip}} - E_{\mathrm{F}}^{\mathrm{sample}}) = eV$

5.1. Inelastic electron tunneling spectroscopy

Vibrational modes of adsorbed atoms or molecules on surfaces can be exited by tunneling electrons if the applied bias voltage V exceed the energy $\hbar\omega$ corresponding to the vibrational excitation in the adsorbate. An idealized energy diagram describing such a process is shown in Fig. 5.1(a). Therein two metallic electrodes (tip and sample) are separated by a vacuum gap and the applied bias voltage V leads to a tunneling current between tip and sample, where horizontal transitions from the energy level E_1 of the tip correspond to elastic tunneling. For inelastic transitions the tunneling electron looses parts of its energy during the tunneling process corresponding to an energy loss $\hbar\omega$ and therefore reaches the lower energy level E_2. Certainly, this process can only occur if any empty state in the sample is available for the tunneling electron, i.e. if $eV \geq \hbar\omega$. As the voltage increases, the inelastic current from this state will continue to increase, since more and more electrons for inelastic tunneling are involved. This phenomenon causes an increase in the tunneling current at the voltage $eV = \hbar\omega$.

The magnitude of the change in the tunneling current due to inelastic tunneling through molecules in planar junctions was first theoretically described by Scalapino and Marcus [138]. Their model is based on the WKB approximation, where the inelastic electron-molecule interactions are taken into account by including the molecular dipolar field in such a way that an interaction potential is introduced as perturbation of the barrier height. This perturbation results in tunneling matrix elements for an elastic and inelastic contribution to the tunneling current. By taking into account tunneling in both directions from tip to sample and from sample to tip the inelastic current is given within this model as

$$\begin{aligned} I_{\mathrm{ine}} \quad &= C \int_{-\infty}^{\infty} [f(E - eV + \hbar\omega)(1 - f(E)) + f(E)(1 - f(E - eV - \hbar\omega))] \\ &\quad \times \rho_{\mathrm{S}}(E)\ \rho_{\mathrm{T}}(E - eV)\, \mathcal{T}(E, eV)\ \mathrm{d}E, \end{aligned} \tag{5.1}$$

where C is a constant, ρ_{S} and ρ_{T} are the density of states of the surface and tip, respectively, $\mathcal{T}(E, eV)$ the transmission factor, and $f(E)$ the Fermi-Dirac function defined

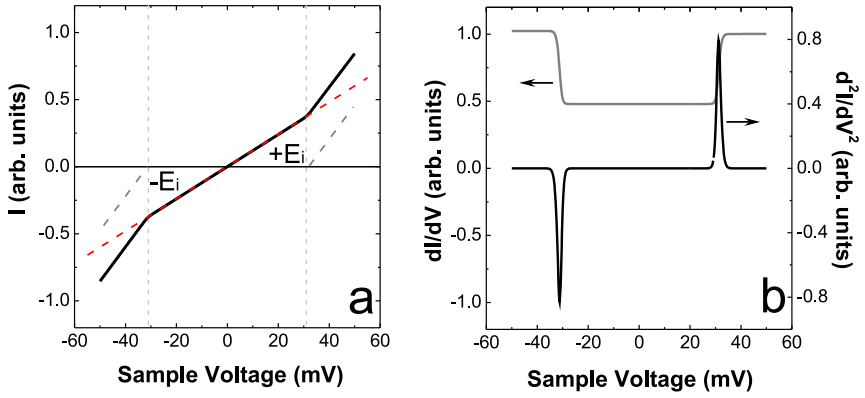

Figure 5.2.: (a): Current-voltage characteristic of an inelastic tunneling process. When the tunneling voltage exceeds the threshold $|eV| = E_i$ an additional tunneling channel opens and the current then consists of an elastic (dashed red line) and an inelastic (dotted gray line) contribution. (b) This change in the tunneling current results in a step like increase in $\mathrm{d}I/\mathrm{d}V$ spectra and a peak will be observed in $\mathrm{d}^2I/\mathrm{d}V^2$ spectra at the voltage $|V| = E_i/e$.

as $f(E) = 1/(1 + \exp(E/k_\mathrm{B}T))$. The total tunneling current, which involves also elastic contributions is then $I = I_\mathrm{ine} + I_\mathrm{el}$ [130], where I_el denotes the elastic tunneling current as defined in Chapter 2 [Eq.(2.7)]. The obtained current-voltage characteristic for a constant tip and sample DOS, as well as in the zero-temperature limit is shown in Fig. 5.2(a). This change in the tunneling current results in a step like increase in $\mathrm{d}I/\mathrm{d}V$ spectra and a peak will be observed in $\mathrm{d}^2I/\mathrm{d}V^2$ spectra at the voltage $V = \hbar\omega/e$, as presented in Fig. 5.2(b). It is important to remark, that this simple model using the assumption that the lifetime τ of the excited state is much smaller than the average time between two tunneling processes. As recently shown by Gupta et al. [139] the obtained spectra can change drastically, when the lifetime of the excited state is comparable or even longer than the average time between two tunneling processes.

While since the pioneering experiment by Jaklevic and Lambe [131] in 1966 much investigations through planar junctions has been taken, the first inelastic tunneling investigation using an STM was reported by Stipe et al. in 1998 [16]. In this work vibrational spectra for an isolated acetylene (C_2H_2) molecule and for a deuterated acetylene (C_2D_2) molecule adsorbed on Cu(100) are obtained, where in the spectra the C-H and C-D stretch modes are visible at 358 mV and 266 mV, respectively. Moreover, using the imaging capability of an STM these two isotopes can be distinguished, since in constant-current STM images recorded at 358 mV and 266 mV a vibrational signal is expected only at the site of the corresponding molecule.

However the above mentioned theoretical approach from Scalapino and Marcus is not able to give an answer to the question why exclusively the C-H (C-D) stretch mode of C_2H_2 (C_2D_2) on Cu(100) is observed and why the other modes like the C-C stretch mode or the C-H bend mode are missing in the spectra. To this end a more realistic theoretical approach to IETS was given by Lorente and Persson [18], which answers these questions [19]. In their model the total measured conductance is the sum of positive

inelastic and negative elastic contributions to the tunneling conductance, which is nearly vanishing for all the modes expect for the C-H (C-D) stretch mode on Cu(100). In detail, their model is based on the Tersoff-Hamann approach, where the density of states of the sample ρ_S at the position of the tip apex $\mathbf{r_0}$ is given by

$$\frac{\mathrm{d}I}{\mathrm{d}V} \propto \rho_S(\mathbf{r_0}, E_F + eV). \tag{5.2}$$

In the absence of electron-vibration coupling, the LDOS is given in density functional theory as,

$$\rho_0(\mathbf{r}_0, E) = \sum_\mu |\langle \mu | \mathbf{r}_0 \rangle|^2 \, \delta(E - E_\mu), \tag{5.3}$$

where E_μ is the energy of the one-electron state $|\mu\rangle$. The vibrational excitation now modifies $\mathrm{d}I/\mathrm{d}V$ and thus ρ_S, where the change in the density of states can be written as

$$\Delta\rho_S = \Delta\rho_{in} + \Delta\rho_{el} \tag{5.4}$$

While here the elastic contribution $\Delta\rho_{el}$ is induced by virtual vibrations, which are emitted and reabsorbed again, $\Delta\rho_{in}$ denotes the inelastic contribution. The physical meaning of the inelastic contribution are most visible in the quasistatic limit, $\hbar\omega \to 0$, where first order perturbation theory shows that $\Delta\rho_{in}$ is given by

$$\Delta\rho_{in} = \delta Q^2 \sum_\mu \left| \left\langle \frac{\partial \mu}{\partial Q} \,|\, \mathbf{r}_0 \right\rangle \right|^2 \delta(E_F - E_\mu), \tag{5.5}$$

where Q is the vibrational displacement and $\delta Q^2 = \hbar/(2M\omega)$ is the mean square amplitude of Q with the ion mass M. This expression has been already found in 1979 by Kirtley and Soven [140] and shows that the vibrational excitation probability involves matrix elements of the change in the tunneling amplitude, where the distance between vibrational ground state and its first excited state originates from the vibrational displacement Q.

At this point we can conclude that STM based on inelastic tunneling spectroscopy is a powerful tool for the analysis of adsorbates on surfaces. However, vibrational spectroscopy investigations with an STM have been used predominantly for molecules and only a single study for vibrational modes of single hydrogen and deuterium atoms is available [17].

5.2. The Kondo effect on single adatoms

In pure metals the electrical resistance monotonically decreases with decreasing temperature to a saturation resistance due to electron scattering at impurity sites, which is damped at low temperatures. However, in some metals, which contain magnetic impurities, the electrical resistance increases again below a certain temperature. This experimental finding is called the Kondo effect and can be explained with a scattering model introduced by Kondo [141], which will be described in the following. The aim of this section is to give a brief introduction to this topic focusing mainly on the important aspects for this thesis. For a more detailed description the reader is referred to Refs. [142, 143].

The Kondo effect arises in metallic systems with magnetic impurities, where the total spin of all the electrons in the impurity is non-zero. The most intuitive approach to describe such a system is given by the *Anderson single impurity model* [144] similiar to the Newns-Anderson model presented in Sec. 8.3.4. In the model discussed here a single

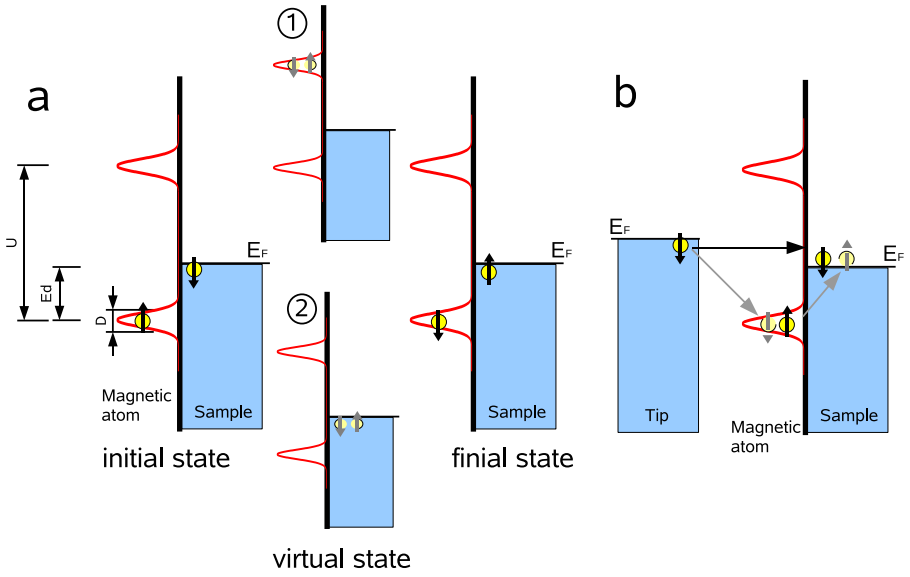

Figure 5.3.: Schematics of the energy dependent DOS in the Anderson model of a magnetic impurity on a metal surface adapted from [143]. (a) The spin of the occupied state can flip by scattering with a bulk electron of opposite spin in two processes labeled as (1) and (2). (b) Electrons from the tip can tunnel to the sample by conserving their spin, or via a spin flip process through the magnetic atom.

electron level E_d can be filled with one, two, or no electrons. The interaction of the impurity state with the continuum of band states of the metallic host is described by the coupling matrix elements V_{ak}, and results into a broadening of this state by $\Delta = \rho_0 |V_{ak}|^2$, where ρ_0 is the substrate DOS at the Fermi level [see Sec. 8.3.4].

In exchange processes the spin of the magnetic impurity can flip from spin up to spin down, or vice versa, while simultaneously a virtual state close to the Fermi energy is created. This process is schematically drawn in Fig. 5.3(a). The single electron level E_d is occupied by one spin-up electron. Adding a spin-down electron from the metallic host the spin-up electron can tunnel out of the impurity state to briefly occupy a *virtual state* and then be replaced by the spin-down electron, whereby the spin of the impurity is reversed. In fact, classically such a process is forbidden, since it requires to overcome an energy barrier of several eV, which is given by the Coulomb repulsion energy U between the occupied and unoccupied states of the magnetic impurity resonance. However, the Heisenberg uncertainty principle allows such a process on a very short time scale of around $h/|E_d|$.

The spin exchange process modifies the excitation spectrum of the system. In particular, taking many of such processes together a new state is generated very close the Fermi level, the so-called Abrikosov-Suhl resonance, which is also known as Kondo resonance. Since many electrons are needed, the Kondo effect is a many-body phenomenon.

The half-width at half-maximum Γ of the Abrikosov-Suhl resonance near the Fermi energy can be described at $T = 0\,\mathrm{K}$ by the so-called Kondo temperature

$$T_\mathrm{K} = \frac{\Gamma}{k_\mathrm{B}} \approx \Gamma \times 11.6\,\mathrm{meV}^{-1} \tag{5.6}$$

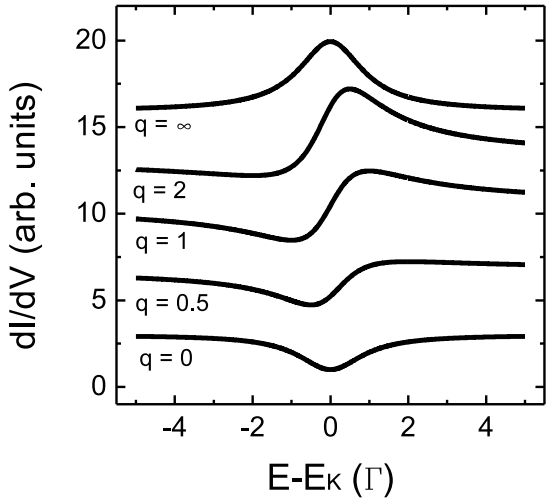

Figure 5.4.: Evolution of the Fano line shape for different values of the form factor q (see Eq. (5.8)). While at $q = 0$ the Fano line shape corresponds to a Lorentzian dip, at $q \to \infty$ a Lorentzian peak is equivalent to the Fano profile.

and can be related to the parameters of the Anderson model by

$$\Gamma = k_{\mathrm{B}}\, T_{\mathrm{K}} \cong \sqrt{\frac{2\Delta U}{\pi}}\, \exp\left[-\frac{\pi}{2\Delta}\left(\left|\frac{1}{E_d}\right| + \left|\frac{1}{E_d + U}\right|\right)^{-1}\right]. \tag{5.7}$$

The STM enables the measurement of the Abrikosov-Suhl resonance [129, 145]. But, instead of a peak a dip-like structure at E_{F} is usually observed in STS measurements [see Fig. 5.6(a)]. This behavior can be understood with the help of Fig. 5.3(b). Therein a magnetic adatom is placed on a metal surface, which results in a localized adatom state at E_d below the Fermi energy. Electrons originating from the tip have now two possibilities to tunnel into the sample. First, they can tunnel directly into empty bulk states above E_{F} of the metal sample [horizontal path in Fig. 5.3(b)] or second, they can tunnel via the above described spin-flip process into the localized state of the magnetic adatom [second mentioned path in Fig. 5.3(b)]. The probabilities of the respective paths can be described by energy-independent tunneling matrix elements t_1 and t_2 for the direct and indirect path, respectively. As a result, the tunneling current is determined by the coherent quantum interferences between both paths. Fano showed that then the detected line shape of the Abrikosov-Suhl resonance has the form

$$\rho(E) \propto \rho_0 + \frac{(q + \epsilon)^2}{1 + \epsilon^2}, \tag{5.8}$$

where ϵ is the normalized energy $\epsilon = (E - E_{\mathrm{K}})/\Gamma$ (E_{K} is the resonance position close to E_{F} and Γ its half-width at half maximum) and q is the form factor, which is given by the ratio between the direct and the indirect tunneling probabilities

$$q \propto \frac{t_2}{t_1}. \tag{5.9}$$

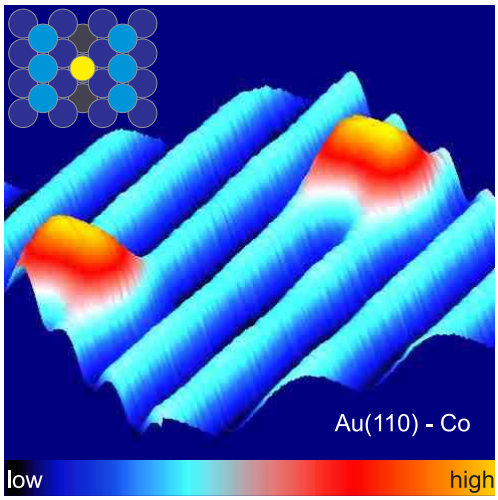

Figure 5.5.: Pseudo-three-dimensional representation of a constant-current STM image of two Co atoms residing in the missing rows of surface-reconstructed Au(110) (sample voltage: 50 mV, tunneling current: 0.1 nA, size: 5 nm × 5 nm). Inset: Sketch of suggested adsorption geometry. The Co atom (bright) adsorbs in the center of the missing row and is coordinated by five substrate atoms.

In particular, q determines the line shape of the spectra, as shown in Fig. 5.4, where the curves correspond to Lorentzian dip for $q = 0$ and to a Lorentzian peak if $q \to \infty$.

5.3. Vibrations from single Co atoms

In the following section the spectroscopic signatures of individual Co atoms on Au(110) are studied. To this end, single Co atoms were deposited onto the cold surface from an evaporant of 99.99 % purity using an electron beam evaporator. In the course of the experiment the tip was controllably indented into the surface to optimize imaging and spectroscopy. Owing to this *in vacuo* treatment the tip apex is most likely covered with substrate material.

Figure 5.5 shows a pseudo-three-dimensional representation of a constant-current scanning tunneling microscopy (STM) image of two single Co atoms adsorbed on Au(110). The majority (> 95 %) of Co atoms, which appear as protrusions in STM images, reside in the (1×2) reconstructed surface [146, 147, 191, 194] as described in detail in Chapter 7. The atoms are adsorbed on top of a Au atom of the missing row, as shown in the inset of Fig. 5.5.

Spectra of $\mathrm{d}I/\mathrm{d}V$ of single Co atoms show a sharp indentation at the Fermi level [Fig. 5.6(a), zero sample voltage]. We interpret this feature as the Abrikosov-Suhl resonance, which is induced by the Kondo effect. To analyse the resonance in more detail we fit a Fano line shape [149] according to Eq. (5.8) to the spectroscopic data. The fit is added as a solid line to Fig. 5.6(a). From this fit we extract $T_\mathrm{K} = (85 \pm 5)\,\mathrm{K}$ and $q = (0.3 \pm 0.1)$.

Vibrations of the single Co adatom may be excited by inelastically tunneling electrons. To push the vibrational signal above the detection limit, the inelastic contribution to the tunneling conductance must dominate the elastic contribution [18]. In this case the spectroscopic signature of the vibration appears as a peak (or an indentation) in the second

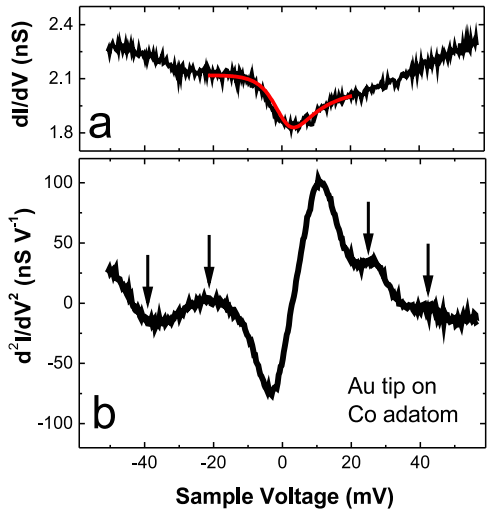

Figure 5.6.: (a) Spectrum of $\mathrm{d}I/\mathrm{d}V$ taken with a gold-covered tungsten tip on a single Co adatom (feedback loop parameters: 55 mV, 10 nA). Full line: Fit according to Eq. (5.8) to data with fit parameters $T_\mathrm{K} = (85 \pm 5)\,\mathrm{K}$, $q = 0.3 \pm 0.1$, $E_\mathrm{K} = -3.5\,\mathrm{meV}$. (b) Spectrum of $\mathrm{d}^2I/\mathrm{d}V^2$ acquired with a gold-covered tungsten tip on a single Co adatom (feedback loop parameters: 55 mV, 10 nA). The prominent signature around 0 mV is the derivative of the Abrikosov-Suhl resonance induced by the single-Co Kondo effect. Additional spectroscopic features are indicated by arrows.

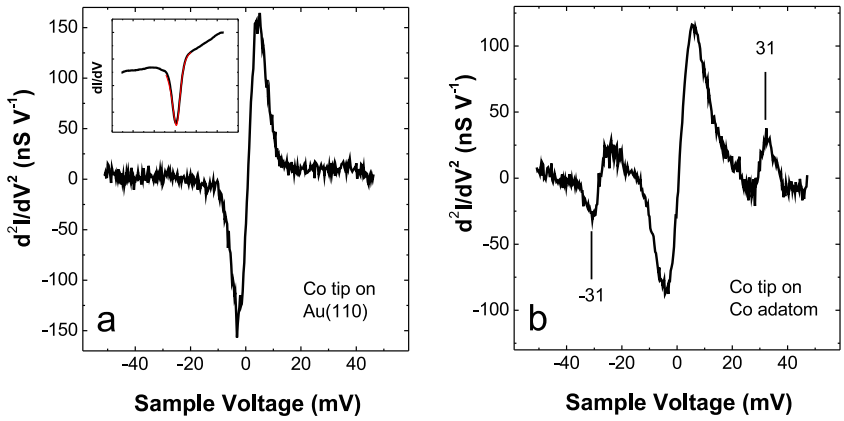

Figure 5.7.: (a) Spectrum of $\mathrm{d}^2I/\mathrm{d}V^2$ acquired with a chemically modified tip on clean Au(110) (feedback loop parameters: 50 mV, 10 nA). Inset: Numerical integration of spectroscopic data displayed in (a). The full line represents a fit to data according to Eq. (5.8) with fit parameters $T_\mathrm{K} = (59 \pm 5)\,\mathrm{K}$, $q = 0.2 \pm 0.1$, $E_\mathrm{K} = 1.4\,\mathrm{meV}$. (b) Spectrum of $\mathrm{d}^2I/\mathrm{d}V^2$ acquired with a chemically modified tip on a single Co adatom (feedback loop parameters: 50 mV, 10 nA). The indentation at -31 mV and the peak at 31 mV are assigned to the spectroscopic signature of the single-Co symmetric stretch mode, while the prominent feature around 0 mV is the derivative of the Abrikosov-Suhl resonance.

derivative of the current with respect to the voltage, *i. e.*, $\mathrm{d}^2I/\mathrm{d}V^2$. Figure 5.6(b) shows a spectrum of $\mathrm{d}^2I/\mathrm{d}V^2$ acquired on top of a Co adatom with the same tip, which was used to monitor the Abrikosov-Suhl resonance displayed in Fig. 5.6(a). As expected, the pronounced signal around zero voltage is the derivative of the Abrikosov-Suhl line shape. In the spectrum additional features appear at positions indicated by arrows. Since they do not appear at symmetric energies with respect to zero sample voltage a vibrational origin for these spectroscopic signals is very unlikely.

Occasionally, the tip apex was modified by an impurity, which changed the electronic structure of the tip in a characteristic way. Figure 5.7 shows a spectrum of $\mathrm{d}^2I/\mathrm{d}V^2$ acquired with the modified tip on clean Au(110). The signature around zero voltage, which is not present for spectra of $\mathrm{d}^2I/\mathrm{d}V^2$ taken with a clean tip, is interpreted as the derivative of the Abrikosov-Suhl resonance [see inset of Fig. 5.7(a)] of a Co atom adsorbed at the tip apex. Other origins are excluded by the same arguments used to corroborate the Kondo effect of Co atoms adsorbed on Au(110). Fitting a Fano line shape according to Eq. (5.8) to the spectroscopic $\mathrm{d}I/\mathrm{d}V$ data displayed in the inset of Fig. 5.7(a), we obtain a Kondo temperature of $(59 \pm 5)\,\mathrm{K}$ and an asymmetry parameter of $q = 0.2 \pm 0.1$. Since the indentation ($\approx -3.2\,\mathrm{mV}$) and the peak ($\approx 4.5\,\mathrm{mV}$) are not symmetric with respect to zero sample voltage a vibrational origin can be excluded. Using this chemically modified tip we performed vibrational spectroscopy on a single Co adatom. The result is presented in Fig. 5.7(b). The most striking observation is the occurance of an indentation and a peak at $\approx -31\,\mathrm{mV}$ and at $\approx 31\,\mathrm{mV}$, respectively. These signatures are not present in $\mathrm{d}^2I/\mathrm{d}V^2$ spectra of the Co adatom acquired with a clean tip [Fig. 5.6(b)], nor do they appear in $\mathrm{d}^2I/\mathrm{d}V^2$ spectra taken on clean Au(110) with the chemically modified tip [Fig. 5.7(a)].

We assign these features to the spectroscopic signature of the single-Co vertical vibration mode, which is also referred to the symmetric stretch mode. Preliminary calculations for a Co atom residing in the missing row of Au(110) as illustrated in the inset of Fig. 5.5 reveal an energy of this vibration mode of $\approx 26\,\mathrm{meV}$. Additional indications, which corroborate our assignment, are provided by calculations of vibration energies of Co adsorbed on Cu(111) [154,155]. The vertical vibration modes are found at 33 meV [154] or 38 meV [155] depending on the employed calculation scheme. Moreover, possible contributions from frustrated translation modes may be buried in the strong signal originating from this resonance. The energies of frustrated translation modes of Co on Cu(111) were calculated to be in the range of 5 meV [154, 155]. The stronger spectroscopic feature extending from $\approx -20\,\mathrm{mV}$ to $\approx 20\,\mathrm{mV}$ in Fig. 5.7(b) corresponds to the derivative of the Abrikosov-Suhl resonance profile. Fits to $\mathrm{d}I/\mathrm{d}V$ data according to Eq. (5.8), which we do not show here resulted in a Kondo temperature of $(97 \pm 5)\mathrm{K}$ and an asymmetry factor of $q = 0.2 \pm 0.1$. Compared to T_K of a Co adatom extracted from $\mathrm{d}I/\mathrm{d}V$ data recorded with a clean Au-covered tip, the present Kondo temperature is slightly increased. This broadening is mainly due to the tip density of states, which contains a Fano-type resonance at $\approx 0\,\mathrm{V}$ [inset of Fig. 5.7(a)]. By simulating the tunneling current, a convolution on the basis of two Abrikosov-Suhl resonance profiles for tip and sample were performed at first. The results are shown in Fig. 5.8. If we assume for both profiles of tip and sample, respectively, the above extracted Fano line shapes, the convolution procedure yields a Kondo temperature of $(105 \pm 5)\,\mathrm{K}$ for the convoluted profile [bottom curve Fig. 5.8(a)]. This Kondo temperature is in good agreement with $(95 \pm 5)\,\mathrm{K}$ extracted from spectra recorded with a modified tip on a single Co adatom. By using Eq. (5.1) the lineshape of the inelastic contributions to the tunneling current can be analyzed in detail and the obtained results are presented in

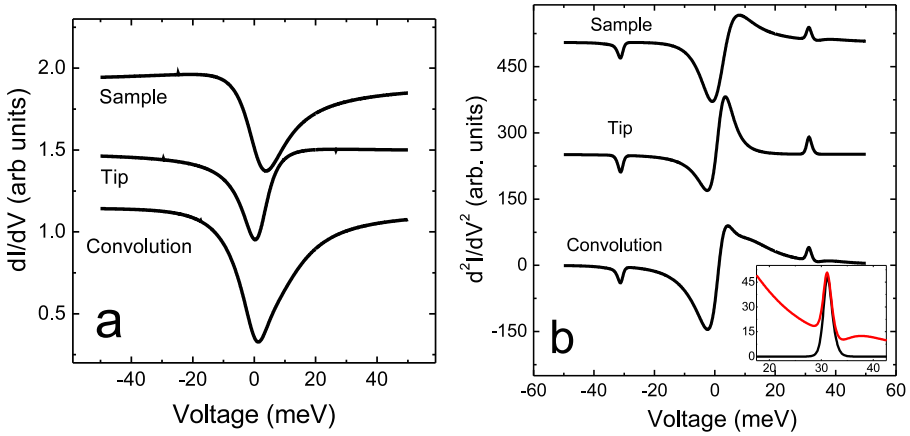

Figure 5.8.: Calculated tunneling spectra: (a) Convolution on the basis of two Abrikosov-Suhl resonance profiles extracted from experimental spectra of $\mathrm{d}I/\mathrm{d}V$ for a single Co atom adsorbed on Au(110) measured with a gold-covered tip apex, and for clean Au(110) measured with a tip apex terminated with a Co atom. (b) Convolution results for $\mathrm{d}^2I/\mathrm{d}V^2$ spectra according to Eq. (5.1), which confirms that vibrational signature is not destroyed by the Kondo effect. Inset: $\mathrm{d}^2I/\mathrm{d}V^2$ spectra of, respectively, the vibrational mode (black line) and their convolution with Fano profile caused by a Co atom terminated at the tip apex (red line). Data are vertically shifted for clarity.

Fig. 5.8(b). As a result we found that the energy position of the vibrational excitations remains to be unchanged after the convolution procedure, while their lineshape is slightly affected, as shown in the inset of Fig. 5.8(b).

Since two Co atoms — one tip apex atom and one adatom on Au(110) — are involved in the data acquisition a possible magnetic effect may be at the origin of the 31 meV excitation. However, this energy is by far too large to be related to magnetic excitations. Magnetic anisotropy energies for single Co atoms on Pt(111), which represents a magnetically strongly coupled system have been determined to be in the range of 5 to 10 meV [152]. Further, the exchange interaction between the Co atoms should be negligible at typical tip-adatom distances in the tunneling regime (≈ 0.7 nm, [264]). In a recent *ab initio* calculation [153] the exchange interaction between a Cr atom at the apex of a Cu tip and Cr, Mn, Fe, Co adatoms on Cu(100) have been determined as a function of the tip-adatom distance. For distances exceeding 0.6 nm the exchange interaction energies are close to zero.

Additionally, spin flip processes via the Kondo effect may influence the spectroscopic lineshape and lead to a phonon-assisted Kondo effect. The underlying physics of a phonon-assisted Kondo effect can be understood with the help of Fig. 5.9(a). The single electron level E_d is occupied by one spin-up electron. If a spin-down electron is added from the probing tip by emitting a phonon, the spin-up electron can only tunnel out of the impurity state to briefly occupy a *virtual state*, if the applied bias voltage V reaches the energy $eV \approx \hbar\omega$ corresponding to the vibrational excitation in the adsorbate. This fact simply results from the energy conservation law, which must be satisfied in the exchange process,

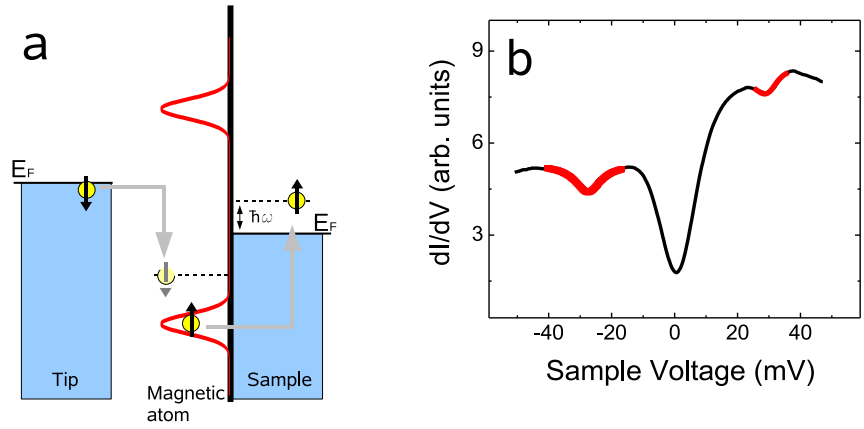

Figure 5.9.: (a) Schematic illustration for the spin exchange processes in phonon-assisted Kondo tunneling. Due to energy conservation the spin-up electron can only tunnel out of the impurity state, if the applied bias voltage V reaches the energy $\hbar\omega$. (b) Numerical integration of spectroscopic data displayed in Fig. 5.7(b). The red full lines represent fits to data according to Eq. (5.8) with fit parameters $T_K = (58 \pm 5)\,\mathrm{K}$, $q = 0.01 \pm 0.05$, $E_K = -27.5\,\mathrm{meV}$ for the dip at negative bias and $T_K = (58 \pm 5)\,\mathrm{K}$, $q = 0.3 \pm 0.1$, $E_K = 30.1\,\mathrm{meV}$ for the peak at positive bias.

whereby a phonon adsorption is unavailable at low temperatures. As a result, additional Kondo signatures appear in the tunneling spectra at the energy positions of the vibrational excitation.

In the field of molecular transistors the interplay of the electron-phonon coupling and the Kondo effect has attracted a lot of attention [156–159]. In particular, the Abrikosov-Suhl resonance has been found to break up into a number of vibron sidebands, whereby the vibrational excitations are not destroyed by the Kondo effect. In a recently published STM investigation [160] on organic molecules grown on salt in top of an Au(111) sample it was shown that the combination of inelastic tunneling electrons and the Kondo effect results in a number of vibron sidebands, which show a Fano lineshape.

In order to analyze our observed features at $\pm 31\,\mathrm{mV}$ with respect to a phonon-assisted Kondo effect, Fano profiles according to Eq. (5.8) are fitted to the experimental spectra. The results are presented in Fig. 5.9(b). From this fits we extract a Kondo temperature of $(58 \pm 5)\,\mathrm{K}$ for both polarities, which is quite similar to the above extracted Kondo temperature of the Co atom on the tip apex. However, while the presented convolution procedure and the phonon-assisted Kondo effect reproduce the experimental observed lineshape of the vibrational excitation, they can not describe why tips with a single Co atom on their apex show the spectroscopic signature of the symmetric stretch mode.

Nevertheless, our experimental investigation clearly shows that the vibrational signal may be pushed above the detection limit by modifying the tip apex with a Co atom. The most evident difference between a Co atom and a Au atom is given by their outermost atomic shell. While for a Au atom a single s shell has to be taken into account, the Co atoms exhibits a half filled d orbital as outermost shell. By using Eq. 5.1 this difference

can be taken into account by using for a clean Au covered-tip a s tunneling matrix element

$$\mathcal{T}_s = C\,\psi(\mathbf{r_0}), \tag{5.10}$$

and for a tip with a Co atom on their apex a d tunneling matrix element

$$\mathcal{T}_d = C\left(\frac{\partial^2}{\partial z^2} - \frac{1}{3}\kappa^2\right)\psi(\mathbf{r_0}), \tag{5.11}$$

where $\psi(\mathbf{r_0})$ is the tip wave function, κ the wave vector, and C a constant. With the help of this matrix elements the inelastic tunneling current I_{in} and their second derivative $\mathrm{d}^2 I_{\mathrm{in}}/\mathrm{d}V^2$ were calculated according to Eq. (5.1). By comparing the obtained change in the magnitude of the vibrational signature a difference of only 0.01 % can be observed, which can not describe the experimental observed difference. However, in the used simple WKB model the explicit local density of states of both electrodes are not taken into account. Furthermore, in the above mentioned theory of IETS from Lorente and Persson [18], the balance of positive inelastic and negative elastic contributions to the tunneling conductance is found to be important to observe vibrational excitation in tunneling spectra recorded with an STM. But even in this more realistic approach, the tip electronic structure is respresented by a s wave and thus does not explicily enter in the variation of the local density of states induced by the electron-vibration coupling. Since according to our experimental results, the tip electronic structure plays a decisive role in detecting vibrational signals, we suggest transport calculations, which track tunneling conductance changes as the result of adatom vibrations probed by a d (rather than an s) orbital.

In conclusion, single Co atoms adsorbed on Au(110) exhibit the Kondo effect. Vibrations of the Co adatom stay below the detection limit when probed with a gold-covered tip apex, while a tip apex terminated with a Co atom gives rise to the observation of the Co symmetric stretch mode.

Chapter 6.

Theoretical Toolbox

Precise control over the geometric, electronic, and magnetic structures at the atomic scale is one of the most challenging tasks in modern nanosience. A detailed understanding of the growth mechanism is essential for a future engineering of nanostructures, which implies a close collaboration of experimental and theoretical investigations.

The focus of interest by using numerical methods in this thesis is on the simulation of diffusion processes of individual atoms to build small clusters of magnetic atoms, as discussed in Chap. 7, and hexagonal ordered adlattices on surfaces, which is reported Chap. 8. The dynamics of such processes occur very rarely on a microscopic time scale and many unsuccessful attempts have to be performed before eventually the corresponding energy barrier is crossed. In order to simulate such dynamical processes molecular dynamical simulation (MD) is often used. In MD the classical equations of motion are propagated forward in time. Since all events to cross the barrier are taken into account, MD is typically limited to a time scale of picoseconds. But the time interval between two successful events can easily reach an order of one microseconds or even longer. Kinetic Monte Carlo (KMC) attempts to overcome the time scale limitation by utilizing the fact that diffusion typically consists of jumps from one state of the system to another state.

However, the study of dynamical processes on crystal surfaces involve the knowledge of diffusion barriers. In order to calculate such barriers density functional theory (DFT) is often used. But, DFT is computationally expensive, which often limits the systems to small supercells. The tight-binding method (TB) can overcome this limitation and can give an acceptable information of band structures of most transition metals. In order to study the formation of crystal structures the total energies rather than just band energies must be obtained. To ascertain the energies of atoms and clusters on surfaces *ab-initio*-based many-body interatomic potentials formulated in the second moment of tight-binding approximation can be used. [172, 173]

In this chapter, the numerical methods are presented, which have been implemented to understand our experimental findings described in Chapter 8 and 7. In detail, Sec. 6.1 is dealing with the kinetic Monte Carlo approach, while in Sec. 6.2 the tight-binding method in the second-moment approximation is presented.

6.1. Kinetic Monte Carlo method

In this section a brief introduction to the KMC approach is given, focusing mainly on the important aspects for this thesis to describe in Chaps. 8 and 7 the diffusion of individual atoms on surfaces. For a review the reader is referred to [161].

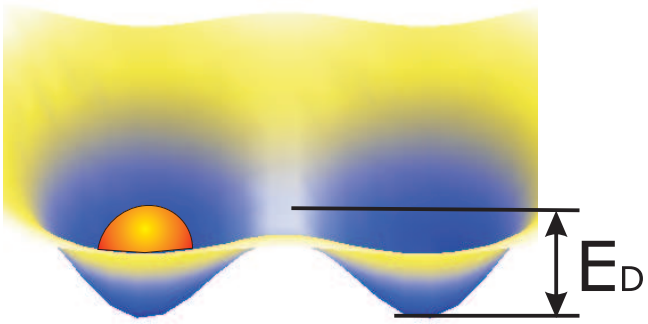

Figure 6.1.: Schematic illustration of the escape process between to locally stable states of the system. The system has to overcome an energy barrier E_{D} to go from the initial state into a new state

6.1.1. The Master Equation

The dynamics of a system is characterized by the occasional transition from one state to another, where each state i of the system is defined by the geometrical position of all particles on the underlaying potential-energy surface. In principle, not single particles are moved to new states, the entire system is moved. But for simplicity it will be assumed in the following that each state corresponds to a single energy basin, and the system must surmount an energy barrier E_{D} to go from one basin to another, as shown in Fig. 6.1. To move now the system from state i to a new state j the system has to find a trajectory out of the initial minimum. After many vibrational periods (attempts) a saddle point (transition state) is perhaps crossing. The key property is that the time of one vibrational event is much smaller than the time to go from one basin to another. The system therefore forgets how it got to a current state. This property, that the transition probability of exiting a state has nothing to do with its history, is known as *Markov process*. Hence, a simple stochastic procedure to let the system propagate from state to state can be constructed. Moreover, if the transition rate of every state is exactly known, the obtained trajectory will be indistinguishable from the exact trajectory of the system, generated for example with the help of a full molecular dynamic simulation.

In order to describe the transition process in a stochastic procedure, the probability P_i that the system is still in a current state i at time $t + \Delta t$ is expressed as

$$P_i(t + \Delta t) = \sum_j W_{i \to j}(\Delta t)\, P_i(t). \tag{6.1}$$

Here $W_{i \to j}$ is the probability that the system will undergo a transition from state i to state j at time $t + \Delta t$ and $P_i(t)$ is the probability that the state is occupied at the initial time t. In particular, to obtain the time dependence of the probability distribution $P_i(t + \Delta t)$

the time derivative is calculated leading to the differential equation

$$\frac{\partial P_i(t)}{\partial t} = \sum_j \left[W_{j\to i}\, P_j(t) - W_{i\to j}\, P_i(t) \right]. \tag{6.2}$$

This equation is called a *Master equation*, since it gives a dynamical interpretation of physical processes. The solution of this equation is obtained numerically by choosing randomly among various possible transitions the appropriate transition. At a steady state the time derivative of the probability distribution $P_i(t)$ is zero and the so-called detailed-balance criterion,

$$\frac{W_{j\to i}}{W_{i\to j}} = \exp\left(\frac{-(H_i - H_j)}{k_{\mathrm{B}} T}\right), \tag{6.3}$$

must be satisfied. Here H is the Hamiltonian of the system and $P_i(t)$ was assumed to be describable by the Boltzmann statistic, where k_{B} is Boltzmann's constant and T the surface temperature. In Monte Carlo simulations the transition probabilities must be constructed in this way, that the thermal equilibrium is guaranteed and the detailed-balance criterion is satisfied.

6.1.2. Canonical MC: The Metropolis algorithm

The *Metropolis algorithm* was already presented in 1953 by Nicholas Metropolis et al. [162] and is the most widely used MC simulation scheme. In particular, it is based on thermodynamics of a canonical ensemble, where the number of particles, system volume, and temperature are conserved and the density probability follows a Boltzmann distribution. The key point of the algorithm is evident from Eq. (6.2). In fact, the transition from one state to another depends only on the previous events. Hence, it is sufficient to consider only transitions between the new and the previous state, rather than the transition of the whole system. In the Metropolis algorithm this is done in a way which leads to the desired probability as presented in the following. Consider a system of N particles depending on their location $x = x_1, ..., x_N$, where for instance the particle i is located at the position x_i. The Metropolis algorithm can then be expressed as:

1. Choose a particle i at random among the N particles
2. Calculate the energy E_b of the system before the transition
3. Generate a uniform random number r between 0 and 1
4. Displace atom i by $\Delta x_i = (2r - 1)\,\delta$, where δ is a chosen distance
5. Calculate the energy E_a of the system after the transition
6. Calculate $\Delta E = E_a - E_b$, then:
   - If $\Delta E < 0$ accept the state
   - If $\Delta E > 0$:
     - Generate a random number r between 0 and 1
     - Accept the state only if $r < \exp(-\Delta E / k_{\mathrm{B}} T)$
7. If the state is rejected keep the previous state.

8. Return to step 1

It is quite evident that the Metropolis algorithm satisfies the detailed-balance criterion. However, there is no time scale involved in this algorithm. Even though the number of Monte Carlo steps are counted, it is not clear at all whether these correspond to any real time scale.

As proved by Fichthorn and Weinberg [167] the kinetic Monte Carlo approach can overcome this limitation. In detail, it satisfies the detailed-balance criterion and involves a physical time scale.

6.1.3. State-to-state dynamics: The KMC concept

Due to the fact that the time scale to enter a current state is short compared to the the time it takes to find out a trajectory of this state, the system loses its memory of how it entered the current state. In particular, in every short time interval the system has the same probability of exiting its current state as it had in the previous time interval. Hence, the system can be described as a Poisson process with a exponential decay statistics. Therefore, the system has the probability

$$P_{\text{state i}}(t) = \exp(-k_{\text{tot}}\, t) \tag{6.4}$$

to have not yet escaped from its current state, where k_{tot} is the total escape rate. The particular interest is, of course, to know the probability $P(t')$ for the time t' of the first escape from the state. To this end, the probability that the system escaped from its current state is given by the integral of $P(t)$ to the time t', which is equal to $1 - P_{\text{state i}}(t')$. Hence, $P(t)$ can directly be calculated from $P_{\text{state i}}$ by taking its negative time derivative according to

$$P(t) = k_{\text{tot}} \exp(-k_{\text{tot}}\, t). \tag{6.5}$$

The average time τ for the escape can be obtained by

$$\tau = \int_0^\infty P(t) t \, \mathrm{d}t = \frac{1}{k_{\text{tot}}}. \tag{6.6}$$

Since the escape from a current system can occur along a number of pathways and each pathway has its own rate constant k_{ij} and first-escape time distribution $p_{ij}(t) = k_{ij}\exp(-k_{ij}t)$, the total escape rate must be the sum of all these rates

$$k_{\text{tot}} = \sum_{j=1}^{i} k_{ij} \text{ for } \; i = 1, \ldots, N, \tag{6.7}$$

where N is the total number of transitions.

6.1.4. The KMC procedure

The most simple KMC algorithm can be designed by drawing exponentially distributed random numbers from the distribution $p(t) = k\exp(-kt)$. In detail, by choosing first a random number r in the interval (0,1], and then form

$$t = -\frac{1}{k} \ln(r) \tag{6.8}$$

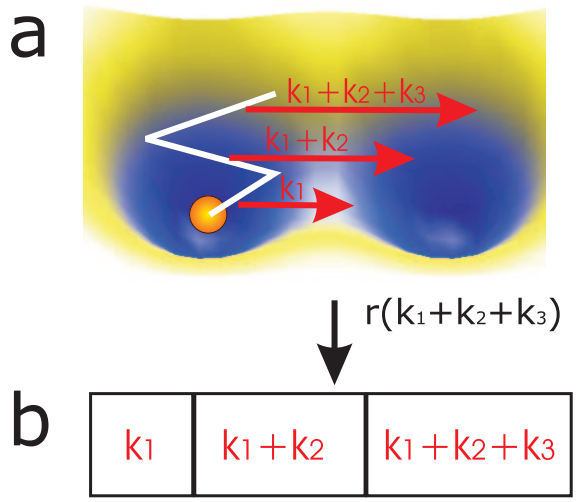

Figure 6.2.: Schematic illustration of the KMC procedure for picking the diffusion pathway to advance the system to the next state: (a) Attempts i to cross the diffusion barrier are illustrated by three lines, where k_i denotes the escape rate to leave the current state. (b) In a computer code a random number r on $(0, 1]$ is generated, multiplied by k_{tot} (here $k_1 + k_2 + k_3$) points to an element in the array with the correct probability.

a realization for the time of the first escape is obtained with a rate constant k. Furthermore, let us assume that all rate constants k_{ij} are known for each state and the system is currently in state i. The exponentially distributed time t_j for each pathway j can then be calculated. The pathway j_{min} is selected which has the lowest value of t_j and the system is moved along j_{min}, whereby the overall system time is updated by t_{min}. Finally, the algorithm begins again in the new state. In principle this is all to construct a KMC algorithm. But, since for every possible path a random number must be generated such a simulation would mean a waste of computer time.

A more efficient stochastic algorithm that will propagate the system from state to state can be designed as one *big Poisson process*, based on multiple independent Poisson processes. This algorithm is known as the *residence-time* algorithm [163,164] or the *n-fold way* or the *Bortz-Kalos-Liebowitz* algorithm [165]. In Fig. 6.2 the pathway selection procedure is schematically indicated. Therein, each pathway to escape a current state is described as a single Poisson process with its own rate constant k_{ij} and first-escape time distribution $p_{ij}(t)$. In order to give a transparent approach to the basic concept of this algorithm, a simple system of three pathway with three transition rates k_1, k_2, k_3 is assumed [see Fig. 6.2(a)]. The key point of the algorithm is to put these transition rates end to end in one array with the total length $k_{\text{tot}} = k_1 + k_2 + k_3$ [see Fig. 6.2(b)]. If we generate a single random number r from the interval (0,1], and multiply it by k_{tot}, this number rk_{tot} will correspond to some point inside the array. Hence, we will obtain the different events with a probability which corresponds to their rate. To advance the overall system time the generated random number r and total escape rate k_{tot} are used to draw a random time from Eq. (6.8). Once the system is in the new state the list of pathways and rates

is updated, and the procedure is repeated. The KMC procedure consists of eight steps, repeated over and over again until the simulation time has been reached. It can be written for instance as follows:

1. Set the time $t = 0$
2. Form a list of all the rates k_{ij} of all possible transitions p_{ij} in the system
3. Calculate total escape rate $k_{\mathrm{tot}} = \sum_{j=1}^{i} k_j$ for $i = 1, \ldots, N$
4. Get a uniform random number r from the interval (0,1]
5. Find the event to carry out i by finding the i for which $k_{i-1} < rk_{\mathrm{tot}} \leq k_i$
6. Carry out event i
7. Get a new uniform random number r from the interval (0,1]
8. Update the time with $t = t + \Delta t$ where: $\Delta t = -\frac{1}{k_{\mathrm{tot}}} \ln(r)$
9. Return to step 1

As a concluding remark, the computing time of this algorithm is $O(N)$, since at least step 2 involves a sum over N elements. This means that we need N operations for every event, which restrict the size, as well as the physical simulation time of the simulated system. But fortunately there are some advantages as it will be discussed below.

6.1.5. Determining the rates

In principle, the KMC approach gives the exact dynamical evolution of a system, when the escape rate for exit from a current state i is exactly known. It is therefore an important task to determine the rate constant for each possible pathway as precisely as possible. From a microscopic point of view it is possible to derive an expression for such rates from the underlying potential energy-surface, which can be done by using transition state theory (TST). [166] In the following the conceptual approximation to a rate constant by using TST will be presented.

The TST rate constant k_{TST} for a one dimensional system can be expressed as the forward flux at the transition state:

$$k_{\mathrm{TST}} = \frac{\left\langle \delta(x) \, \frac{\mathrm{d}x}{\mathrm{d}t} \, \theta(\frac{\mathrm{d}x}{\mathrm{d}t}) \right\rangle}{\langle \theta(-x) \rangle}, \tag{6.9}$$

where the angular brackets indicate the thermal expectation value over the position coordinate x and the momentum p. While θ is the step function defined as 1 for $x > 0$ and 0 for $x < 0$ and $\delta(x)$ is the Dirac distribution. In particular, there are two basic assumption underlying transition state theory: First, it is assumed that there is local thermodynamic equilibrium along the whole diffusion path. Secondly, a recrossing of the energy barrier is not counted, which can lead to an overestimation of the exact rate. This last point is directly coupled to classical mechanics and spotlights the fact that TST is a classical mechanical theory.

In order to derive from TST the rate expression the one-dimensional model from Fig. 6.1 is used. Therefore, a potential $V(x)$ with two potential minima is assumed. Within this model Eq. (6.9) leads to

$$k_{\mathrm{TST}} = \frac{1}{2\pi\hbar\, Z_0} \int \mathrm{d}q\, \mathrm{d}p\ \delta(q)\, p\, \theta(p)\ \exp(-\frac{H(q,p)}{k_{\mathrm{B}}T}), \tag{6.10}$$

where q and p are identified with the position coordinate x and the momentum p, respectively, and Z_0 is the partition sum in the inertial potential minimum. While the integral over the momentum coordinate gives $k_{\mathrm{B}}T$, the integration over q is simply

$$\int \mathrm{d}q\ \delta(q)\ \exp(-\beta V(q)) = \exp(-\frac{E_{\mathrm{D}}}{k_{\mathrm{B}}T}). \tag{6.11}$$

Here E_{D} is the static barrier height. Finally, Eq. (6.9) can be written as

$$k_{\mathrm{TST}} = Z_0^{-1}\ \frac{k_{\mathrm{B}}T}{h} \exp\left(\frac{E_{\mathrm{D}}}{k_{\mathrm{B}}T}\right). \tag{6.12}$$

In the harmonic approximation, which is valid for vibrational energies much smaller than the thermal energy ($\hbar\omega \ll k_{\mathrm{B}}T$), the partition sum in the initial potential minimum Z_0 is given in the classical limit by

$$Z_0 = \prod_{i=1}^{N} \frac{k_{\mathrm{B}}T}{\hbar\omega_0^i} = \frac{k_{\mathrm{B}}T}{\hbar\omega_0}. \tag{6.13}$$

Hence, with the help of the harmonic approximation the expression for k_{TST} can be further simplified and yields

$$k_{\mathrm{TST}} = \frac{\omega_0}{2\pi} \exp\left(\frac{-E_{\mathrm{D}}}{k_{\mathrm{B}}T}\right). \tag{6.14}$$

The prefactor corresponds to an attempt frequency, which counts the number of attempts of the system to cross the energy barrier E_{D}.

In conclusion, in canonical thermodynamical ensembles the probability in a current state to find the system at a dividing surface relative to the probability of being anywhere else can be exploited in the Boltzmann statistic. Classical exact rates can be calculated for each of the pathways in the system.

6.1.6. Technical Implementations

As already above-mentioned the aim of Chap. 8 is to model diffusion processes of Cesium atoms on the Ag(111) surface. In particular, KMC-simulations are used to gain information about the relevant atom-atom interactions to stabilize the experimental observed adlattices, as well as to identify the relevant diffusion processes, which describe the experimental observed adsorbate structures. In the following the important technical implementations of the KMC-code, which was developed for this, are presented.

As mesh for the simulations a two-dimensional hexagonal lattice is used, for which periodic boundary conditions are applied in both lateral directions. The substrate lattice itself is modeled by finite hop rates of adatoms between adjacent lattice sites r_i and r_j, and the hop rates ν_{ij} are described by an Arrhenius law according to Eq. (6.14):

$$\nu_{ij} = \nu_0\ \exp\left(-E_{ij}/\mathrm{k_B}T\right), \tag{6.15}$$

where ν_0 is the attempt frequency and E_{ij} is describing the hopping barrier between two adjacent lattice sites. If we assume that there are no big differences among the attempt rates for a single particle on different lattice sites, a static diffusion barrier between lattice sites i and j can be used. Following Ref. [168] a simple model for E_{ij} can adopt:

$$E_{ij} = E_{\mathrm{D}} + 0.5\,(E_j - E_i), \tag{6.16}$$

where E_{D} is the diffusion barrier height for an isolated adatom and the $E_{j(i)}$ describes the interaction of atom j (i) with all the other atoms. In fact, ν_0 and E_{D} are calibrating the simulated time scales. Consequently, by modifying this parameters within reasonable limits, experimentally observed time scales must be reproduced. In particular, if experimentally observed time scales differ from numerically simulated ones by a factor of more than 10^4 then it is no longer reasonable to compensate this discrepancy by an adjustment of ν_0 and E_{D} [247]. It is therefore a fundamental task to determine carefully these time scales from experimentally measurements, or *ab initio* calculations in order to obtain physical relevant time scales within the KMC approach.

The above presented KMC procedure in its simplest implementation would require $O(M)$ operations in each KMC step corresponding to M escape pathways. In particular, the physical time scale that can be reached within the KMC approach is strongly system dependent. To get an idea of which time scales are possible, we assume that present-day computers can reach 10^{10} steps in several hours. Furthermore, with a typically attempt frequency of the order of $10^{13}\,\mathrm{s}^{-1}$ a simulation time of $10^{13}/(10^{12}\exp(-E/\mathrm{k_B}T))\,\mathrm{s}$ can be achieved [161]. This gives for $E = 0.1\,\mathrm{eV}$ a total time of 50 ms at 300K and 3 ms at 1000K. In fact, these times are significant longer then times which can be reached with molecular dynamics. Nevertheless, it is useful to reduce the computation time in order to study the growth process of Cesium on Ag(111).

This can be done with the nearest-neighbor model, which assumes that only a small number of local configuration affects a given escape rate [169]. Furthermore, for a system in which there are equivalent rates that can be grouped in partial sums, the computation time becomes independent of M. [170]

Another restriction occurs in the case of a single low energy barrier. Since fastest hopping events slow-down the whole simulation, the total accessible physical time is significantly decreased. In order to overcome this limitation the fastest hopping events have to be avoided.

6.2. Second moment Tight-binding model

The study of adatom diffusion on crystal surfaces involve the knowledge of diffusion barriers. As above-mentioned, the KMC approach gives the exact dynamical evolution of a system, if the escape rate for exit from a current state i is exactly known. From the theoretical point of view total energy calculations using density functional theory (DFT) can be used to calculate such energy barriers. But, DFT is computationally expensive, which often limits the systems to small supercells. The tight-binding method (TB) can overcome this limitation and can give an acceptable information of band structures of most transition metals.

In the following section a tight-binding scheme is presented which allows to study the initial growth of atomic clusters on crystal surfaces, as it will be used in Chap. 7 to understand the growth process of small Cobalt clusters on Au(110). The numerical implementations

which were developed for this are shortly described. In particular, the use of canonical MC to find the ground state of the system instead of molecular dynamic simulation is discussed. To this end, the diffusion mechanism of a Gold atom onto the reconstructed Au(110) surface is investigated.

6.2.1. Tight-Binding Method

The tight-binding method assumes that around every lattice site of a crystal the total Hamiltonian can be characterized by the one-particle Hamiltonian of the individual lattice site. In particular, this requires that the eigenstates of the effective one-particle Hamiltonian can be expanded into an atomic-like basis set, where the exact many-body Hamiltonian is replaced by parametrized Hamiltonian matrix elements

$$h_{\alpha\beta}(\mathbf{k}) = \sum_j \mathrm{e}^{i\,\mathbf{k}\,\mathbf{R}_j}\; h_{\alpha\beta}(\mathbf{R}_j). \tag{6.17}$$

Here Bloch sums are used in order to construct periodic functions from the atomic function, which are parametrized the atomic orbitals. The key idea in the tight-binding formalism is to replace $h_{\alpha\beta}(\mathbf{R}_j)$ by parametrized functions depending on the interatomic distances $\mathbf{R}$. [171] The band energies $\epsilon(\mathbf{k})$ can then be evaluated as eigenvalues of

$$h(\mathbf{k})\;\chi_{\mathbf{k}}(\mathbf{r}) = S(\mathbf{k})\epsilon(\mathbf{k})\;\chi_{\mathbf{k}}(\mathbf{r}) \tag{6.18}$$

where $\chi_{\mathbf{k}}(\mathbf{r})$ are the eigenfunctions of the one-particle Hamiltonian, and $S(\mathbf{k})$ the overlap matrix. In particular, if one assumes that the atomic orbitals are already orthogonalized, the eigenenergies are just obtained from the diagonalization of the Hamiltonian matrix $h(\mathbf{k})$.

In order to study the formation of crystal structures the total energies rather than just band energies must be obtained. This usually requires an additional repulsive term which leads to

$$E_{\mathrm{tot}} = \underbrace{\sum_k \epsilon(\mathbf{k})}_{E^{\mathrm{B}}} + \underbrace{\sum_{ij} V_{ij}}_{E^{\mathrm{R}}}\,. \tag{6.19}$$

Therefore, the energy of an atom at site i can be written as the sum of two terms, an attractive band energy E_i^{B} and a repulsive pair interaction E_i^{R}.

The energy terms can be obtained using the second-moment approximation, where the realistic density of states (DOS) is replaced by schematic rectangular ones with the same second orbital moment. [172, 173] In detail, the description of the DOS in terms of its moments allows directly to relate the lattice topology to the electronic structure. In particular, the first moment is related to the band center and can be set zero, since its only fixes the energy scale. The square root of the second moment is roughly proportional to the average of the electronic DOS (the same full width at half maximum). [174]

Following Tomànek et al. [173] an analytical many-body potential scheme can be evaluated, wherein the band term can be written as

$$E_i^{\mathrm{B}} = -\sqrt{\sum_{j,r_{ij}<r_c} \xi_{AB}^2 \exp\left[-2q_{AB}\left(\frac{r_{ij}}{r_0^{AB}} - 1\right)\right]}, \tag{6.20}$$

where the exponent q_{AB} characterizes the distance dependence of the hopping integral between two atoms at sites i and j. While ξ_{AB} is an effective hopping integral and A, B

indicate the metal species. The nearest-neighbor distance in metal A is given by r_0^A and is assumed to be $r_0^{AB} = 1/2\,(r_0^A + r_0^B)$ in alloys. Where finally beyond a cutoff radius r_c the interaction is canceled. The repulsive term E_i^{R} is described by a sum of Born-Mayer ion-ion repulsions originating from the increase in the kinetic energy of conductance electrons constrained within two approaching ions:

$$E_i^{\mathrm{R}} = \sum_{j, r_{ij} < r_c} A_{AB} \exp\left[-p_{AB}\left(\frac{r_{ij}}{r_0^{AB}} - 1\right)\right], \tag{6.21}$$

where p_{AB} is related to the bulk modulus of the metal. In general, for each pure metal species the parameters ξ, A, p, q can be determined by fitting the potential to experimental values of the cohesive energy, lattice parameters, bulk modulus and elastic constants. [175]

6.2.2. Principles of calculations

By using the presented N-body potential scheme the energetics of adatoms, as well as clusters can be investigated. The key idea is to calculate the *cohesive* energy of the adsorbate onto the substrate, which is defined as follows:

$$E_{\mathrm{ads}} = E_{\mathrm{tot}}^{AB} - E_{\mathrm{tot}}^{A} - \mu^B, \tag{6.22}$$

where E_{tot}^{AB} is the total energy of the system including the substrate (A) with the adsorbate (B), and E_{tot}^{A} is the energy of the bare substrate. Moreover, μ^B is the chemical potential of the adsorbate B in the vapor phase, always taken as the origin of energies. The lateral change in the adsorption position on the underlaying substrate lattice provides then an estimation of the diffusion barrier.

In a first step of our theoretical investigation the substrate lattice is modeled as a finite slab of n atomic layers, where periodic boundary conditions are applied in the surface plane (x and y directions). The cohesive energy of the adsorbate is then calculated by using Eq. (6.22) as a function of the substrate-adsorbate distance, where the adsorption height z_{ads} is given by the minimum of E_{ads}.

In order to allow the substrate lattice to relax in the presence of the adsorbate the equilibrium structure of the system is determined in a second step of our theoretical investigation. To this end the above-mentioned canonical MC algorithm is used, which is able to find the global minimum of an arbitrary function. At this point typically quenched-molecular-dynamics or gradient descent method are used as energy minimization procedure. However, also canonical MC can be used at this point, as it will be demonstrated above.

In order to speed up the computation $(n-m)$ atomic layers are kept fixed, where $n > m$ and n, m are determined in this way that the MC code reaches the thermal equilibrium. Since we are basically interested in static diffusion barriers, the ground state of the system has to be determined. To this end we considered that the ground state of the system is reached, when the system temperature is lower than 1K (in the limit of $k_{\mathrm{B}}T \ll E_{ij}$), which ensures an energy accuracy better than 0.1 meV.

6.2.3. First results: Au on Au(110)

In order to give a proof of the capabilities of the developed TB-SMA code, the energetics of Au adatoms onto the reconstructed (110) facet of Gold is investigated. The reasons

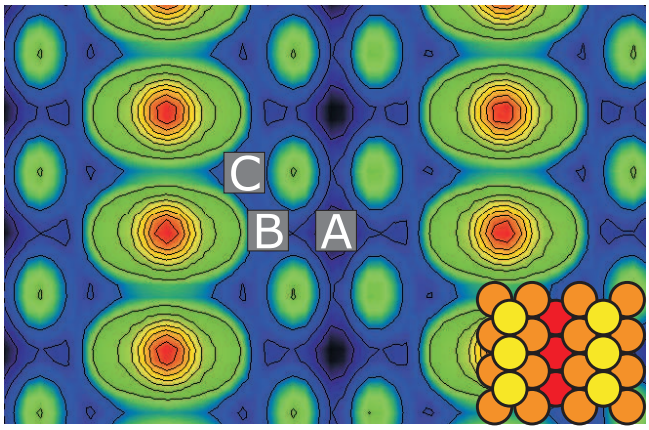

Figure 6.3.: Contour map of the potential energy surface of an Au adatom onto the reconstructed Au(110) surface. For the calculation only the adatom substrate-adsorbate distance was allowed to alter. Inset: Schematic drawing of the first three substrate layers. Possible adsorption sites of an Au adatom onto Au(110) are labeled A, B, and C.

to choose this system are twofold: First, this system was already studied by Montalenti and Ferrando [176] using molecular-dynamics simulations based on the above-mentioned many-body potentials, which allows us to verify our results. Secondly, the Au(110) surface was used in this thesis as a template to guide Cobalt deposition [see Chapter 7].

For this purpose the above-mentioned many-body potentials are used, where the parameters $\xi = 1.790\,\text{eV}$, $A = 0.2061\,\text{eV}$, $p = 10.229$, and $q = 4.036$ are taken from Ref. [175]. The simulations are performed with a slab of 12 layers, where the 5 bottom layers are kept fixed.

In a first step we are interested in the possible adsorption sites of an Au adatom onto Au(110). To this end the potential energy surface is calculated, where only the adatom substrate-adsorbate distance was allowed to change in order to reach the accurate adsorption height on the various lateral positions. A contour map of the resulting energy surface is shown in Fig. 6.3, where in the inset of Fig. 6.3 a schematic drawing of the first three substrate layers is presented. In agreement with Ref. [176], the lowest energy position (adsorption site) is found to be inside the the missing row (labeled A in Fig. 6.3). Another two local minima are at the (111) facet, which are labeled B and C, respectively. Moreover, two saddle-points are found, which have to be crossed by an Au adatom adsorbed on the energy position A.

In the next step of our theoretical investigation we are interested in the diffusion barriers. Therefore, the adsorbate energy is calculated along the pathways AA and AB, where at each point along the pathway the x and y coordinates of the adatom are fixed and all other degrees of freedom of the system are allowed to relax. The following static energy barriers are found: $E_{A\to A} = 0.28$ eV for a single jump along the missing row, $E_{A\to B} = 0.39$ eV for translations from in-channel minima to the meta-stable B sites, and $E_{B\to A} = 0.06$ eV for the reverse move. These values are in good agreement with $E_{A\to A} = 0.31$ eV, $E_{A\to B} = 0.40$ eV, and $E_{B\to A} = 0.06$ eV calculated by Montalenti and Ferrando [176], which use molecular dynamics as an energy minimization procedure.

Summing up, the use of the above presented tight-binding potentials to describe binding energies of adatoms and small clusters, combined with the use of canonical MC as an

energy minimization procedure gives an idea about the relevant diffusion processes. In Chap. 7 this method is used to study the growth of Co on Au(110) in the early stages of heteroepitaxy.

Chapter 7.

Template-guided formation of cobalt clusters on Au(110)

The ongoing miniaturization of magnetic memory devices is be linked to the challenge of shifting the superparamagnetic limit. At this limit the magnetization of magnetic grains used to store one bit reverses due to thermal excitation on a time scale shorter than the desired memory retention time. Consequently, it is of considerable interest to decrease the size of magnetic grains and explore the ultimate value of the superparamagnetic limit. The minimum size and the optimum shape of assemblies of magnetic atoms with constant magnetization is of considerable interest and these assemblies must be fabricated.

To this end two experimental paths, as reviewed by Martín *et al.* [177], can be taken, namely (i) top-down and (ii) bottom-up fabrication methods. The top-down approach has been the traditional method to miniaturization by sculpting via lithographic tools. However, structure sizes below several tens of nanometers are challenging for lithography. This is where bottom-up methods enter centrestage. To create assemblies of magnetic atoms with a given shape two fabrication methods may be applied. Tip-assisted manipulation of individual atoms, as first reported by Eigler and Schweizer [178], is suitable to form single nanometre-scaled arrays with an artificial shape. If parallel fabrication of many similarly shaped assemblies with a high degree of lateral periodicity is desired, the use of pre-structured surfaces appears to be an appropriate choice. For instance, vicinal surfaces have been proved as templates to guide deposition of atoms [179–181] and molecules [182–185]. Reconstructed surfaces may also be used. For instance, gold is the only face-centered cubic metal where the close-packed (111) surface has been observed to reconstruct. Measurements by helium atom scattering [186] and scanning tunneling microscopy (STM) [187,188] reported on the $22 \times \sqrt{3}$ reconstruction which is also referred to as the herringbone reconstruction. Initial nucleation of cobalt deposited on Au(111) at room temperature as investigated by STM [189,190] takes place at the so-called elbow sites of the herringbone reconstruction. This nucleation behavior gives rise to a regular array of Co islands on Au(111). The (110) surface orientation of face-centered cubic transition metal crystals has a strong tendency for reconstructions of the missing row type [191]. In a previous study Au(110) was employed for Ni deposition [192]. As a main result, Hugenschmidt *et al.* [192] reported that Ni adsorption on Au(110) was morphologically dominated by the presence of the missing row reconstruction. Upon deposition at lower temperatures, one-dimensional Ni chains were located in the troughs of the reconstruction, while at higher temperatures ($\approx 220\,\mathrm{K}$) so-called double rows were found which above 280 K coalesce into two-dimensional islands.

The aim of this chapter is to give a detailed understanding of the growth process of small atomic colbalt (Co) clusters on a pre-structured surface. To this end the adsorbate system Au(110)-Co in stages of growth is studied. While at 80 K Co adsorbs in compact clusters of two to four atoms inside the missing gold row [Sec. 7.2], at room temperature Co chains

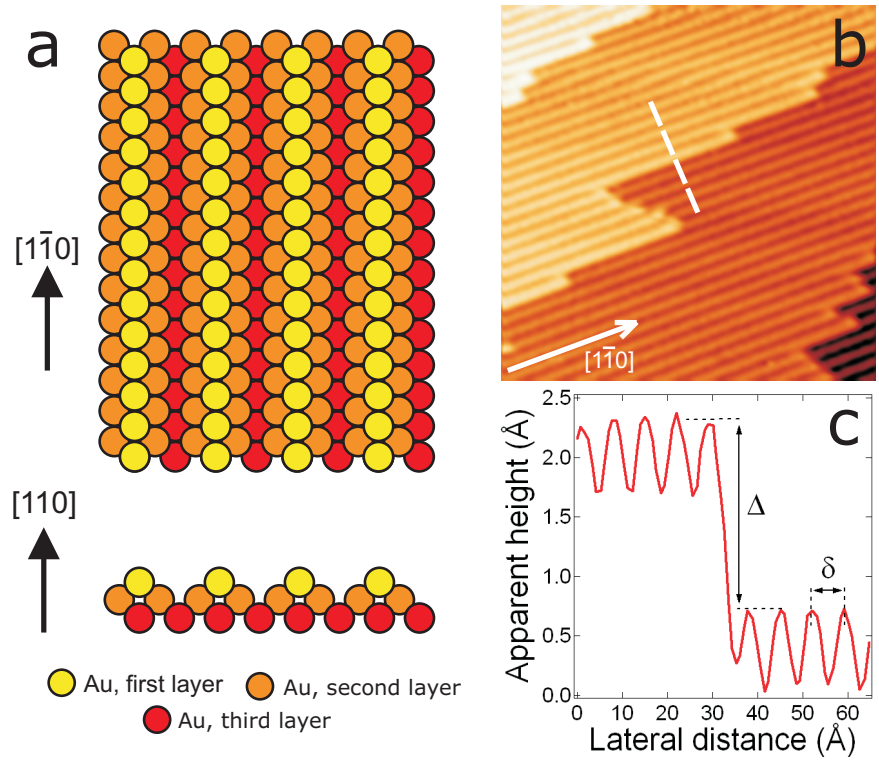

Figure 7.1.: (a) A schematic drawing of the Au(110) surface. (b) STM image of clean Au(110) acquired at room temperature ($V = -190\,\mathrm{mV}$, $I = 0.7\,\mathrm{nA}$, $200\,\text{Å} \times 200\,\text{Å}$). Crystallographic orientation of the missing row is indicated. (c) Cross-sectional profile along the path indicated by a dashed line in (b). For the step height we obtain $\Delta = 1.5\,\text{Å}$ and for the distance between the ridges of the surface reconstruction $\delta = 8.0\,\text{Å}$.

with different width end length are oriented along the missing row direction [Sec. 7.3]. The experimentally obtained results are confirmed with atomic-scale simulations revealing the energetics of various diffusion processes.

7.1. The Au(110) surface

The crystal structure of Gold is face-centered cubic (fcc) with a lattice constant of 0.408 nm. This represents a nearest neighbor distance of 0.288 nm. The ideal (110)-surface would keep a squared elementary cell with a lattice constant of 0.288 nm along [1$\bar{1}$0] and 0.408 nm along the perpendicular direction. But, due to the inward relaxation of the surface layer the clean Au(110) surfaces form a (1×2) reconstruction at room temperature [191]. In particular, alternate atomic rows in the [1$\bar{1}$0] direction are removed exposing (111) micro-facets, which leads to a distance of 0.816 nm between two adjacent gold rows. In Fig. 7.1(a) a sphere model of the reconstructed Au(110) surface is shown, where the different colors represent the 1st, 2nd and the 3rd layer as indicated in the figure.

In Fig. 7.1(b) we present an STM image of clean Au(110). The (1×2) missing row reconstruction can be identified by ridges (bright contrast) and troughs (dim contrast) which are oriented along [1$\bar{1}$0] as indicated in the STM image. Figure 7.1(c) shows a cross-sectional profile taken perpendicular to [1$\bar{1}$0] (see dashed line in Fig. 5.5). The distance

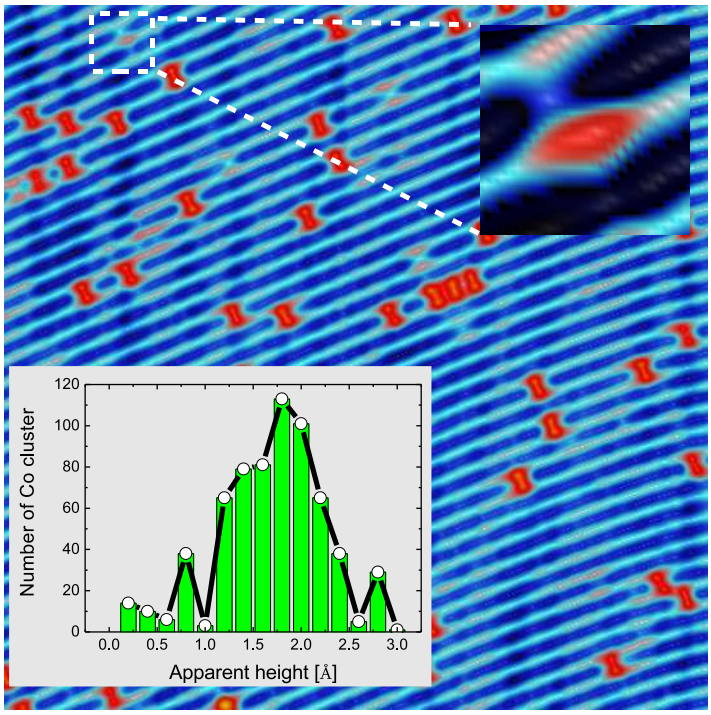

Figure 7.2.: Low-temperature STM image of 0.14 ML of Co adsorbed on Au(110) at 78 K ($V = 200\,\mathrm{mV}$, $I = 0.1\,\mathrm{nA}$, $250\,\text{Å} \times 250\,\text{Å}$). Close-up view of a Co atom embedded into the topmost gold layer. Inset: Histogram of the apparent height of Co assemblies.

between the ridges is $\delta = (8.0 \pm 0.5)\,\text{Å}$ while the step height is $\Delta = (1.5 \pm 0.1)\,\text{Å}$ in good agreement with previous measurements [194].

7.2. Deposition at low temperature

To study the growth of Co on Au(110) in the early stage of the growth process we focus in this section to low temperatures. Our investigation involves two steps: Firstly, our experimental results are presented and the cluster sizes are analyzed with the help of cross-sectional profiles. Secondly, the in Sec. 6.2 presented tight-binding scheme is used to ascertain the energies of Co atoms and clusters on Au(110).

7.2.1. Experimental results

For Co deposition at 78 K the clean Au(110) sample was transferred to the scanning tunneling microscope and deposition was performed onto the cooled sample through openings in the shields of the cryostat. Deposition rates as judged from the exposure time and from STM images of Co-covered surfaces were estimated to be $\approx 0.2\,\mathrm{ML\,min^{-1}}$. One monolayer (ML) is defined in the following as one Co atom per Au atom. All STM images presented in this chapter were acquired in constant-current mode. Voltages refer to the sample bias with respect to the tip.

Figure 7.2 displays a representative STM image of Au(110) covered with 0.14 ML of Cobalt. The (1×2) missing row reconstruction can be identified by ridges (bright contrast)

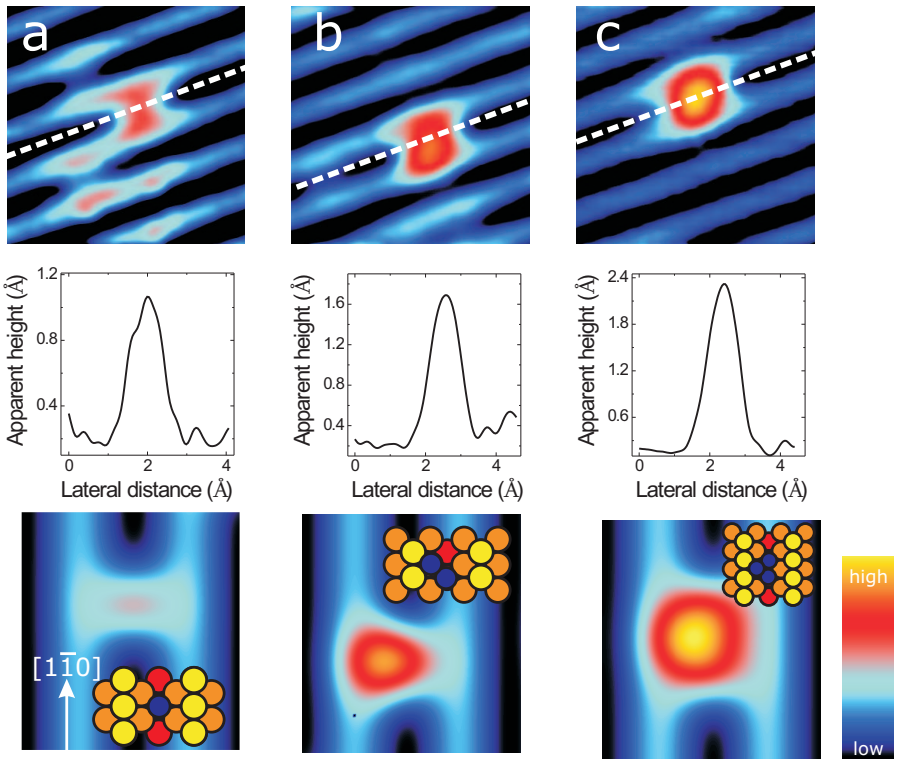

Figure 7.3.: STM images of the typical observed Co assemblies ($V = 130\,\mathrm{mV}$, $I = 1\,\mathrm{nA}$, $40\,\text{Å} \times 40\,\text{Å}$) together with their cross-sectional profiles and modeled STM images of the proposed adsorption geometries. For this reason, a two dimensional Gaussian is used to model a single Co atom (a), a superposition of two such Gaussians are used for the dimer (b), and three Gaussians are used to describe a trimer (b). The substrate itself is modeled by a sinusdoidal function. Color scale: the apparent heights range from 0 (low) to 2.4 Å (high).

and troughs (dim contrast) which are oriented along [1$\bar{1}$0]. Different types of Co assemblies are observed. While the most common Co assemblies are adsorbed in the troughs of the surface reconstruction, assemblies adsorbed on top of the ridges –close-up view in Fig. 7.2– were observed less frequently.

In order to analyze their size distribution in detail the apparent height of 650 Co assemblies is determined from constant-current STM images, which were acquired at different samples and surface areas. To reduce effects of tip shape and voltage on the apparent height of the clusters, all STM images were normalized in this way that the apparent height of the (1×2) missing row reconstruction appears identical for all images. Within this normalization procedure the histogram presented in the inset of Fig. 7.2 was acquired. As a result, a prominent peak at 1.8 Å appears in the histogram with a shoulder at 1.6 Å to its left side, and two small peaks at 0.8 Å an 2.8 Å, respectively. In particular, only the apparent height of the clusters are analyzed, since a detail analysis of the widths of the clusters along [001] is hampered by the missing row reconstruction of the substrate, where along [1$\bar{1}$0] the differences in the widths of the Co assemblies are found to changing not significant and a full width at half maximum (FWHM) of $\approx (8.0 \pm 0.5)$ Å is obtained.

To determine the number of Co atoms inside the Co assemblies a sphere model is pre-

sented in the following, which is based on cross-sectional profiles of the observed assemblies. To this end three representative Cobalt species are analyzed by cross-sectional profiles along $[1\bar{1}0]$ in the middle panel of Fig. 7.3. The experimental profiles shown in Fig. 7.3 are fitted by a Gaussian lineshape giving apparent heights of $\approx (0.9 \pm 0.1)$ Å for assembly shown in Fig. 7.3(a), $\approx (1.4 \pm 0.1)$ Å for the cluster of Fig. 7.3(b), and $\approx (2.1 \pm 0.1)$ Å for the assembly depicted in Fig. 7.3(c). In comparison with the apparent height of a single Co atom adsorbed at 7K (not shown) we can conclude that the species presented in Fig. 7.3(a) corresponds to an individual Co atom. In order to get an idea about the adsorption geometry of these Co assemblies the extracted apparent height and FWHM are used to draw the shape of the clusters as the appear in STM images. For this reason, a two dimensional Gaussian is used to model single Co atoms and a sinusoidal function is taken to describe the reconstructed substrate surface. By using superpositions of two and three of such Gaussians and taking the mutual distance between gold atoms into account Co dimers, and trimers can be constructed. The results are presented in the bottom panel of Fig. 7.3, together with a schematic drawing of the adsorption geometry. Since the apparent height of these Co clusters, and their spatial appearance in the contour plot are in agreement with the experimental data, we propose dimers and trimers as reasonable cluster shapes for the most frequently observed assemblies.

While the above Co structures grow starting from missing rows, another type of structure is embedded in existing Au rows. A typical example of these structures along $[1\bar{1}0]$ is shown in the inset of Fig. 7.2. While its FWHM is ≈ 3.5 Å, its apparent height is ≈ 0.5 Å. Based on these data and on the comparison with the dimensions of the other Co clusters we propose that single Co atoms are embedded into the topmost Au rows by atom exchange during the Co deposition at 78 K.

Observation of intermixing of adsorbed atoms (adatoms) and substrate atoms was reported for Au(110)-Ni [192] and the closely related system Ni(110)-Au [197]. In Ref. [192], the exchange of adatoms and substrate atoms was evidenced by locations on substrate terraces as well as on adsorbate islands which appeared lower than the majority of atoms. These sites were attributed to substitutional nickel atoms incorporated into the topmost gold rows. In Ref. [192] atomic exchange was suggested to be assisted by the presence of adjacent Ni islands. This conclusion was drawn because of an asymmetry in the distribution of Ni atoms incorporated in the top Au rows on either side of adsorbed Ni islands along $[1\bar{1}0]$. A theoretical study by Stepanyuk and Hergert [198] revealed that site exchange between $3d$ transition metal impurities on Au(100) and Au atoms are energetically favorable. However these investigations have been carried out at room temperature. In direct contrast, at 78 K, an intermixing of adsorbed atoms can be assumed to be strongly suppressed. Indeed, the number of Co atoms embedded into the topmost substrate layer are found to be only $\approx 10\%$, which implies that this process is less efficient at 78 K. However, detailed information about the diffusion processes of Co on Au(110) is essential to understand the growth mechanism of Co on Au(110). To this end, the energetics of various diffusion processes will be adressed in the following by using atomic-scale simulations.

7.2.2. Theoretical results

To model diffusion processes at the atomic scale, the second moment tight-binding method (presented in Sec. 6.2) is used. This method allows one to construct many-body potentials to describe the interatomic interactions of different species of atoms involved in the system and to investigate at the same time large systems in fully relaxed geometries [174, 175].

	A_1 (eV)	A_{AB} (eV)	ξ_{AB} (eV)	p_{AB}	q_{AB}	r_0^{AB} (nm)
Au-Au		0.1890	1.7440	10.4000	3.8700	0.2880
Au-Co		0.1400	1.6560	10.6300	3.1100	0.2695
Co-Co	-0.8520	0.1390	1.5200	7.6790	2.1390	0.2378

Table 7.1.: Parameters used in the calculation of interatomic interactions, where p_{AB} and q_{AB} characterize the decay of the interaction strength with distance of the atoms, ξ_{AB} is an effective hopping integral, and r_0^{AB} is nearest-neighbor distance. While the values for Au-Au and Au-Co are taken from Ref. [199], for the Co-Co interaction potential a modified form of the repulsive part is used introduced in Ref. [200].

As discussed in Sec. 6.2 the total energy of the system E_{tot} can be written as a sum of two terms:

$$E_{\text{tot}} = \sum_i (E_i^{\text{B}} + E_i^{\text{R}}), \tag{7.1}$$

where the attractive term (band term) E_i^{B} contains the many-body interaction

$$E_i^{\text{B}} = -\sqrt{\sum_{j,r_{ij}<r_c} \xi_{AB}^2 \exp\left[-2q_{AB}\left(\frac{r_{ij}}{r_0^{AB}} - 1\right)\right]}, \tag{7.2}$$

and the repulsive term E_i^{R} is described by pair interactions

$$E_i^{\text{R}} = \sum_{j,r_{ij}<r_c} A_{AB} \exp\left[-p_{AB}\left(\frac{r_{ij}}{r_0^{AB}} - 1\right)\right]. \tag{7.3}$$

The parameters ξ, A, p, q can be determined by fitting the potential to experimental values of the cohesive energy, lattice parameters, bulk modulus and elastic constants. [175] In detail, A, B indicate the metal species, p_{AB} and q_{AB} characterize the decay of the interaction strength with distance of the atoms, ξ_{AB} is an effective hopping integral, and r_0^{AB} is nearest-neighbor distance. Finally, the interaction is canceled beyond a cutoff radius r_c. The parameters used for the potentials are summarized in Tab. 7.1.

The substrate lattice relaxation in presence of adsorbate atoms has been investigated by using the canonical Monte Carlo method, as described in Sec. 6.2. Since we are basically interested in the ground state configuration of the system, the system temperature in the calculation is taken lower than 1K. Calculation of diffusion barriers are carried by means of adsorption energy calculation of individual Co atoms, as well as small clusters. Therefore a finite slab of 12 layers is constructed, where the five bottom layers are kept fixed and periodic boundary conditions are applied in the surface plan.

The obtained results for a single Co atom are presented in Fig 7.4. In accordance with the results of Sec. 6.2 we consider three possible adsorption sites for an individual Co atom on the Au(110) surface. Firstly, the adatom can be adsorbed in the troughs of the surface reconstruction (missing gold row), secondly on the metastable (111) facet of the missing gold row coordinated by two second layer and one third layer Au atoms, and thirdly on the same facet but now coordinated by one second layer and two first layer Au atoms. We are particularly interested in activation energies, which have to be reached to change their adsorption sites. In particular, the diffusion barrier E_1 of an individual Co atom

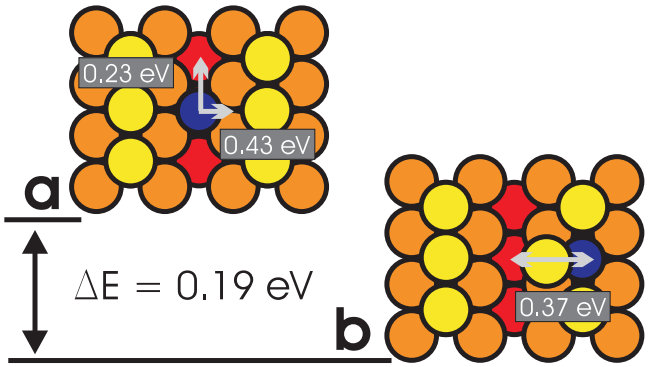

Figure 7.4.: Energetics of an individual Co atom at the proposed adsorption geometries. (a) A Co atom (blue circle) is adsorbed on the surface. (b) If an atom is embedded in the first substrate layer the total energy of the system has been found to decrease. The activation barriers of the atomic events are presented in the gray frames.

along $[1\bar{1}0]$ is found to be 0.23 eV, where the activation energy E_2 to reach a adsorption site on the (111) facet is 0.43 eV, as presented in Fig 7.4(a). While at room temperature a Co atom can easily overcome these barriers, at 80K diffusion on the (111) facet is strongly suppressed. Indeed, a single diffusion process needs approximately at time τ of $\nu_0^{-1}\exp(E_i/k_\mathrm{B}T)$ according to the Arrhenius behavior. Assuming an attempt frequency ν_0 of $1 \times 10^{13}\,\mathrm{s}^{-1}$ and for E_i the obtained diffusion barriers E_1 and E_2 one finds that at room temperature diffusion occurs within less then microseconds in both directions. In contrast, at 80K the time scale reaches order of seconds to several hours for jumps on the (111) facet of the missing gold row. We therefore conclude that movements from troughs of the missing row to their facet are suppressed at 80K.

However, single Co atoms, which are embedded into the topmost Au rows by atomic exchange, decrease the total energy of the system by $\Delta E = 0.19\,\mathrm{eV}$, as depicted in Fig 7.4. This process takes place with a barrier E_3 of 0.37 eV. In agreement with the above-mentioned approximation this process is very unlikely to be observed at 80K. In order to understand this discrepancy it has to be kept in mind that Co atoms are deposited onto the substrate using e-beam evaporation, which provides additional kinetic energy to the atoms. In fact, for Ir atoms on Rh(100) atomic exchange was observed at temperatures well below those required for thermal exchange [203]. Based on this experimental observation we suggest that arriving Co atoms can transfer some of their kinetic energy into motion along the surface. Since embedded atoms were less frequently observed in the experiment, we conclude that this transfer process is less efficient at low temperatures.

To study the initial growth of the experimental observed small Co clusters the total energy of different adsorption geometries are investigated and the obtained results are summarized in Fig 7.5. As a result, the most stable configuration of two Co atoms is a dimer, where the two most possible configurations on Au(110) are presented in Fig 7.5(a). While in the first configuration both dimer atoms are adsorbed along the troughs oriented along $[1\bar{1}0]$, the total energy of the system can be decreased by $\Delta E = 0.11\,\mathrm{eV}$, if one Co atom moves on the (111) facet. This motion takes place with a diffusion barrier of 0.28 eV. Since this activation energy is not much different from the barrier E_1 along the missing row we propose this dimer configuration as most probable. Moreover, this configuration leads to an asymmetric form of the cluster, similar to our experimental findings [see

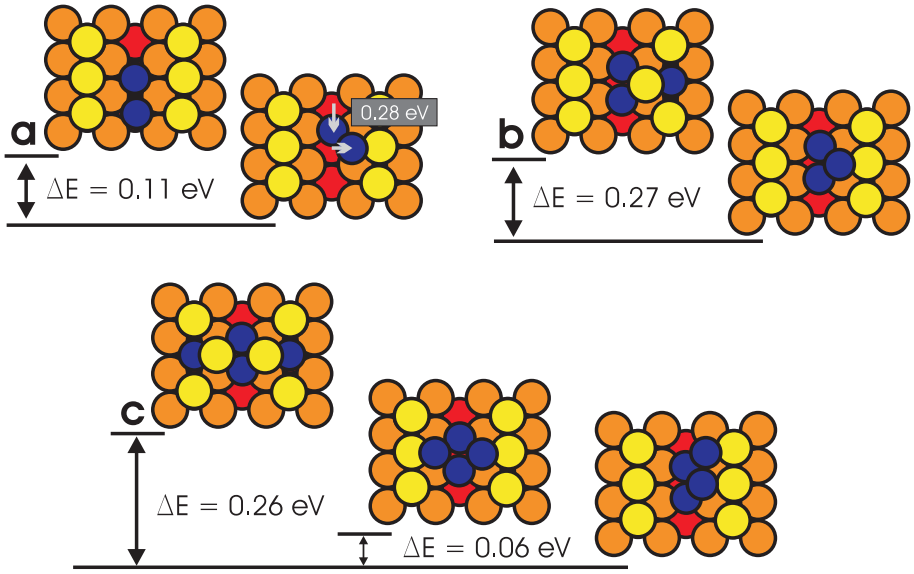

Figure 7.5.: Inertial stages of low temperature Co growth on Au(110). Possible adsorption geometries for (a) two, (b) three, (c) four Co atoms are illustrated, where the most stable configuration are shown in each panel at the bottom and the relative energies between the adsorption geometries are indicated by arrows.

Fig 7.3(b)]. If a third Co atom is taken into account the trimer is found to be the most stable configuration, where a configuration of two Co atoms along the missing row and the third atom on the facet is found to be energetically favorable [see Fig 7.5(b)]. Moreover, the atom exchange of a Co atom with one Au atom of the topmost Au row increases the total energy of the system by $\Delta E = 0.27\,\text{eV}$. Therefore, such an atom exchange process can be assumed to be suppressed.

Finally, four Co atoms are most probable adsorbed into a tetramer, with two Co atoms into troughs of the missing row and two onto the (111) facet oriented along $[1\bar{1}0]$, as shown in Fig 7.5(c). Since the difference in the total energy between the two possible configurations, as depicted in Fig 7.5(c), are very small both of them are probable configurations of Co tetramers on Au(110). However, to distinguish between these two configurations from STM images is challenging due to their small spatial differences. Similar to the trimer configuration, we found that an atom exchange, as shown in Fig 7.5(c), increases the total energy of the system by $\Delta E = 0.26\,\text{eV}$. In agreement with our experimental findings we conclude therefore that Co dimers and trimers are the most frequently observed assemblies in the initial stage of Co growth on Au(110) at 78K.

7.3. Deposition at room temperature

Figure 7.6 displays a STM image of Au(110) covered with 0.05 ML of Co grown at room temperature. Along $[1\bar{1}0]$ elongated adsorbate assemblies are observed. Three types of assemblies occur most frequently on the surface. Types 1 and 2 exhibit a uniform width along their entire length, while type 3 changes its width somewhere along the chain. In Figs. 7.7(a)-(c) we analyse the geometric structure of these Co assemblies in more detail. A chainlike assembly is presented in the top panel of Fig. 7.6(a). The width of the chain

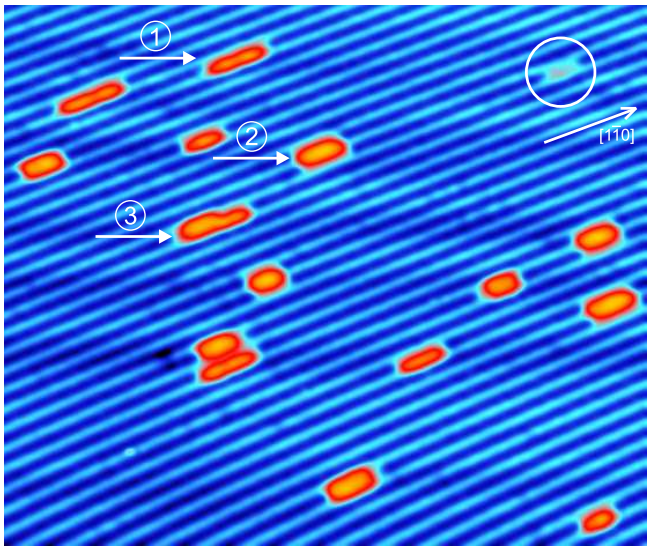

Figure 7.6.: Room temperature STM image of Co-covered Au(110) after deposition at room temperature ($V = 80\,\mathrm{mV}$, $I = 6\,\mathrm{pA}$, $310\,\text{Å} \times 260\,\text{Å}$). Three most frequently observed types of Co chains are indicated by arrows (1,2,3). The Co assembly encircled by a full line does not occur as frequently as the others.

is $\approx 8\,$Å (evaluated from the FWHM of the largest peak in the cross-sectional profile of Fig. 7.7(a)), while the apparent height is $\approx 2\,$Å (relative to the Au rows) at the given voltage. The lateral extension of the chain along the missing row is $\approx 40\,$Å which, judging from the mutual gold atom distance along [1$\bar{1}$0] of $\approx 2.9\,$Å, corresponds to two lines of 14 adjacent atoms. Structure 2 is analysed in Fig. 7.7(b). While its apparent height is $\approx 3\,$Å (relative to the Au rows), the FWHM of the chain perpendicular to the missing row direction as seen most clearly in the cross-sectional profile (middle panel of Fig. 7.7b) is $\approx 16\,$Å. Figure 7.7(c) shows a Co assembly (adsorption type 3) which does not reveal a uniform width along [1$\bar{1}$0]. While the narrow part of the chain corresponds to a two atom wide chain (see Fig. 7.7(a) and the lowest panel of Fig. 7.7c), the wider part ($\approx 15\,$Å) matches a width of three Co atoms (lower panel of Fig. 7.7c). Moreover, the apparent heights of the Co chains presented in Figs. 7.7(b) and 7.7(c) are similar.

Increasing the Co coverage at room temperature leads to two-dimensional and three-dimensional growth. In Fig. 7.8(a) we present a STM image of the Au(110) surface covered with 0.5 ML of Co. Widths and heights of the assemblies are quite different from the corresponding dimensions at low coverage. The increased width, *i. e.*, the extension of the chains perpendicular to [1$\bar{1}$0], can be explained by coalescence of adjacent chains. Additional Co atoms may also adsorb on top of the existing chains and increase their height as shown in Fig. 7.8(b). Apparently, the increase of coverage does not lead to a considerable increase of the chain length along [1$\bar{1}$0]. Rather, two-dimensional island growth across the ridges of the surface reconstructions by coalescence of adjacent chains sets in. At this coverage we also observed clusters with apparent heights of $\approx 14\,$Å indicating three-dimensional growth of the assemblies. Furthermore, the Au rows of the substrate seems to be partly destructed by the Co deposition as indicated by the arrows in Fig. 7.8(a), which additionally revealed the evidence of surface alloying.

In this context it is interesting to refer to experiments on Ag(110)-Pd and Ag(110)-

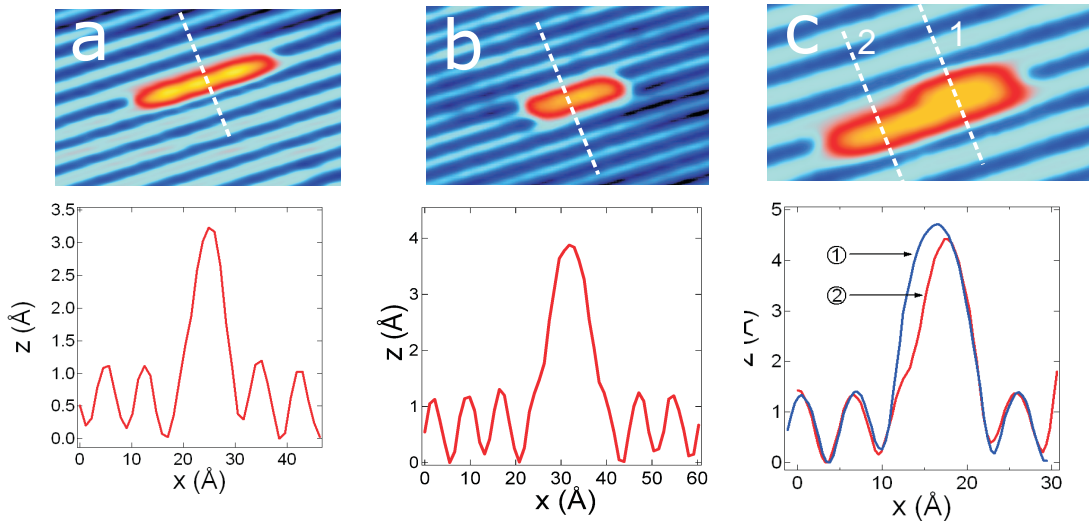

Figure 7.7.: (a) STM image of Co chain-like assembly ($V = 20\,\mathrm{mV}$, $I = 16\,\mathrm{pA}$, $92\,\text{Å} \times 58\,\text{Å}$) together with the cross-sectional profile. (b) STM image of a observed Co adatom assembly ($V = 20\,\mathrm{mV}$, $I = 16\,\mathrm{pA}$, $90\,\text{Å} \times 70\,\text{Å}$) and cross-sectional profile. (c) STM image of a Co chain where both (110) facets of the missing row are occupied ($V = 20\,\mathrm{mV}$, $I = 4\,\mathrm{pA}$, $45\,\text{Å} \times 32\,\text{Å}$).

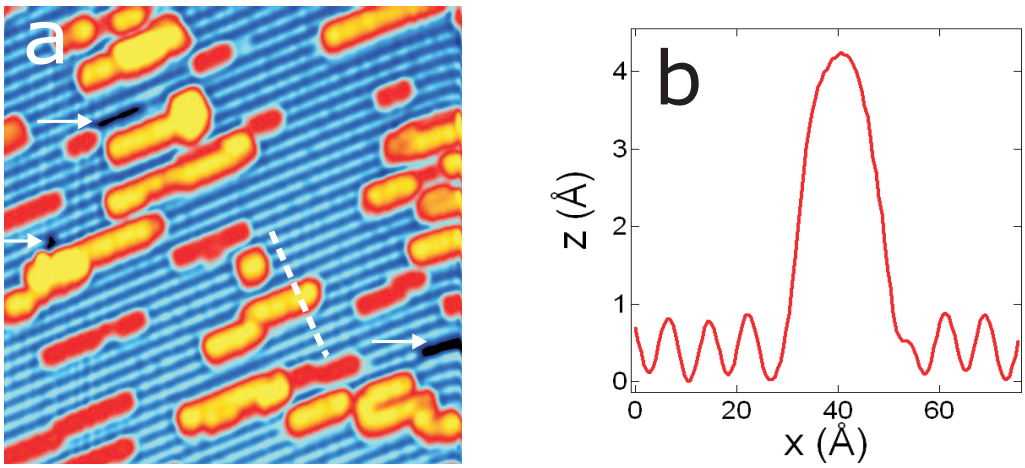

Figure 7.8.: (a) STM image of 0.5, ML of Co adsorbed on Au(110) ($V = 180\,\mathrm{mV}$, $I = 0.1\,\mathrm{nA}$, $200\,\text{Å} \times 200\,\text{Å}$). (b) Cross-sectional profile across the Co chain as indicated by the dashed line in (a).

Pt [195, 196]. While X-ray and ultraviolet photoemission hinted at the formation of linear chains or two-dimensional islands for both adsorbate systems at low coverages, calculations within the embedded atom model revealed the propensity of Pt to form three-dimensional clusters on Ag(110). By extending the model to allow for surface alloying and further experimental analysis Massobrio *et al.* [195] concluded that intermixing of adsorbate and substrate was more likely than three-dimensional growth. Moreover, from our theoretical analysis we know that the embedding of a single Co atom in the topmost substrate layer by atomic exchange reduces the total energy of the system by 0.19 eV. In a recently published theoretical investigation [201] on a similar system, namely Co/Cu(110), the intermixing of Co and Cu substrate atoms reveals that embedded Co atoms serve as nucleation centers for substituted Cu atoms, which leads to elongated clusters. However, it turned out from our investigation that the intermixing of Co and Au substrate atoms plays a minor role in the growth process of Co on Au(110). From our calculations as well as from our STM images of Co clusters grown at room temperature at low coverages no indication of surface alloying can be observed. As a reason for these findings the relatively low diffusion barrier along $[1\bar{1}0]$ can be assumed to lead to a channel diffusion. Moreover, small clusters of atoms are found to be energetically favorable as to alloy with substrate atoms [see Fig 7.5]. This findings are in contrast to the above-mentioned closely related systems Au(110)-Ni [192] and Ni(110)-Au [197].

7.4. Conclusion

Cobalt deposition at 78 K gives rise to compact Cobalt clusters of two up to four atoms. At room temperature deposition and at low Co coverages the adsorbate structure is dominated by the missing row reconstruction of Au(110) which therefore acts as a template for guiding Co deposition. Upon increasing the coverage two-dimensional growth of islands owing to coalescence of adjacent Co chains, as well as three-dimensional growth was revealed. The interchange behavior of Co and Au atoms within the reconstruction rows points to an initial stage of surface alloying. The experimentally obtained results are modeled with atomic-scale simulations revealing the energetics of various diffusion processes. This adsorbate system is a promising candidate to investigate size- and shape-dependent magnetic properties of atom assemblies at the nanometer scale.

Chapter 8.

Cesium on Ag(111)

The fabrication of ordered structures on surfaces at the atomic length scale is central to the understanding of geometric, electronic, and magnetic properties of single atoms or molecules in a solid state environment. In principle, a lot of fundamental aspects can be gained from *test systems*, which enable the study of interaction of adsorbates, with coadsorbates, and with the surface itself. Alkali atoms on noble metal surfaces are such *simple* systems. Indeed their adsorption on metal surfaces has been studied intensely for many years (for a review see Refs. [5, 204]). With their single s electron at the outermost atomic shell these metals are considered as simple and much research on the analysis of the interplay between their mutual interaction and the interaction with the hosting substrate has been done [204].

In this chapter the structural and electronic properties of the adsorbate system Ag(111)-Cs will be discussed. The creation of hexagonal ordered superlattices of single Cs adatoms on Ag(111) will be reported in Sec. 8.2. In particular, the interplay between surface-state mediated interaction and dipole-dipole repulsion will be discussed, where the observed adsorbate structures are modeled within kinetic Monte Carlo simulations. Besides these structural properties, alkali metal-covered surfaces exhibit intriguing electronic properties. In particular, the lifetimes of excitations of electronic states are central for the understanding of processes at surfaces, as discussed in Sec. 8.3. In detail, we found that individual Cs atoms adsorbed on Ag(111) induce a resonance appearing just below the threshold of the quasi-two-dimensional Shockley-type surface state continuum. Furthermore, *A. G. Borisov* and *J. P. Gauyacq* provided theoretical modeling of our experimental data, which identify the importance of various contributions to the linewidth and to the decay of this resonance. The starting point of this chapter [Sec.8.1] is a brief overview of alkalis on metal surfaces focusing mainly on the important aspects used for the understanding of the adsorbate system Ag(111)-Cs.

8.1. Basic aspects

The aim of this section is to summarize the basic structural and electronic aspects of alkali atoms adsorption on noble metal surfaces. But before going into detail about alkalis on metal surfaces the central properties of the used Ag(111) substrate surface are presented.

8.1.1. The Ag(111) surface

The crystal structure from silver is face-center-cubic (fcc) with a lattice parameter of 409 pm. As shown in the constant-current STM image presented in Fig.8.1, the hexagonal closed-packed (111) surface exhibits an interatomic distance of $409\,\mathrm{pm}/\sqrt{2} = 289\,\mathrm{pm}$ and a six-fold symmetry.

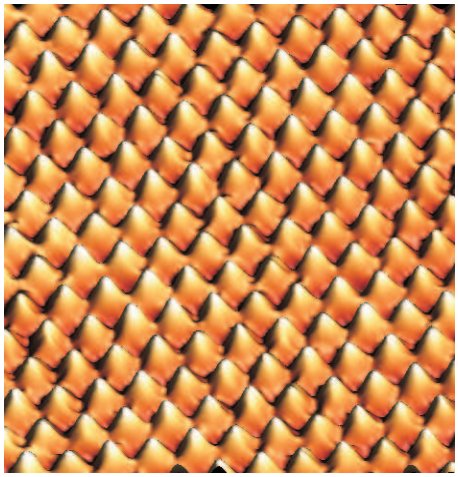

Figure 8.1.: Atomically resolved STM image of the clean Ag(111) surface (voltage $V = 100\,\mathrm{mV}$, current $I = 0.1\,\mathrm{nA}$, size $3\,\mathrm{nm} \times 3\,\mathrm{nm}$).

The electronic properties of the Ag(111) surface are mostly characterised by the *Shockley surface-state*. A Shockley surface-state appears in the surface-projected band gaps of bulk electronic structures and has its band edge at $E_0 = -63\,\mathrm{meV}$ below the Fermi energy. Following Ref. [254], the appearance of a surface state can be described by a model potential sketched in Fig. 8.2(a). At the surface ($z = 0$) the periodicity of the crystal potential [black line in Fig. 8.2(a)] is interrupted, which leads to the fact that physically not possible electron wave-functions [doted line in Fig. 8.2(a)] with imaginary k-vectors inside the crystal have a non vanishing real part at the surface. As a result, the amplitude of the surface-state wave-function decreases exponentially in the crystal as well as in the vacuum. Moreover, the Ag(111) surface state electrons form a nearly free two-dimensional electron gas with an almost parabolic dispersion relation and an electron mass of $\mathrm{m}^* = 0.42\,\mathrm{m}_0$, which is usually different from the free electron mass m_0.

As seen in Chapter 2 scanning tunneling spectroscopy (STS) enables monitoring of the differential conductance (dI/dV), which can be related to the local density of states (LDOS) of the sample. A typical dI/dV spectrum acquired over a bare terrace of Ag(111) is presented in Fig. 8.2(b). A sharp steplike onset at an energy $E_0 = -67\,\mathrm{meV}$ can be observed, which corresponds to the lower edge of the Ag(111) surface-state band.

8.1.2. Alkali on noble metal surfaces

The most striking effect of alkali metal adsorption on noble metal surfaces is the drastic change in the surface work function. At low coverages, the work function decreases strongly with an increasing alkali coverage and increases again after reaching a minimum at half the saturation coverage, which is given by the maximum amount of adsorbate atoms that build an adlattice on the substrate surface. Following R. W. Gurney [291] this effect can be explained, since the alkali ionisation energy is smaller than the clean surface work function. Therefore the first alkali adatoms adsorb as positive ions on the surface, which leads to a dipole layer on the surface. At elevated coverages the adatoms progressively neutralise, which leads to a saturation of the work function and finally for high coverages to a metallic layer.

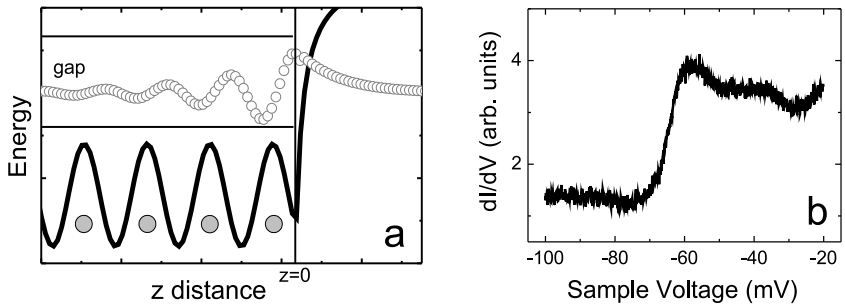

Figure 8.2.: (a) Localization of the surface state: Crystal potential (black line) oscillates in the bulk and decays at the surface into the vacuum. Since the surface states wavefunction (dotted gray line) decreases exponentially in the bulk and in the vacuum, a state is localized at the surface. (b) STS enables to measure the surface state: dI/dV spectrum over the center of a defect- and impurity-free area of Ag(111) (feedback loop opened at 1 nA and 100 mV).

Structural studies of alkali adsorbate superstructures focused mostly on higher coverages. For Ag(111)-Cs, a $p(2 \times 2)$ structure along with evidence of some disordered and possibly incommensurate phases was found. [205, 206] Bond length changes between the Cs adsorption layer (adlayer) and the Ag(111) substrate surface were studied by surface-extended X-ray absorption fine structure also for higher coverages. [207] *Leatherman and Diehl* provided a structural analysis of Ag(111)-Cs for various coverages and temperatures using low-energy electron diffraction. [208] In particular, for very low coverages they found ring-like diffraction patterns which were assigned to disordered or fluid overlayer phases. This fluid phase appears to be a common arrangement of alkali metal films on metal surfaces at low coverage. [209–212] It is usually argued that at low coverages the dipole-dipole repulsion between the adsorbed alkali metal atoms dominates the alkali-substrate interaction. This results in a structure with no long-range order, yet with a typical distance between the adsorbed atoms (adatoms).

Besides these structural properties, alkali metal-covered surfaces exhibit intriguing electronic properties resulting from quantum size effects: Quantum well states confined to ultrathin films of alkali metals are investigated experimentally as well as theoretically. [213–225]

8.2. Cesium superlattices on Ag(111)

In this section structural properties of various Cs coverages are reported, where the experimental results are modeled by kinetic Monte Carlo simulations. Therefore cesium was deposited at room temperature from commercial dispensers [240] at a rate of $\approx 0.05\,\mathrm{ML\,min^{-1}}$ as monitored by a quartz microbalance and judged from the deposition time and corresponding STM images. We define a monolayer (ML) as one Cs atom per Ag atom. Simulations have been done using the kinetic Monte Carlo method from Refs. [163, 164] and described in Chapter 6.

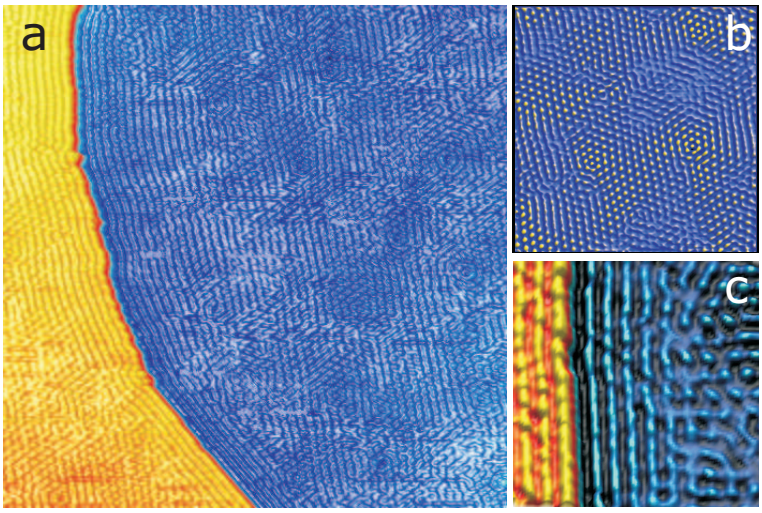

Figure 8.3.: (Color online) (a) STM image of two adjacent terraces of Ag(111) covered with 0.03 – 0.04 ML Cs deposited at room temperature and imaged at 7 K. A monatomically high step separates the terraces (voltage $V = 200\,\mathrm{mV}$, current $I = 0.2\,\mathrm{nA}$, size $97\,\mathrm{nm} \times 97\,\mathrm{nm}$). (b) Close-up view of Cs adatoms on a terrace ($35\,\mathrm{nm} \times 35\,\mathrm{nm}$). (c) Close-up view of the adsorbate arrangement in the vicinity of a step edge ($20\,\mathrm{nm} \times 20\,\mathrm{nm}$).

8.2.1. Low coverage: $\Theta < 0.1$ ML

Figure 8.3 illustrates the main experimental findings at low coverages. The STM image in Fig. 8.3(a) shows two adjacent terraces of a Ag(111) surface covered with 0.03 – 0.04 ML Cs. On terraces we observe local hexagonal order of Cs atoms. Long-range order is suppressed in regions where Cs adatoms are no longer resolved as point-like features [Fig. 8.3(b)]. Rather, these regions are characterized by broadened protrusions extending along the symmetry directions of the adsorbate lattice. From atomically resolved STM images of the adsorbate lattice a mutual adatom distance of $(1.5 \pm 0.2)\,\mathrm{nm}$ was determined. At step edges as well as close to them [Fig. 8.3(c)] adatoms tend to form rows parallel to the step direction separated by $(1.5 \pm 0.2)\,\mathrm{nm}$. Individual Cs adatoms start to be resolved again at distances exceeding 5 nm from the step edge.

In order to understand the observed adsorbate arrangements two central question have to be answered: First, which interactions are taking place between individual Cs atoms? In particular what is the role of the Ag(111) substrate in the growth process? And second, what is the origin of the observed loss of atomic resolution in the STM images? In the following sub-sections these questions will be answered.

The role of surface-state mediated interaction

The dipole-dipole interaction between alkali adatoms are usually used to explain the formation of alkali superstructures on surfaces. While the dipole-dipole interaction presents a direct coupling between adatoms, the substrate may influence the interatomic interaction in an indirect way.

Indirect interaction between two atoms was first investigated theoretically by Koutecký [226] and then by Grimley, [227] Newns, [228] and Einstein and Schrieffer. [229] In an early field ion microscopy experiment evidence for indirect interaction between Re atoms

adsorbed on W(110) was reported by Tsong. [230] In particular, it was found that the interaction energy exhibits an oscillatory behavior as a function of the separation distance between the adatoms. Lau and Kohn [231] then predicted a long-range and oscillatory interaction between atoms mediated by density oscillations of a two-dimensional electron gas. The first scanning tunneling microscopy (STM) experiment evidencing this type of interaction was reported by Repp *et al.* [235] for carbon atoms adsorbed on Al(111). Similar experiments were then performed for benzene molecules on Cu(111), [233] sulfur atoms on Cu(111), [234] copper atoms on Cu(111), [235] cobalt atoms on Cu(111) and Ag(111), [236] and for Ce atoms adsorbed on Ag(111). [237] These experiments reveal that the adatom-adatom distance is predominantly influenced by the surface state-mediated interaction. In particular, the mutual distance is reported to be $\lambda_F/2$ where λ_F denotes the Fermi wavelength of the involved surface state. This interaction may lead to superlattices on surfaces [237] or to confinement-induced adatom self-organization in quantum corrals. [238, 239]

A theoretical analysis of the surface state-mediated interaction energy based on the Harris functional expression was preformed by P. Hyldgaard and M. Persson [241]. For this interaction they derived a non-perturbative analytical estimate. Within this model, the surface state-mediated interaction energy for an atom i at a lattice site r_i can be written as [241]

$$E_i^s = A_0\, E_0 \left[\frac{2\sin(\delta_0)}{\pi}\right]^2 \sum_{j\neq i} \frac{\sin(2k_F|r_j - r_i| + 2\delta_0)}{(k_F|r_j - r_i|)^2} \tag{8.1}$$

with A_0 denoting the scattering amplitude, E_0 the surface state binding energy, δ_0 the scattering phase shift, and k_F the Fermi wave vector. The parameters A_0, E_0, and δ_0 can be determined from STM measurements. From previously published results [234–237] an amplitude of $A_0 \approx 0.3$ is deduced. The scattering phase shift varies between 0.3π and 0.5π [234–237] and within this range the obtained interaction energy does not depend strongly on the specific choice of δ_0. Therefore $\delta_0 = \pi/2$ is used in the following. For clean Ag(111) the surface state binding energy is $E_0 \approx -0.06\,\text{eV}$ below the Fermi energy (see above). Charge transfer from the Cs layer to the substrate, most likely induces a shift of the surface state binding energy to higher values. This shift is estimated from a similar adsorption system, namely Cu(111)-Cs, for which a change of the Cu(111) surface state binding energy has been investigated by photoelectron spectroscopy. [246] By extrapolating the photoemission results to low coverages (0.03 ML), an energy shift of $\approx 0.01\,\text{eV}$ was found.

In order to compare the strength of the dipole-dipole interaction with the interaction mediated by the surface state electrons the dipole moment p is estimated from an individual Cs adatom. Adsorption leads to a considerable charge transfer from an alkali atom to the substrate. [242] As a consequence the adsorbed atom becomes partly ionic and develops a dipole moment which leads to a decrease of the work function. From the initial linear decrease of the work function the dipole moment of the adsorbed species may be evaluated. [242] As shown in Sec. 2.6, the apparent height of the tunneling barrier extracted from current-distance curves can be related to the substrate work function. In particular, from current-distance curves on clean and Cs-covered Ag(111) apparent barrier heights of $\approx 5\,\text{eV}$ and $\approx 4\,\text{eV}$ were inferred. The 1 eV difference of the apparent barrier heights is in good agreement with the work function modifications observed on other surfaces covered with alkali metals. [5, 243, 244] Using a work function change of $\Delta\Phi \approx 1\,\text{eV}$, a dipole moment p

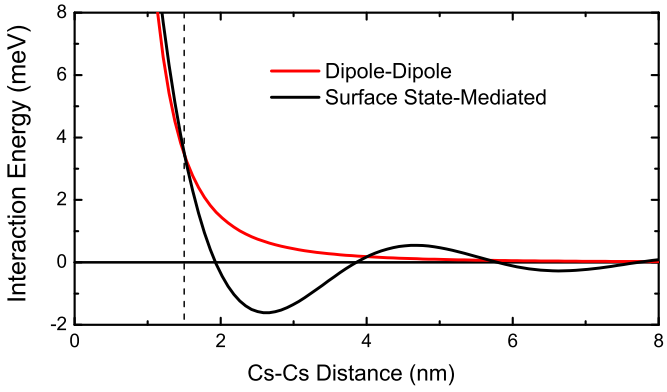

Figure 8.4.: Dipole-dipole interaction energy (gray) and surface state-mediated interaction energy (black) between Cs adatoms on Ag(111) calculated according to Eqs. (8.3) and (8.1) with parameters $p = 0.09\,\mathrm{e\,nm}$, $A_0 = 0.3$, $\delta_0 = \pi/2$, $E_0 = -0.06\,\mathrm{eV}$, and $k_\mathrm{F} = 0.813\,\mathrm{nm}^{-1}$. At the experimentally observed lattice constant of the adlayer, $a \approx 1.5\,\mathrm{nm}$ (dashed line), the surface state-mediated interaction and the dipole-dipole interaction energy have similar values.

is extracted according to [245]

$$\epsilon_0\,\Delta\Phi = \mathrm{e}\,p\,n, \tag{8.2}$$

where $-\mathrm{e}$ is the electron charge and n the surface density of alkali metal atoms. As a result $p \approx (0.09 \pm 0.03)\,\mathrm{e\,nm} = (4.3 \pm 0.7)\,\mathrm{D}$ is obtained. The dipole-dipole interaction of an isolated adatom i at the lattice site r_i with all other atoms $j \neq i$ adsorbed on lattice sites r_j can then described by

$$E_i^\mathrm{d} = \frac{1}{4\pi\epsilon_0} \sum_{j \neq i} \frac{p^2}{|r_j - r_i|^3}, \tag{8.3}$$

where ϵ_0 is the dielectric constant. For the parameters estimated above the interaction energies for the dipole-dipole and the surface state-mediated coupling according to Eqs. (8.3) and (8.1) are calculated. A comparison is shown in Fig. 8.4. At the adsorbate lattice spacing of $a \approx 1.5\,\mathrm{nm}$ observed in the experiment [dashed line in Fig. 8.4] both interaction energies are similar. Therefore, in the following numerical simulations of the low-coverage adatom arrangements both interactions have to be taken into account.

Kinetic Monte Carlo simulations

While from the above performed analysis the type of interactions between Cs adatoms are mainly known, the loss of atomic resolution in STM images [see Fig. 8.3] has still to be answered. For this reason the kinetic Monte Carlo code presented in Chapter 6. As already discussed in Chapter 6 the Ag(111) substrate lattice is modeled by finite hop rates of adatoms between adjacent lattice sites r_i and r_j. The hop rate ν_{ij} is described by an Arrhenius law according to

$$\nu_{ij} = \nu_0 \exp\left(-E_{ij}/\mathrm{k_B}T\right), \tag{8.4}$$

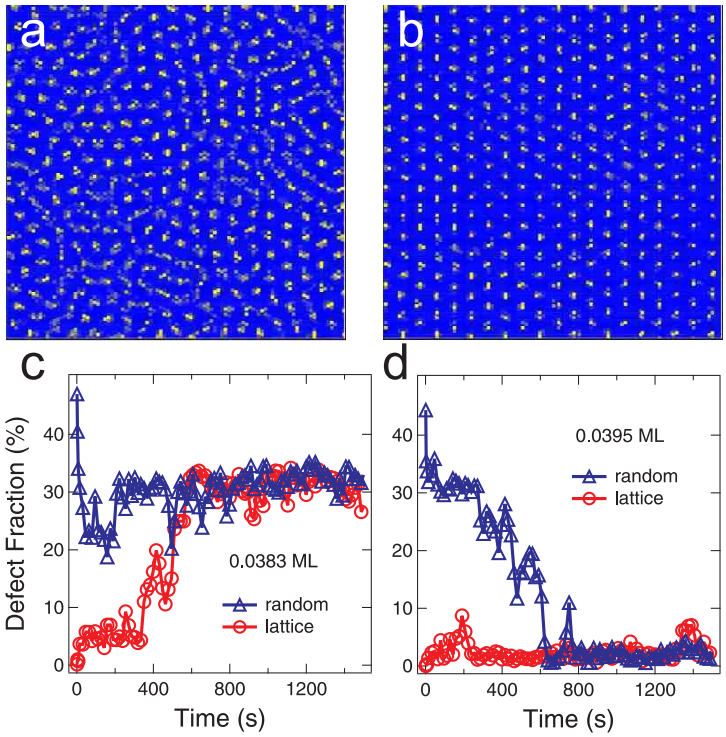

Figure 8.5.: (a), (b) Density plots and (c), (d) defect fractions calculated by kinetic Monte Carlo simulations at $T = 7\,\mathrm{K}$ and $E_\mathrm{D} = 17\,\mathrm{meV}$ for particle coverages 0.0383 ML in (a), (c) and 0.0395 ML in (b), (d). The density plots of $g_\tau(\mathbf{r})$ are calculated at 1000 s using a time averaging interval of $\tau = 16\,\mathrm{s}$. The image size corresponds to 26 nm × 26 nm. The time evolution of the defect fraction q_τ in (c), (d) is shown for a disordered (triangles) and a hexagonally ordered (circles) initial particle arrangement. In the initial equilibration period between 0 and 30 s the defect fraction changes rapidly until the stable or metastable state is reached. The asymptotic stable phase is reached within 800 s.

where T is the substrate temperature, k_B Boltzmann's constant and ν_0 the attempt frequency. For the hopping barrier between lattice sites i and j $E_{ij} = E_\mathrm{D} + 0.5\,(E_j - E_i)$ is used, where E_D is the diffusion barrier height for an isolated adatom and the $E_{j(i)}$ describe the interaction of atom j (i) with all the other atoms given by the sum of Eq. (8.1) and (8.3). In order to describe the dynamics of the system it is desirable to access the probability of finding a particle at a given lateral coordinate. Therefore, for comparison with experimental data we use the time-averaged two-dimensional distribution function, $g_\tau(\mathbf{r})$, which represents the probability of finding a particle at a position $\mathbf{r}$ during a time interval τ, *i. e.*,

$$g_\tau(\mathbf{r}) = \frac{1}{N\tau}\left\langle \sum_{i=1}^{N} \delta(\mathbf{r} - \mathbf{r}_i(t)) \right\rangle_\tau , \tag{8.5}$$

where N is the number of particles used in the simulation. In the following this method is used to describe the experimental situation on a qualitative level.

Beside the parameters of $E_{j(i)}$, which are estimated in the previous paragraphs, E_D of individual adatoms has to be determined. Thus, single Cs atoms are deposited on the cold surface. Upon positioning the tip above the center of a Cs adatom the feedback loop

of the instrument was opened. Next, the time interval was measured from the moment of freezing the feedback loop until the current dropped, which signals that the adatom has moved away from its original position. This procedure resulted in a distribution of time intervals between 1 and 15 s. Together with an assumed attempt frequency of $\nu_0 = 10^{12}\,\mathrm{s}^{-1}$ (Ref. [168]) a diffusion barrier height is estimated between 16 and 18 meV at 7 K. $E_\mathrm{D} \approx 17$ meV matches the time scale of the experiment quite well. However, a word of caution is necessary in this context. Simulated time scales vary with the factor $\nu_0 \exp(-E_\mathrm{D}/\mathrm{k_B}T)$. Consequently, by modifying ν_0, E_D, or both within reasonable limits, experimentally observed time scales may be reproduced. If experimentally observed time scales differ from numerically simulated ones by a factor of more than 10^4, it is no longer reasonable to compensate this discrepancy by an adjustment of ν_0 and E_D. [247] In this case new important physical processes have to be included in the menu of hopping events of the kinetic Monte Carlo algorithm. [167] It turns out that the inclusion of the adatom mutual interactions according to Eqs. (8.3) and (8.1) already leads to correlated transition processes.

With these parameters at hand the experimentally observed coexistence of ordered and less ordered regions is then addressed. Taking into account the experimental uncertainty of the Cs adatom coverage, 0.03 - 0.04 ML, a series of kinetic Monte Carlo simulations is performed at $T = 7$ K and in a coverage regime between 0.035 and 0.040 ML. Two possible asymptotic states are found: A disordered (liquid-like) state [Figs. 8.5(a),(c)] and an ordered (crystalline) state [Figs. 8.5(b),(d)]. Below (above) a critical coverage of $n_\mathrm{c} = 0.0389(6)$ ML the liquid (crystalline) state is stable whereas the crystal (liquid) is metastable. Figures 8.5(a), (b) show density plots of $g_\tau(\mathbf{r})$ averaged over $\tau = 16$ s. In Fig. 8.5(a) the density plot of $g_\tau(\mathbf{r})$ exhibits regions with broad maxima, which tend to overlap and to appear as continuous lines following close-packed directions of the hexagonal particle lattice. The density plot of $g_\tau(\mathbf{r})$ shown in Fig. 8.5(b) is characterized by localized and sharp maxima at the sites of a hexagonal lattice with long-range order. Consequently, depending on the particle density a disorder-to-order transition is observed. In this context, the coexistence of ordered and less ordered regions of the Cs adatom lattice [Fig. 8.3] may be interpreted as the result of locally varying adatom coverages.

To characterize the ordered and disordered phases in more detail, a Voronoï analysis is performed. [248, 249] This analysis provides access to local distortions of the hexagonal symmetry by determining the fraction of particles with a number of nearest neighbors deviating from six. These particles are referred to as defects in the following. The defect fraction are defined according to $q_\tau = N_\tau/(\tau N)$ with N_τ denoting the number of defects recorded during the time interval τ and N the total number of particles. Figures 8.5(c),(d) show the time evolution of q_τ for particle densities of 0.0383 ML and 0.0395 ML, respectively. For long times ($\tau > 800$ s) the defect fraction approaches a value above 30 % (below 2 %) for coverages below (above) n_c. These asymptotic defect fractions depend on the particle density but they do not depend on the initial particle configuration. In Figs. 8.5(c),(d) the time evolution of the defect fraction for two initial configurations is shown. Starting from a disordered (triangles) and from a hexagonally ordered (circles) initial configuration does not alter the asymptotic defect fraction. After initialization the system is allowed to equilibrate with canonical Monte Carlo or kinetic Monte Carlo. With kinetic Monte Carlo simulations it takes about 100 s at 7 K (or $\lesssim 100000$ kinetic Monte Carlo steps) until the system equilibrates in one of the two phases. Typically, in the vicinity of the first-order disorder-to-order transition the system can equilibrate first in

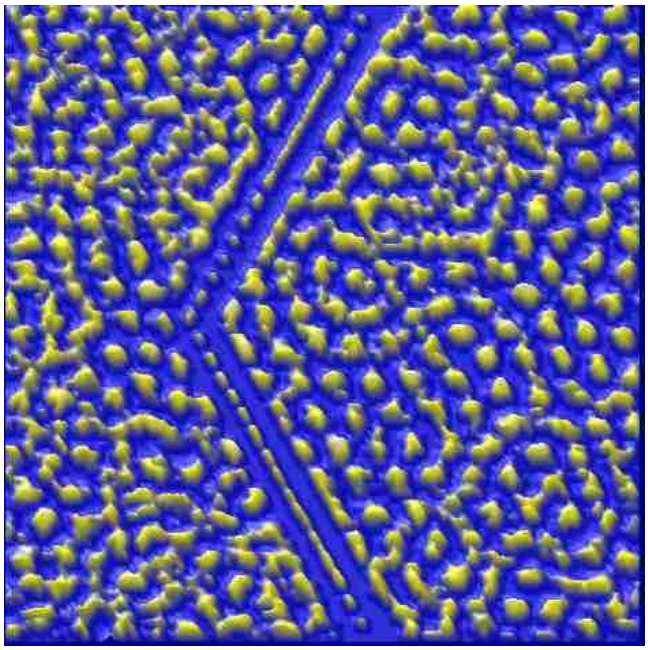

Figure 8.6.: Density plot of $g_\tau(\mathbf{r})$ in the vicinity of a (111) (upper part) and a (100) (lower part) step edge. The simulation area corresponds to an image size of 30 nm × 30 nm. The density plot was generated for $T = 7\,\mathrm{K}$, $\tau = 12\,\mathrm{s}$, and $E_\mathrm{D} = 17\,\mathrm{meV}$.

the metastable phase. The stable phase emerges typically after 800 s.

To model the adsorbate arrangement at step edges, the steps are taken into account as scatterers of the surface state. A step edge is considered as an infinitely long and linear chain of Ag atoms each of which gives rise to a surface state-mediated interaction with Cs adatoms according to Eq. (8.1). Integrating the contribution of each scatterer leads to the total interaction [241, 250]

$$E(r_\perp) = B_0 \frac{\sqrt{5}E_0}{\pi^2 k_\mathrm{F} a_0} \frac{\sin(2k_\mathrm{F} r_\perp + 2\delta_0 + \pi/4)}{\sqrt{k_\mathrm{F} r_\perp}^3}, \tag{8.6}$$

where $r_\perp$ denotes the distance to the step and $a_0 = 0.287\,\mathrm{nm}$ the Ag(111) lattice constant. The parameters E_0, k_F, and δ_0 are the same that were used for modeling the adlayer structure on terraces, while the choice of $B_0 = 4\,\mathrm{meV}$ is in good agreement with the results obtained for Cu atoms adsorbed on Cu(111). [251] Figure 8.6 shows the density plot of $g_\tau(\mathbf{r})$ for $\tau = 12\,\mathrm{s}$. Two kinds of step edges were included in the simulations, namely a step edge of the (111) type (upper part of Fig. 8.6) and a (100) step edge (lower part of Fig. 8.6). Deviating from the KMC simulations of adsorbate structures on terraces we found that the surface state-mediated interaction according to Eq. (8.6) introduced an additional stabilization of the superlattice. The distribution function, $g_\tau(\mathbf{r})$, exhibits overlapping maxima along the step edge directions which is in agreement with Cs adatoms showing elongated rows close to step edges in STM images [Fig. 8.3(c)]. Additionally, maxima of $g_\tau(\mathbf{r})$ become more localized again with larger distances from the step edge and reflect then the characteristic particle arrangement on terraces.

According to the Monte Carlo simulations the experimental observations can be interpreted as a consequence of an enhanced Cs adatom mobility at the low-coverage regime

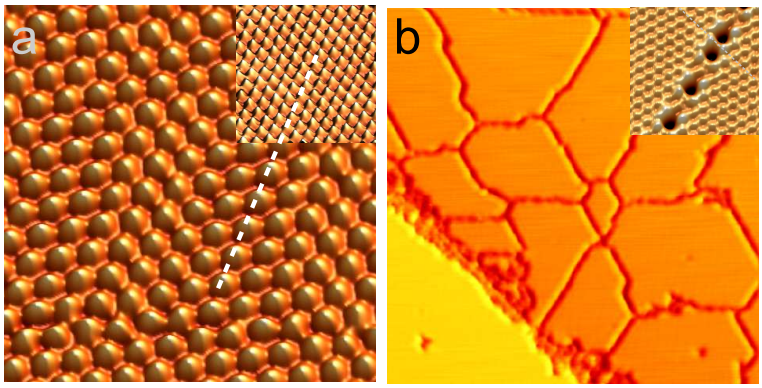

Figure 8.7.: (a) Quasi-three-dimensional representation of constant-current STM image of Ag(111) covered with 0.11 ML of Cs ($V = 0.25\,\mathrm{V}$, $I = 0.1\,\mathrm{nA}$, $10\,\mathrm{nm} \times 10\,\mathrm{nm}$). Cesium adatoms which appear as almost circular protrusions exhibit a mutual distance of 0.74 nm. Inset: Atomically resolved Ag(111) lattice. The dashed line indicates that adlayer and substrate lattice have the same orientation. (b) STM image of Cs-covered Ag(111) at 0.15 ML ($V = 1.2\,\mathrm{V}$, $I = 0.2\,\mathrm{nA}$, $80.4\,\mathrm{nm} \times 80.4\,\mathrm{nm}$). Lines on terraces which contain irregularly shaped structures appearing as depressions at the applied tunneling voltage are boundaries between translational domains of the adsorbate lattice. Inset: Atomically resolved Cs domains. While the orientation of the adjacent domains is identical, the lattices are translated by half a superlattice constant (see dashed line).

discussed in this section. The origin of the observed mobility can be identified as a property of adatom coverages, which are slightly lower than a critical coverage leading to a *disorder-to-order transition*.

8.2.2. Higher coverages: $\Theta > 0.1$ ML

A way to stabilize the adsorption lattice, *i. e.*, to obtain a hexagonal superstructure with long-range order, is the increase of the coverage. Many structural analyses of alkali metal films adsorbed on metal surfaces have previously reported the transition from a disordered phase at very low coverage to well-ordered adsorbate structures at higher coverages (Ref. [204] and references therein). An increased coverage leads to a smaller adatom-adatom distance and will therefore increase the dipole-dipole repulsion between the adatoms. As a consequence, the probability for a Cs atom to hop from one adsorption site to an adjacent one is lowered. The experimental and calculated results presented below corroborate this picture.

Figure 8.7(a) shows an STM image of Ag(111) covered with 0.11 ML of Cs. A hexagonal adlayer with long-range order and a mutual adatom distance of $(0.74 \pm 0.04)\,\mathrm{nm}$ is observed. This adsorbate superstructure corresponds to a (3×3) commensurate phase and has been observed before by low-energy electron diffraction. [208] The inset of Fig. 8.7(a) shows the atomically resolved Ag(111) lattice to indicate that the adlayer and substrate lattice exhibit the same orientation [see dashed line in Fig. 8.7(a)]. Regions indicating an enhanced mobility of adatoms are no longer present at this coverage. Given that the commensurate adsorbate phase is observed experimentally at a specific coverage, simulations for an adatom lattice matching the substrate lattice are performed. The superstructure similar to the one observed in the experiments was obtained as the ground state from

canonical Monte Carlo calculations. The distribution function $g_\tau(\mathbf{r})$ for this coverage was then calculated for a variety of time intervals. Even for extended intervals, *e. g.*, $\tau = 35\,\mathrm{s}$, no enhancement of the diffusion processes was observed indicating that the increased dipole-dipole coupling stabilizes the hexagonal adsorption lattice.

The same behavior was observed at higher coverages. Figure 8.7(b) shows an STM image of Ag(111) covered with 0.15 ML Cs. Again, no indication of enhanced diffusion of Cs adatoms was found. The Cs adatoms are arranged in an incommensurate hexagonal superlattice with a mutual distance of $\approx 0.66\,\mathrm{nm}$ and rotated with respect to the Ag(111) lattice by $\approx 19°$. Moreover, at this coverage domains of hexagonally ordered Cs atoms were observed. Cesium atomic rows of adjacent domains are offset by half an adlayer lattice constant [see inset of Fig. 8.7(b)]. At the domain boundaries rows of irregularey shaped structures occur whose apparent height depends on the tunneling voltage. The formation of domains may be understood in terms of stress release at the domain boundaries. Similar observations of translational adsorbate domains have been reported for oxygen adsorption on W(110) [252] and on Rh(111). [253]

To model these observations within a kinetic Monte Carlo approach particle arrangements are simulated for coverages ranging between 0.11 ML and 0.2 ML [Fig. 8.8]. After an interval of $\tau = 12\,\mathrm{s}$ has elapsed the coordinates of 340 particles with a coverage of 0.11 ML are given by the upper left plot in Fig. 8.8. This coverage corresponds to the (3×3) commensurate adsorption phase and it can be observed that the superlattice aligns with the crystallographic direction of the substrate lattice (depicted as the horizontal arrow). With increasing coverage this alignment weakens. At 0.132 ML some domains are still oriented along the substrate crystallographic direction while others enclose an angle of $\approx 20°$ indicating that at 0.132 ML commensurate and incommensurate phases coexist. This coexistence is in agreement with previous reports based on low-energy electron diffraction. [208] At 0.136 ML all particle domains exhibit a rotation angle of $\approx 20°$. This angle is maintained until at 0.2 ML the particle lattice is aligned with the substrate lattice again. In particular, the incommensurate phase observed experimentally at 0.15 ML with a rotation angle of $\approx 19°$ is well reproduced by this simulations. In Fig. 8.9 calculated and measured rotation angles as a function of the coverage are summarized. These simulations reproduce the experimentally observed rotation angles for commensurate adsorbate phases.

Besides the rotation angle of commensurate superstructures the simulations indicate the origin for domain formation as observed experimentally at 0.15 ML [Fig. 8.7(b)]. Increasing the particle density in the simulations to 0.14 ML and thus being close to the $(\sqrt{7} \times \sqrt{7})R19.1°$ commensurate phase leads to a particle arrangement where the domains have almost disappeared in favor of a nearly homogeneous particle film with long-range hexagonal order. At a particle coverage of 0.155 ML the boundaries of adjacent domains overlap leading to an increase of the particle interaction at the boundaries. A further increase of the particle density to 0.2 ML induces a decrease of the domain size and leads to a similar particle arrangement as observed for 0.136 ML. As a result, the particle coverages giving rise to incommensurate phases exhibit the propensity to form domains, while commensurate phases lead to homogeneous films.

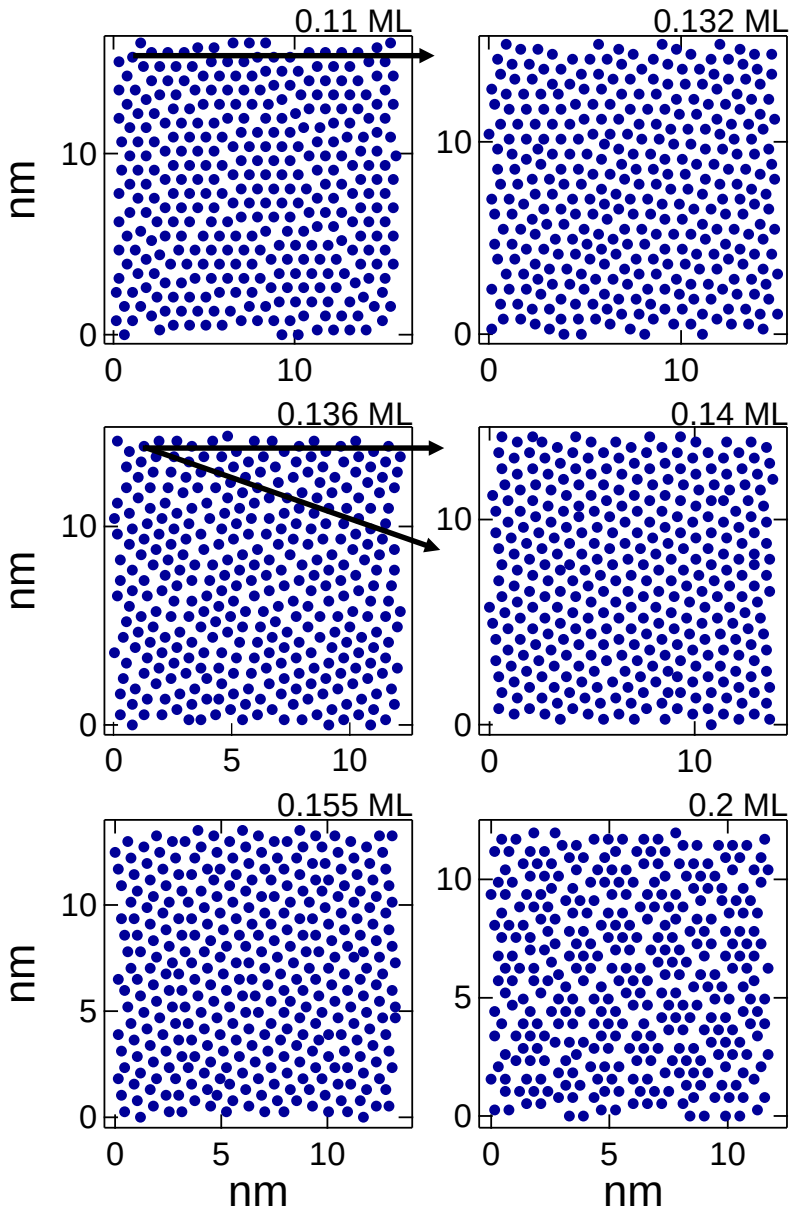

Figure 8.8.: Arrangement of 340 particles according to kinetic Monte Carlo simulations using a time averaging interval of $\tau = 12\,\mathrm{s}$ and a substrate temperature of $T = 7\,\mathrm{K}$. The coverages are indicated at the top right of each plot. The horizontal (inclined) arrow indicates the crystallographic direction of the substrate (particle lattice). The rotation angle is defined as the smaller angle enclosed by the two arrows.

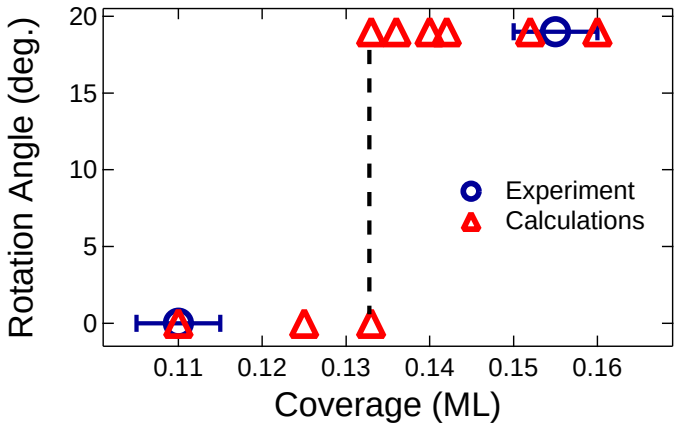

Figure 8.9.: Rotation angle of the superlattice with respect to the substrate lattice. Experimental data are depicted as circles and calculated data as triangles. The dashed line indicates a coverage at which two phases with different rotation angles coexist.

8.3. Surface-state localization at adatoms

Besides the structural properties, as explained in detail in the previous section, Ag(111)-Cs exhibits intriguing electronic properties, which will be the topic of this section. It will be experimentally and theoretically shown that an alkali metal atom adsorbed on Ag(111) induces an occupied localized state derived from the two-dimensional surface state continuum. The contributions to the spectroscopic line shape and decay rate of this state can be identified. The resonance decays due to resonant charge transfer and inelastic processes. In addition, Cs-Ag zero point vibrations, which do not influence the decay rate, contribute to the broadening of the resonance line.

8.3.1. Decay of surface-localized electronic excitations

Decay rates of surface-localized electronic excitations may provide valuable insight into quasi-particle interactions, since these excitations determine the dynamics of charge and energy transfer. STS can be used to determine the lifetime of surface-localized electronic excitations. For this reason, the line shapes of spectroscopic signatures in $\mathrm{d}I/\mathrm{d}V$ data are analyzed, where the width of these signatures reflects the lifetime [287, 288], as for a Lorentzian line shape their full width at half maximum. In particular, the measured width Δ is related to the imaginary part of the self-energy via [287]

$$\Delta = \beta\pi \mathrm{Im}\Sigma = \beta\pi\frac{\Gamma}{2} \tag{8.7}$$

where $\mathrm{Im}\Sigma = \Gamma/2$ denotes the imaginary part of self-energy which is related to the half width at half maximum, $\Gamma/2$, of the surface state; β is a number reflecting the probability of finding the electron in the tunneling barrier region where $\mathrm{Im}\Sigma = 0$. The self-energy concept allows to describe many-body physics and to include lifetime effects. In order to compare lifetime data originating from, for instance, angle-resolved photoelectron spectroscopy with

STS data the linewidth Γ is related by [287, 288]

$$\tau = \frac{\hbar}{\Gamma} \tag{8.8}$$

to the lifetime τ. However, various scattering processes, like electron-electron, electron-phonon and electron-defect scattering, can influence the linewidth and hence the total linewidth Γ is sum of all these contributions. In this context, angle-resolved photoelectron spectroscopy, scanning tunneling spectroscopy, and time-resolved two-photon photoemission have been used to investigate these lifetimes. [254] Several contributions to the decay of surface-localized states were unraveled, among which the most prominent are electron-electron and electron-phonon interactions, as well as charge transfer in the case of localized states. [254, 255] The origin of these contributions will be reported next.

Inelastic interactions

The mainly dominating inelastic processes, which influence the lifetime of surface-localized electronic excitations are given by electron-electron and electron-phonon interactions [254]. The underlying physics can be understood with the help of Fig. 8.10(a). An excited hole in the surface state band, which results from an electron tunneling out of the bottom of the band, relaxes via electron–electron and electron–phonon scattering. Both electron–electron scattering within the surface-state band (intraband scattering) and electron–electron scattering with surface-projected bulk states (interband scattering) occur. In general, electron–electron scattering within surface states is the dominating process due to the greater overlap between the hole and surface-band electron wave functions.

Resonant charge transfer

Resonant charge transfer of electrons occurs between adatom states that are resonant with the substrate levels. The diagram in Fig. 8.10(b) shows a metallic substrate with all states below the Fermi level filled. An atom moves towards the substrate surface from an infinite distance from the surface. When the atom is located at an infinite distance from the surface, it has discrete energy levels. As it moves closer to the surface, the discrete atomic states interact with the metal states resulting in a broadening of the atomic levels. If the atom is ionized, it sees an image charge on the metal surface. Due to the interaction of the charge with its image, the ionization levels shift.

In addition, in the case of electronic continua at surfaces, the presence of adsorbates, steps, defects, or ordered overlayers of adsorbates induce scattering phenomena leading to extra broadening effects. [224, 256–259] Scattering by impurities at surfaces has recently received much attention. [260–267] For example, scattering of image potential states by Cu atoms adsorbed on Cu(100) [261, 262] has been shown to contribute significantly and differently to the decay and broadening of these states.

8.3.2. Broadening of surface-localized excitations

Alkali metal atoms adsorbed on noble metal surfaces, *e. g.*, Cu(111)-Na, [268] Cu(111)-Cs, [217, 218] and Ag(111)-Cs, [269, 270] induce long-lived unoccupied resonances within the surface-projected band gap. These resonances correspond to the transient capture of

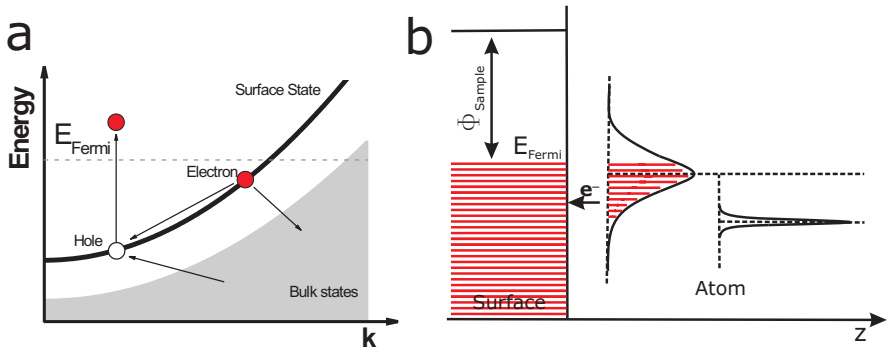

Figure 8.10.: (a) Diagram of electron-electron scattering of surface-state electrons. While the black line presents the surface-state band, the shaded area marks the bulk states. An excited electron from the surface-state band leaves a hole. Surface-state electrons with a higher energy, as well as electrons from the bulk can scatter into the hole. (b) Diagram of resonant charge transfer: An atom moves towards the surface, the discrete atomic states interact with the metal states resulting in a broadening of the atomic levels and charge transfer of electrons occurs between adatom states that are resonant with the metal levels.

an electron on a *sp* hybrid orbital of the alkali metal atom. The very low decay rates of these resonances have been explained by a quasi-blocking of the resonant charge transfer between the resonance and the substrate due to the presence of the surface-projected band gap. While resonant charge transfer rates for an alkali atom on a free-electron metal may reach 1 eV, [271] it can be reduced to a few meV if a surface-projected band gap is present. [272] Surprisingly, the spectral widths of these resonances are much larger than their decay rate would explain, indicating the existence of extra sources of broadening. In a recent theoretical analysis, the peculiar linewidth and its temperature dependence were traced back to an inhomogeneous broadening due to the distribution of adsorption heights of the alkali adsorbate. [223]

Alkali metal atoms have also been predicted to induce occupied resonances on surfaces as a result of the localization of the two-dimensional surface state continuum, [273,274] when the latter exists. While these states have been reported in the case of noble metal [263,264] and magnetic [264, 275] adatoms, they have not been observed for alkali adsorbates until now.

8.3.3. STS on individual Cs adatoms

Fig. 8.11 presents a $\mathrm{d}I/\mathrm{d}V$ spectrum acquired from single Cs atoms adsorbed on Ag(111). A prominent peak appears at $\approx -80\,\mathrm{meV}$ below the Fermi level, which is located at $V = 0\,\mathrm{V}$ [Figure 8.11, black curve]. The additional spectroscopic structures visible at $\approx -50\,\mathrm{meV}$ are not visible in spectra of clean Ag(111), which were acquired with the same tip. Consequently, we can rule out tip electronic structure as the origin. These structures may rather be a remnant of the Ag(111) surface state or they may be related to additional Cs-induced states. A typical spectrum acquired on an individual Cs atom residing in the adsorbate layer shown in Fig. 8.3 is presented in Fig. 8.12. The spectrum exhibits the same characteristics as the spectrum taken on a single adatom. But the peak maximum occurs at $\approx -83\,\mathrm{meV}$ in Fig. 8.12 and consequently is by $\approx 3\,\mathrm{meV}$ lower than

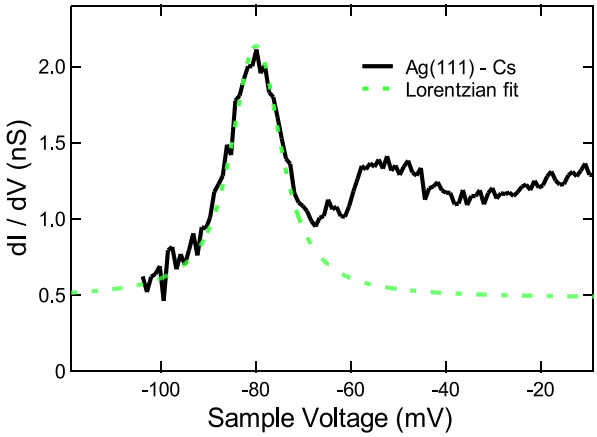

Figure 8.11.: Spectrum of the differential conductance ($\mathrm{d}I/\mathrm{d}V$) taken at 7 K on a single Cs atom adsorbed on Ag(111) (solid line). The tunneling gap was defined by opening the feedback loop at 0.1 nA, 50 meV. The dashed line is a Lorentzian, which was fit to the resonance.

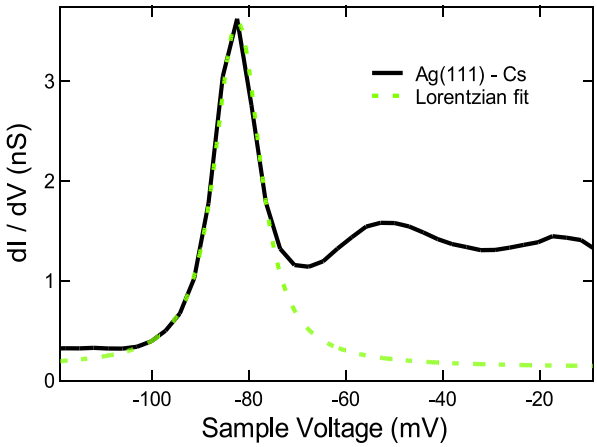

Figure 8.12.: Spectrum of $\mathrm{d}I/\mathrm{d}V$ acquired on a Cs atom in a 0.03 ML thick Cs layer on Ag(111) presented in Fig. 8.3. The tunneling gap was defined at 0.1 nA and 200 mV. The dashed line is a Lorentzian fitted to the resonance.

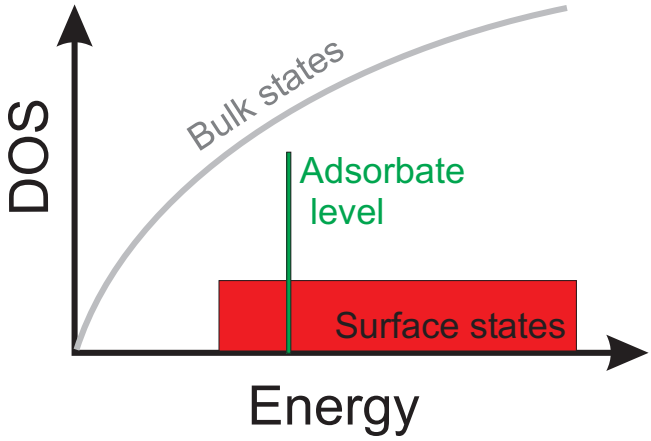

Figure 8.13.: Schematic representation of the extended Newns-Anderson model [264]: An adatom described by a single valence state ϕ_a with an energy ϵ_a interacting with the substrate bulk states and surface states.

the peak maximum in the spectrum of the single Cs adatom [Fig. 8.11]. This shift may be partly due to a surface state shift owing to charge transfer from the alkali metal layer to Ag(111). Already at small coverages, alkali metal adsorption is known to induce a considerable charge transfer, as reported in Sec. 8.1.2. An additional contribution to the observed energy shift may be due to the electric field of the tip. [281, 282]

To extract the intrinsic widths of the Cs-induced resonances a Lorentzian line shape with a full width at half maximum (FWHM) Γ_0 was convoluted with functions describing thermal and instrumental broadening [functions are defined in Sec. 2.3.2]. The resulting function was then fit to experimental data. At 7 K the thermal broadening function exhibits a FWHM of ≈ 2.1 meV, while a root-mean-square amplitude of the voltage modulation of 1 mV used for the lock-in detection of the tunneling current gives rise to a FWHM of the instrumental broadening function of ≈ 2.4 mV. As a result we obtain $\Gamma_0 = (12.0 \pm 2.0)$ meV for single Cs adatoms and $\Gamma_0 = (9.5 \pm 0.5)$ meV for Cs atoms embedded in the Cs layer. The convoluted line shapes are depicted as dashed lines in Figs. 8.11 and 8.12.

8.3.4. Newns-Anderson Model

Adsorption at surfaces corresponds to the making of localized bonds between substrate and adsorbate. This leads to significant hybridization between the adsorbate and substrate electronic states. To interpret the modification of the spectral features in terms of an adsorbate-substrate coupling we might apply the Newns-Anderson model [292] in an extended version following Limot et al. [264].

Consider an adatom described by a single valence state ϕ_a with an energy ϵ_a interacting with the substrate quasi-continuum of Bloch bulk states $\phi_{\mathbf{q}}$ with eigenenergies $\epsilon_{\mathbf{q}}$, as shown in Fig. 8.13. In the extended version of this model a second interaction to the Ag(111) surface states $\phi_{\mathbf{k}}$ is added with eigenenergies $\epsilon_{\mathbf{k}}$. The interaction can be described by the following model Hamiltonian [264]:

$$H = \begin{pmatrix} \epsilon_{\mathrm{a}} & V_{\mathrm{a}\mathbf{q}} & V_{\mathrm{a}\mathbf{k}} \\ V^*_{\mathrm{a}\mathbf{q}} & \epsilon_{\mathbf{q}} & 0 \\ V^*_{\mathrm{a}\mathbf{k}} & 0 & \epsilon_{\mathbf{k}} \end{pmatrix}, \tag{8.9}$$

where $\epsilon_{\mathbf{q}}$ and $\epsilon_{\mathbf{k}}$ are submatrices in this notation. The interaction of the adatom state with substrate and the surface states is given by $V_{\mathrm{a}\mathbf{q}}$ and $V_{\mathrm{a}\mathbf{k}}$, respectively. In principle the Hamiltonian could be written as a sum over independent one-particle states, but even then a direct solution of the Schrödinger equation is impossible due to the infinite number of bulk states. The key to derive some fundamental aspects of the behavior of the adatom valence state ϕ_{a} from the model is given by the projected density of states

$$n_{\mathrm{a}}(E) = \sum_i |\langle \phi_{\mathrm{i}} | \phi_{\mathrm{a}} \rangle|^2 \, \delta(E - \epsilon_{\mathrm{a}}) = -\frac{1}{\pi} \operatorname{Im} G_{\mathrm{aa}}(E), \tag{8.10}$$

where G is the single particle Green function, formally defined by $(E - H + \mathrm{i}\delta)G(E) = 1$. Applying standard Green function techniques, G_{aa} can be written in the following form:

$$G_{\mathrm{aa}}(E) = \frac{1}{E - \epsilon_{\mathrm{a}} - \Sigma(E)}. \tag{8.11}$$

Here the imaginary self-energy $\Sigma(E) = \Lambda(E) - \mathrm{i}\Delta(E)$ consists of contributions from the coupling of the adatom valence state ϕ_{a} to bulk and surface states, respectively:

$$\Delta(E) = \Delta_{\mathrm{b}}(E) + \Delta_{\mathrm{s}}(E). \tag{8.12}$$

The contributions to bulk and surface states are given by

$$\Delta_{\mathrm{b}}(E) = \pi \sum_q |V_{a\mathbf{q}}|^2 \delta(E - \epsilon_{\mathbf{q}}) \tag{8.13}$$

and

$$\Delta_{\mathrm{s}}(E) = \pi \sum_k |V_{a\mathbf{k}}|^2 \delta(E - \epsilon_{\mathbf{k}}). \tag{8.14}$$

The real part of the self-energy $\Lambda(E)$ can be calculated via a Hilbert transform from $\Delta(E)$ [296]:

$$\Lambda(E) = \frac{1}{\pi} \mathrm{P} \int \frac{\Delta(E')}{E - E'} dE', \tag{8.15}$$

where P denotes the principal part value. Inserting Eq. (8.11) into Eq. (8.10) leads to the projected DOS at the adsorbate atom

$$n_{\mathrm{a}}(E) = \frac{1}{\pi} \frac{\Delta(E)}{[E - \epsilon_{\mathrm{a}} - \Lambda(E)]^2 + \Delta(E)^2}. \tag{8.16}$$

Δ_{b} can be assumed to be independent of the energy, if the substrate band width is much larger than the coupling matrix elements $V_{a\mathbf{q}}$ in the energy range of interest. In this case $\Lambda(E)$ can be calculated from

$$\Delta_{\mathrm{s}}(E) = \Delta_{\mathrm{s}} \Theta(E - E_0), \tag{8.17}$$

which is assumed to be governed by the step-function behavior of the surface state including lifetime effects [264]:

$$\Lambda(E) = \frac{\Delta_{\mathrm{s}}}{2\pi} \ln \left[(E - E_0)^2 + (\Gamma/2)^2 \right] + \mathrm{const}, \tag{8.18}$$

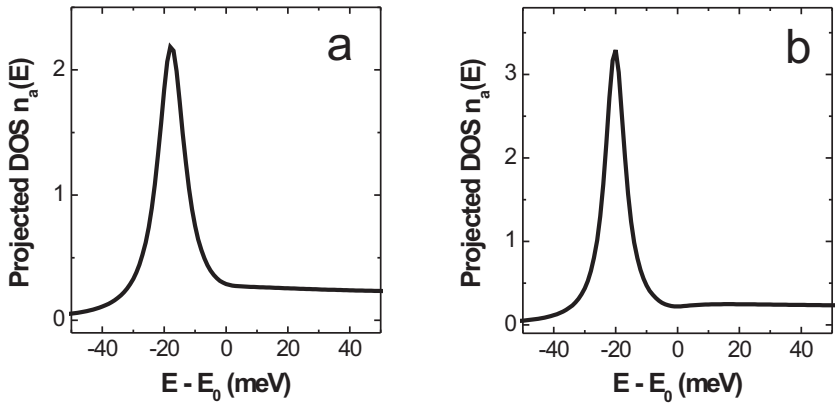

Figure 8.14.: Projected density of states at the Cs adsorbate position: (a) Calculated spectra for a single Cs atom adsorbed on Ag(111) and (b) for a Cs atom in a Cs layer. The used parameters to reproduce the experimental spectra are summarized in Table 8.1

	Γ (meV)	Γ_0 (meV)	ϵ'_a (meV)	Δ_s (meV)
single Cs	13.1 ± 2.0	12.0 ± 2.0	475.0 ± 5.0	430 ± 10
Cs layer	11.1 ± 2.0	9.5 ± 0.5	495.0 ± 5.0	430 ± 10

Table 8.1.: Parameters of Eq. (8.16) employed to reproduce the experimental Cs-induced localized resonance. Γ denotes the full width at half maximum (FWHM) of the resonance measured in spectra of $\mathrm{d}I/\mathrm{d}V$, while Γ_0 is the intrinsic FWHM without thermal and instrumental broadening. E_0 was fixed to the surface-state energy onset at $-63\,\mathrm{meV}$ and Δ_b is found to be zero.

where Γ is the inverse lifetime and E_0 the onset of the surface state. This model predicts a bound state which splits off from the bottom of the surface state band due to the coupling between adsorbate state and surface state. Furthermore this bound state broadens into a resonance by the coupling to the bulk states. The including of lifetime effects in Eq. (8.18) leads to an increased line width, and a smoother variation around the onset of the surface band

The presented surface-state DOS (Eq. (8.16)) was used to reproduce the experimental data. The resulting spectra are shown in Fig. 8.14 and the corresponding parameters are summarized in Tab. 8.1. The surface-state band onset E_0 was fixed to the unshifted surface state at $-63\,\mathrm{meV}$ and the linewidths of the Cs-induced localized resonance are set to intrinsic FWHM without thermal and instrumental broadening, which was extracted from the measured $\mathrm{d}I/\mathrm{d}V$ spectra shown in Figs. 8.11 and 8.12. In order to reproduce the line shape of experimental spectra the rest of parameters of Eq. (8.16) are taken as free fit parameters. As a result, the eigenenergy of the adsorbate level ϵ'_a is found at $(-475 \pm 5)\,\mathrm{meV}$ for a single Cs adatom and at $(-495 \pm 5)\,\mathrm{meV}$ for a Cs atom embedded into an ultrathin Cs layer, where the surface-state band edge E_0 was taken as energy reference according to $\epsilon'_\mathrm{a} = \epsilon_\mathrm{a} + E_0$. According to Ref. [275] it can be assumed that ϵ'_a is

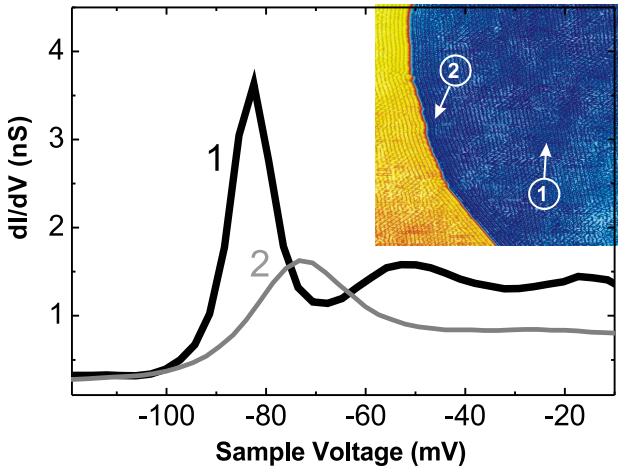

Figure 8.15.: Spectra of $\mathrm{d}I/\mathrm{d}V$ acquired on Cs atoms in a 0.03 ML thick Cs layer on Ag(111): While the black line (labeled 1) is a spectrum recorded on the terrace, the gray (labeled 2) is taken at the bottom of a Cs covered monoatomic step of Ag(111). The tunneling gap was defined at 0.1 nA and 200 mV. Inset: STM image of two adjacent terraces of Ag(111) covered with 0.03 – 0.04 ML Cs deposited at room temperature and imaged at 7 K. A monoatomically high step separates the terraces (voltage $V = 200$ mV, current $I = 0.2$ nA, size 55 nm $\times$ 55 nm).

the energy of a narrow s-like resonance, exhibiting a significant overlap with surface-state band. Moreover, the coupling Δ_b to the bulk conduction band is found to be nearly zero, which implies a strong coupling of $\Delta_\mathrm{s} = (430 \pm 10)$ meV to the surface-state band.

To discuss these findings in some more detail, we want to explore the role played by the Ag(111) surface-state electrons. Therefore conductance spectra are taken close to a monoatomic step edge [Inset Fig. 8.15], where the surface state LDOS ρ_s is strongly perturbed due to a superimposing of incoming and reflected surface state waves [293]. Moreover this perturbation of the surface state LDOS leads to a depopulation of electrons from the surface-state band near a step edge [294]. In Fig. 8.15 a spectrum acquired at the center of a Cs covered terrace on Ag(111) (black line, labeled 1) is compared with a spectrum taken near the monoatomic step edge (gray line, labeled 2). The most significant spectroscopic differences are a shift of the peak position of 10 mV towards the Fermi energy and a broadening of the linewidth of the resonance by 20 mV. Hence, the state close to and below the the surface state most originates from the localization of the two-dimensional surface-state by the attractive Cs adsorbate.

Focusing on Γ, we find that the invers lifetime measured on a Cs atom embedded into a Cs layer, and on a single Cs adatom is much larger compared to the measured value of $\Gamma = 6.0$ mV obtained onto the clean Ag(111) surface. This finding indicates the existence of additional decay channels. However, in the framework of the applied Newns-Anderson model the different contributions to the measured linewidth could not be identified. To overcome these limitations a theoretical investigation is needed, which characterises the Cs induced excited states, the origin of their long lifetimes, as well as

the resulting consequences for the adsorbate dynamics.

8.3.5. Linewidth of a cesium adatom resonance

To identify the different contributions to the spectroscopic line shape of the observed Cs resonances a modeling of the system is needed. Since a direct determination of excited states by the coupling of quantum electronic structure methods with dynamical simulations is not computationally feasible, *A. G. Borisov*, and *J. P. Gauyacq* performed simulations using a one-electron wave-packet approach (WPP). In this approach a mixed quantum-classical dynamic method is realized, which determines the time evolution of an excited electron interacting with the *static* single adsorbate-substrate system. This method is based on the separation of the kinetic energy of the classical particles from the total Hamiltonian:

$$H = T_{\mathbf{R}} + H_{\mathrm{el}}(\mathbf{r}, \mathbf{R}) \tag{8.19}$$

where $\mathbf{R}$ are the classical and $\mathbf{r}$ are the quantum degrees of freedom. H_{el} is the one-electron Hamiltonian,

$$H_{\mathrm{el}} = T + V_{\mathrm{Surf}} + V_{\mathrm{Ads}} + \Delta V_{\mathrm{Surf}} \tag{8.20}$$

which consists of the electron kinetic energy T, the electron-clean metal surface interaction V_{Surf}, the electron-adsorbate interaction V_{Ads}, and ΔV_{Surf} the modification of the electron-metal interaction induced by the presence of the adsorbate. Therein, the single Cs adsorbate is modeled as a positive ion and the electron-substrate interaction is described by a local potential from Ref. [277]. The calculations were performed in cylindrical coordinates, with the z axis perpendicular to the surface and going through the adsorbate center. Following the symmetry of the Cs-induced resonance only the $m = 0$ component (m is the electron momentum projection on the z axis) is studied, which reduced the wave-packet to two dimensions ($\mathbf{r} = (\rho, Z)$). The time evolution of the electron wave function $\psi(\mathbf{r}, \mathrm{t})$ is given by the time-dependent Schrödinger equation

$$i\frac{\mathrm{d}\psi(\mathbf{r}, \mathrm{t})}{\mathrm{d}t} = H_{\mathrm{el}}\psi(\mathbf{r}, \mathrm{t}). \tag{8.21}$$

Where the time propagation of the electron wave function is obtained using the evolution operator $U(\Delta\mathrm{t})$:

$$\psi(\mathbf{r}, \mathrm{t} + \Delta\mathrm{t}) = U(\Delta\mathrm{t})\psi(\mathbf{r}, \mathrm{t}) \tag{8.22}$$

where

$$U(\Delta\mathrm{t}) = \exp(-iH_{\mathrm{el}}\Delta\mathrm{t}). \tag{8.23}$$

The time propagation starts with an initial electron wave function $\psi(\mathbf{r}, \mathrm{t} = 0)$, which is taken equal to the eigenfunction $\psi_a(\mathbf{r})$ of the used local potential. For a fixed adsorbate-surface distance the electron dynamics can then be studied using the electronic wave-packet autocorrelation function [276]

$$A = \langle \psi_a(\mathbf{r}) \, | \psi(\mathbf{r}, \mathrm{t}) \rangle \, . \tag{8.24}$$

From the real part of the Laplace transform of Eq. (8.24)

$$g(\omega) = \frac{1}{\pi}\int_0^\infty e^{i\omega t} A(t)\mathrm{d}t \tag{8.25}$$

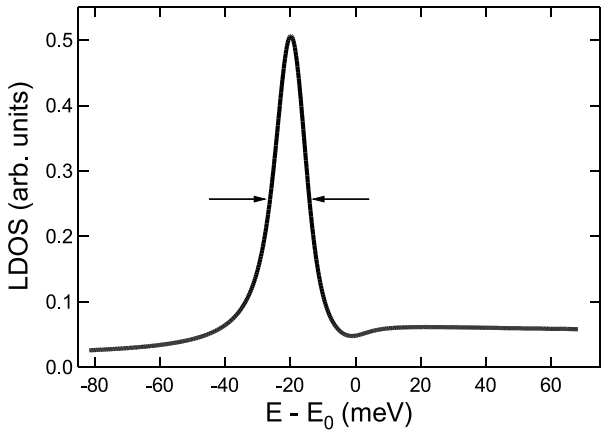

Figure 8.16.: Calculated local density of states (LDOS) of the Cs-induced resonance as a function of energy, E (static adsorbate, black). The resonance maximum is located $\approx 20\,\text{meV}$ below the surface state onset. The linewidth of the resonance (static adsorbate) is 9.1 meV.

the local density of states (LDOS) can be calculated. From the width of the obtained Lorentzian peak at the resonance position, characteristics (energy, decay rate) of the *static* quasi-stationary states of the system can be extracted. [273, 276] Some test studies on the case of a finite Cs coverage were performed using the modeling from Ref. [278]. The calculations reveal the existence of a quasi-stationary state located slightly below the surface state band bottom. Its energy and width were determined as functions of the adsorbate-surface distance Z.

The obtained spectrum is shown in Fig. 8.16. A sharp peak appears in the local density of states below the surface state threshold, similarly to earlier predictions for Cu(111)-Cs. [273] The resonance wave function for a fixed adsorbate-surface distance has been computed with WPP and is shown in Fig. 8.17. Except close to the adsorbate center, the resonance wave function looks like the surface state wave function along the coordinate perpendicular to the surface and exhibits a broad featureless structure parallel to the surface. The resonance decay by the energy-conserving (resonant) electron transfer from the adsorbate-localized state into the continuum of metal states appears in Fig. 8.17 as an outgoing electron flux inside the bulk, enclosing a finite angle with the surface normal. All this confirms that the state close to and below the surface state originates from the localization of the two-dimensional continuum by the attractive Cs adsorbate.

A detailed comparison of the experimental and calculated peak positions is complicated by the presence of a biased STM tip in the experiment. This leads to a modified image potential and a "Stark" shift of the surface state. [281, 282] Since the studied resonance arises from the surface state continuum localisation, it is expected to exhibit a "Stark" shift similar to that of the surface state, so that the resonance position with respect to the surface state band bottom should be only weakly influenced by the electric field of the microscope's tip. Indeed, the calculated resonance position, which is $\approx 20\,\text{meV}$ below the surface state band, reasonably agrees with the experimental offset of $\approx 17\,\text{meV}$ below the band edge of the unshifted surface state at $-63\,\text{meV}$. [283] The influence of the tip on the lifetime is expected to be negligible. [284]

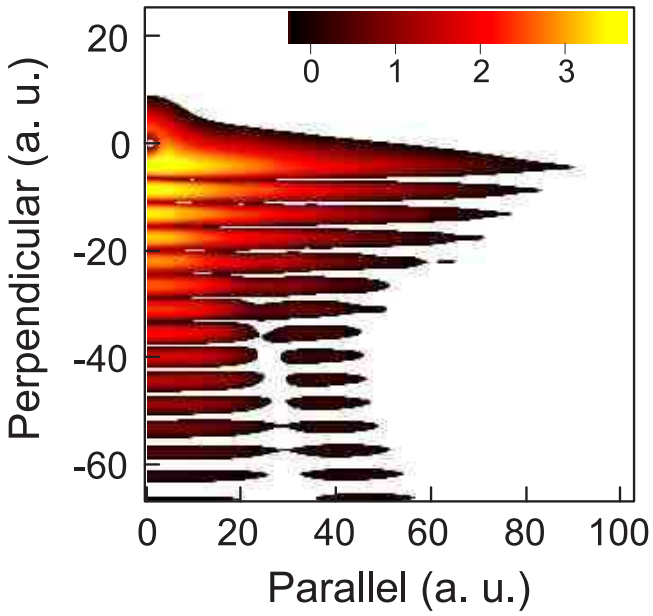

Figure 8.17.: Contour map of the logarithm of the electron density associated with the Cs resonance, which is localized below the surface state band, as a function of the electron coordinates parallel and perpendicular to the surface. The adsorbate center is at the origin of the coordinates and negative coordinates are inside the substrate. The color code is given in the inset: light yellow corresponds to high electron densities, dark to small densities, and white to very low densities.

In the experiments, stable spectroscopy of single Cs adatoms on Ag(111) was often hampered by the mobility of the adatoms. Though $\mathrm{d}I/\mathrm{d}V$ spectroscopy was performed at very low tunneling currents, the signal-to-noise ratio remained below values found for adatoms with stronger coupling to the substrate. [264] Our calculations show that electrons which tunnel out of the Cs-induced resonance have a high probability for exciting vibrations of the adatom perpendicular to the surface, suggesting a strong resonance-induced adsorbate diffusion, similarly to what has been observed for tip-assisted translations of Li atoms adsorbed on Ag(100). [285]

Our calculations predict that the localized resonance persists at very low coverages, in the few 10^{-3} ML range, before the resonances located on the individual Cs adsorbates overlap. It is remarkable that in the experiments [see Fig. 8.12] the resonance survives in a coverage range where a different regime may be expected: resonances on different adatoms should start to overlap [Fig. 8.17] leading to their delocalization and in that case, the resonance cannot be considered as a result of the surface state localization by an attractive impurity.

Focusing on the initial question, the static local density of states in Fig. 8.16 takes into account the resonance decay by both elastic ($\Gamma_{\mathrm{RCT}} \approx 3.1\,\mathrm{meV}$) and inelastic processes ($\Gamma_{\mathrm{inel}} = 6.0\,\mathrm{meV}$). The total decay rate of the excited state is then obtained as the sum of the decay rates

$$\Gamma_{\mathrm{inel}} + \Gamma_{\mathrm{RCT}} = 9.1\,\mathrm{meV}. \tag{8.26}$$

For Γ_{inel}, we assume that an excited hole in the Cs-induced resonance is subject to inelastic scattering similar to the Ag(111) Shockley-type surface state. Thus we use the same decay

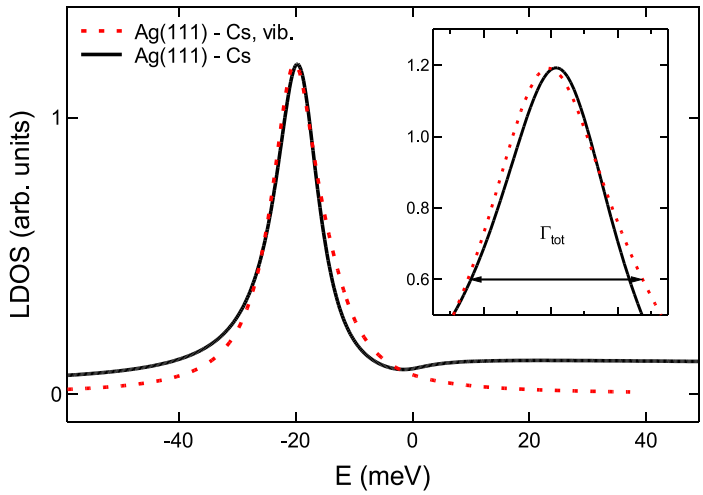

Figure 8.18.: Calculated local density of states (LDOS) of the Cs-induced resonance as a function of energy, E (static adsorbate, black). The resonance maximum is located $\approx 20\,\text{meV}$ below the surface state onset which is set to 0 V. The linewidth of the resonance (static adsorbate) is 9.1 meV. The red dashed line shows the resonance profile with the adsorbate vibration taken into account ($\Gamma_{\text{tot}} \approx 10.5\,\text{meV}$). Inset: Close-up view to show the different widths of the resonance profiles.

rate as observed for the surface state [283, 288, 289] as an input for our calculations. This choice is supported by the above mentioned similarity between the localized state and the surface state band. However, the experimental total width of the resonance is found to be $(12.0 \pm 2.0)\,\text{meV}$, which is larger than the calculated one. This finding indicates an extra source of broadening, which can perhaps be explained by the evolution of the system in the quasi-stationary state.

Adsorbate vibration perpendicular to the surface

For an understanding of the evolution of the system in this quasi-stationary state, the system was treated within the Local Complex Potential (LCP) approximation. In this approximation a complex-valued effective potential is used, which is characterized by the energy and the decay width of the electronic resonance. To this end the LCP is given by the energy and width computed above as a function of adsorbate-surface distance Z. The time evolution of the adsorbate in this LCP was studied in a one-dimensional (1D) wave-packet calculation. It describes how the adsorbate vibrates when brought into the excited electronic state. This approach has recently been developed in the context of the resonant photo-desorption process; [279] it is similar to the time-dependent treatment of resonant vibrational excitation in electron-molecule collisions. [280] From the analysis of the time dependence of the 1D wave packet, it is possible to extract inelastic transitions induced by the electronic excitation as well as the energy profile of the vibrating resonance for an adsorbate initially in the ground vibrational state.

As a result it was found, that the localized state also broadens due to the adsorbate zero-point motion perpendicular to the surface. The corresponding Franck-Condon width amounts to $\Gamma_{\text{vib}} = 5.4\,\text{meV}$. The total width of the resonances was evaluated from the

Γ	Γ_0	Γ_{inel}	Γ_{RCT}	Γ_{vib}	Γ_{tot}
13.1 ± 2.0	12.0 ± 2.0	6.0	3.1	5.4	10.5

Table 8.2.: Experimental and theoretical linewidths (in meV) of the Cs-induced localized resonance ($1\,\mathrm{eV} = \hbar \cdot 1.52 \times 10^{15}\,\mathrm{s}^{-1}$). Γ denotes the full width at half maximum (FWHM) of the resonance measured in spectra of $\mathrm{d}I/\mathrm{d}V$, while Γ_0 is the intrinsic FWHM without thermal and instrumental broadening. Γ_{inel} and Γ_{RCT} are the resonance decay rates due to inelastic processes and resonant charge transfer, while Γ_{vib} is the calculated Franck-Condon width of the resonance due to zero point vibration of the adsorbate perpendicular to the surface. Γ_{tot} is the total theoretical linewidth obtained for a vibrating adsorbate.

resonance profile for the adsorbate vibrating perpendicular to the surface, obtained in an additional quantal calculation including the electron-vibration coupling. The obtained local density of states is shown in Fig. 8.16. Therein the static LDOS (black line) is compared to the resonance profile, which takes the adsorbate vibration into account. The resulting total width for a single adsorbate is $\Gamma_{\mathrm{tot}} = 10.5\,\mathrm{meV}$, which is in better agreement with the experimentally measured width, than considering elastic and inelastic processes alone. A summary of the theoretical and experimental analysis of the linewidth of the Cs-induced resonance is presented in Table 8.2.

Vibrational heating of the Cs adatom induced by inelastically tunneling electrons has been considered. Using the LCP treatment of the vibrating adsorbate, we could evaluate the probability for vibrational excitation induced by the electron injection into the resonance. Based on a Cs vibration decay time of 1.5 ps, which was reported for Pd(111)-Cs, [290] we find a negligible effect of vibrational heating for the presently considered STM current.

8.4. Conclusion

To summarize, Cesium films adsorbed on Ag(111) with submonolayer coverage have been investigated. The resulting adsorbate arrangements were modeled by kinetic Monte Carlo simulations. At very low coverages, a long-range hexagonal order of the superstructure does not exist while at higher coverages a stable and hexagonally ordered adsorbate lattice was observed. Modeling of the adsorbate arrangement at very low coverages have been demonstrated the importance of both dipole-dipole repulsion and surface state-mediated interaction between Cs adatoms. Long-range hexagonal order was inhibited if the coverages are lower than critical coverages, which lead to a disorder-to-order transition. At higher coverages, the dipole-dipole repulsion between the Cs adatoms becomes large enough to stabilize hexagonal superlattices. While commensurate adsorption phases were characterized by a homogeneous adsorbate films, incommensurate phases exhibit domain-like patterns. The experimentally observed rotation of commensurate adsorbate lattices was modeled by our calculations.

From a spectroscopic analysis using scanning tunneling spectroscopy as well as theoretical descriptions, in terms of an extended Newns-Anderson model and theoretical modeling using the wave-packet approach, Cs atoms could be found to localize the two-dimensional surface state continuum at the adsorbate site. A detailed analysis of the linewidth of this occupied resonance have been shown that it can be quantitatively accounted by inelas-

tic scattering processes, resonant charge transfer, and vibrations of the adsorbate. The electron-adsorbate vibration coupling associated with the localized resonance split from the surface state continuum provides a new scheme for STM-induced adsorbate excitation.

Appendix A.

Acknowledgments

My gratitude is debt to those who have helped along the way and supported the approach to a consolidated knowledge of physical concepts presented in this thesis.

In particular, I wish to express my gratitude to my supervisor, Professor Richard Berndt for his encouragement and invaluable suggestions during this work. In this I would also like to include my gratitude to my co-supervisor Dr. Jörg Kröger whose door was always open for discussions in an atmosphere which allowed me to find my own ideas. Moreover, his suggestions, inspiration, and background had a major influence on this thesis.

I would also like to thank Prof. Michael Bonitz and Dr. Alexei Filinov for the provided assistance in computational science and programming.

Furthermore I thank all my colleagues that have provided the environment for sharing their experiences and assistance during the last years. In particular, I wish to express my gratitude to Dr. Nicolas Néel for his extremely valuable experiences, support, insights, and french lessons.

Finally, I want to thank my family. Especially, I dearly thank Hannah for her continued encouragement and support during the entire time, whose love and aid made this entire endeavor worthwhile. A special thought is devoted to my parents for a never-ending support.

This work was supported by the DFG through SFB 668, which is gratefully acknowledged.

Appendix B.

Curriculum vitae

Martin Ziegler
* January 24, 1980 in Bad Soden am Taunus (Germany)

Education

- **1999/03:** Abitur at the Heinrich-Böll-Schule (Hattersheim am Main)
- **2000/04-2002/08:** Study of physics at the Technische Universität Darmstadt
- **2002/09-2003/07:** Study of physics at the Université Bordeaux I
- **2003/09-2006/01:** Study of physics at the Universität Kiel

  Diploma thesis: *Vacuum Alignment in Little-Higgs Modellen*
  in the group of Prof. B. Schrempp

Professional experience

- **since 2006/03:** Research and teaching assistant
  in the group of Prof. R. Berndt, *IEAP Universität Kiel*

List of publications during this thesis

- M. Ziegler, J. Kröger, R. Berndt, A. Filinov, and M. Bonitz,
  Scanning tunneling microscopy and kinetic Monte-Carlo investigation of Cesium superlattices on Ag(111),
  Phys. Rev. B **78**, 245427 (2008).
- M. Ziegler, J. Kröger, R. Berndt, A. G. Borisov, and J. P. Gauyacq,
  Linewidth of a Cesium Adatom Resonance on Ag(111),
  Phys. Rev. B **79**, 075401 (2009).
- M. Ziegler, N. Néel, A. Sperl, J. Kröger, and R. Berndt,
  Local density of states from constant-current tunneling spectra,
  Phys. Rev. B **80**, 125402 (2009).
- N. Néel, J. Kröger, M. Ziegler, and R. Berndt,
  Electronic structure modification of magnetic clusters,
  submitted to Phys. Rev. B.

Teaching experience

- Teaching assistant: Experimental exercises (Neben- und Hauptfach Praktikum Physik)

Languages

- German (mother tongue), English (fluent), French (fluent)

Appendix C.

Eidesstattliche Erklärung

Hiermit erkläre ich an Eides Statt, dass ich diese Arbeit selbständig unter der Beratung meiner wissenschaftlichen Lehrer und nur mit den angegebenen Hilfsmitteln erstellt habe. Diese Arbeit wurde weder ganz noch in Teilen an anderer Stelle im Rahmen eines Prüfungsverfahrens vorgelegt. Frühere Promotionsversuche wurden von mir nicht vorgenommen.

Kiel, den

Bibliography

[1] M. N. Baibich, J. M. Broto, A. Fert, F. Nguyen Van Dau, F. Petroff, P. Etienne, G. Creuzet, A Friederich, and J. Chazelas, Phys. Rev. Lett. **61**, 2472 (1988).

[2] G. Binash, P. Grünberg, F. Saurenbach, and W. Zinn, Phys. Rev. B **39**, 4828 (1989).

[3] N. Agraït, A. L. Yeyati, and J. M. van Ruitenbeek, Phys. Rep. **377**, 81 (2007).

[4] B. Doudin and M. Viret, J. Phys.: Condens. Matter **20**, 083201 (2008).

[5] H. P. Bonzel, A. M. Bradshaw, and G. Ertl (Eds.), *Physics and chemistry of alkali metal adsorption* (Elsevier, Amsterdam, 1989).

[6] G. Binnig, H. Rohrer, Ch. Gerber, and E. Weibel, Appl. Phys. Lett. **40**, 178 (1982); Phys. Rev. Lett. **49**, 57 (1982); Physica **109/110B**, 2075 (1982); G. Binnig and H. Rohrer, Helv. Phys. Acta **55**, 726 (1982).

[7] M. F. Crommie, C. P. Lutz, and D. M. Eigler, Nature **363**, 524 (1993).

[8] Y. Hasegawa and Ph. Avouris, Phys. Rev. Lett. **71**, 1071 (1993).

[9] J. Li, W.-D. Schneider, R. Berndt, O. R. Bryant, and S. Crampin, Phys. Rev. Lett. **81**, 4464 (1998).

[10] X. Lu, M. Grobis, K. H. Khoo, S. G. Louie, and M. F. Crommie, Phys. Rev. Lett. **90**, 096802 (2003).

[11] R. Wiesendanger, H. J. Güntherodt, R. J. Gambino, and R. Ruf, Phys. Lett. Lett **65**, 247 (1990).

[12] P. M. Tedrow and R. Meservey Phys. Rev. Lett. **26**, 192 (1971).

[13] M. Julliere, Phys. Lett. A **54**, 225 (1975).

[14] A. J. Heinrich, J. A. Gupta, C. P. Lutz, D. M. Eigler, Science **306**, 466 (2004).

[15] C. F. Hirjibehedin, C. P. Lutz, and A. J. Heinrich, Science **312**, 1021 (2006).

[16] B. C. Stipe, M. A. Rezaei, and W. Ho, Science **280**, 1732 (1998).

[17] L. J. Lauhon and W. Ho, Phys. Rev. Lett. **85**, 4566 (2000).

[18] N. Lorente and M. Persson, Phys. Rev. Lett. **85**, 2997 (2000).

[19] N. Lorente, M. Persson, L. J. Lauhon, and W. Ho, Phys. Rev. Lett. **86**, 2593 (2001).

[20] I. Giaver, Phys. Rev. Lett. **5**, 147 (1960); **5**, 464 (1960).

[21] J. Tersoff and D. R. Hamann, Phys. Rev. Lett. **50**, 1998 (1983); Phys. Rev. B **31**, 805 (1985).

[22] A. Selloni, P. Carnevali, E. Tosatti, and C. D. Chen, Phys. Rev. B **31**, 2602 (1985).

[23] J. A. Stroscio, R. M. Feenstra, and A. P. Fein, Phys. Rev. Lett. **57**, 2579 (1986).

[24] N. D. Lang, Phys. Rev. B **34**, 5947 (1986).

[25] N. D. Lang, Phys. Rev. Lett. **56**, 1164 (1986).

[26] V. A. Ukraintsev, Phys. Rev. B **53**, 11176 (1996).

[27] B. Koslowski, C. Dietrich, A. Tschetschetkin, and P. Ziemann, Phys. Rev. B **75**, 035421 (2007).

[28] M. Passoni, F. Donati, A. Li Bassi, C. S. Casari, and C. E. Bottani, Phys. Rev. B **79**, 045404 (2009).

[29] D. B. Dougherty, P. Maksymovych, J. Lee, and J. T. Yates, Jr., Phys. Rev. Lett. **97**, 236806 (2006).

[30] H.-C. Ploigt, C. Brun, M. Pivetta, F. Patthey, and W.-D. Schneider, Phys. Rev. B **76**, 195404 (2007).

[31] M. Feng, J. Zhao, and H. Petek, Science **320**, 359 (2008).

[32] S. F. Alvarado, P. F. Seidler, D. G. Lidzey, and D. D. C. Bradley, Phys. Rev. Lett. **81**, 1082 (1998).

[33] J. Li, W.-D. Schneider, and R. Berndt, Phys. Rev. B **56**, 7656 (1997).

[34] L. Limot, J. Kröger, R. Berndt, A. Garcia-Lekue, and W. A. Hofer, Phys. Rev. Lett. **94**, 126102 (2005).

[35] J. G. Simmons, J. Appl. Phys. **34**, 1793 (1963).

[36] J. Bardeen, Phys. Rev. Lett. **6**, 57 (1961).

[37] C.J. Chen, Mod. Phys. Lett. B **5**, 107 (1991).

[38] C. B. Duke, *Tunneling in Solids* (Academic, New York, 1969).

[39] R. J. Hamers, in *Scanning Probe Microscopy and Spectroscopy. Theory, Techniques and Applications*, edited by Dawn A. Bonnell (VCH, New York, 1993).

[40] X. Lu, M. Grobis, K. H. Khoo, S. G. Louie, and M. F. Crommie, Phys. Rev. B **70**, 115418 (2004).

[41] G. Schull, N. Néel, M. Becker, J. Kröger, and R. Berndt, New J. Phys. **10**, 065012 (2008).

[42] L. Limot, T. Maroutian, P. Johansson, and R. Berndt, Phys. Rev. Lett. **91**, 196801 (2003).

[43] J. Kröger, L. Limot, H. Jensen, R. Berndt, and P. Johansson, Phys. Rev. B **70**, 033401 (2004).

[44] J. Kröger, L. Limot, H. Jensen, R. Berndt, S. Crampin, and E. Pehlke, Prog. Surf. Sci. **80**, 26 (2005).

[45] J. Li, W.-D. Schneider, R. Berndt, O. R. Bryant, and S. Crampin, Phys. Rev. Lett. **81**, 4464 (1998).

[46] A. Schäfer, I. L. Shumay, M. Wiets, M. Weinelt, Th. Fauster, E. V. Chulkov, V. M. Silkin, and P. M. Echenique, Phys. Rev. B **61**, 13159 (2000).

[47] J.A Stroscio and R.M. Feenstra, in *Scanning Tunneling Microscopy*, edited by J.A Stroscio and W.J. Kaiser, *Methods of Experimental Physics*, Vol. 27 (Academic Press, New York, 1993)

[48] J. A. Stroscio, R. M. Feenstra, D. M. Newns, and A. P. Fein, J. Vac. Sci. Technol. **A 6**, 499 (1988).

[49] Th. Berghaus, A. Brodde, H. Neddermeyer, and St. Tosch, Surf. Sci. **193**, 235 (1988).

[50] A. Sperl, J. Kröger, N. Néel, H. Jensen, R. Berndt, A. Franke, and E. Pehlke, Phys. Rev. B **77**, 085422 (2008).

[51] G. Binnig, K. H. Frank, H. Fuchs, N. Garcia, B. Reihl, H. Rohrer, F. Salvan, and A. R. Williams, Phys. Rev. Lett. **55**, 991 (1985).

[52] R. S. Becker, J. A. Golovchenko, and B. S. Swartzentruber, Phys. Rev. Lett. **55**, 987 (1985).

[53] A. Sperl, J. Kröger, R. Berndt, A. Franke, and E. Pehlke, submitted.

[54] A. Franke and E. Pehlke, private communication. For calculations of constant-distance data the tip was placed 0.4 – 0.6 nm above the dimer and the distances between the maxima varied between 0.45 and 0.48 nm. The current was calculated in a Tersoff-Hamann approach. [21] The electronic structure of the silver dimer has been calculated using density functional methods described in Ref. [50].

[55] G. Hörmandinger, Phys. Rev. Lett. **73**, 910 (1994); Phys. Rev. B **49**, 13897 (1994).

[56] S. Crampin, J. Kröger, H. Jensen, and R. Berndt, Phys. Rev. Lett. **95**, 029701 (2005).

[57] J. Li, W.-D. Schneider, R. Berndt, and S. Crampin, Phys. Rev. Lett. **80**, 3332 (1998).

[58] J. Kliewer, R. Berndt, and S. Crampin, Phys. Rev. Lett. **85**, 4936 (2000).

[59] H. Jensen, J. Kröger, R. Berndt, and S. Crampin, Phys. Rev. B **71**, 155417 (2005).

[60] S. Crampin, H. Jensen, J. Kröger, L. Limot, and R. Berndt, Phys. Rev. B **72**, 035443 (2005).

[61] S. AA. Lindgren and L. Walldén, Phys. Rev. B **22**, 5967 (1980).

[62] H. P. Bonzel, Surf. Sci. Rep. **8**, 43 (1988).

[63] J. Kröger, D. Bruchmann, S. Lehwald, and H. Ibach, Surf. Sci. **449**, 227 (2000).

[64] N. Néel, J. Kröger, L. Limot, T. Frederiksen, M. Brandbyge, and R. Berndt, Phys. Rev. Lett. **98**, 065502 (2007).

[65] J. Klein, A. Léger, M. Belin, and D. Défourneau, Phys. Rev. B **7**, 2336 (1973).

[66] J. Kröger, N. Néel, and L. Limot, J. Phys.: Condens. Matter **20**, 223001 (2008).

[67] R. Landauer, IBM J. Res. Dev. **1**, 223 (1957).

[68] M. Büttiker, IBM J. Res. Dev. **32**, 63 (1988).

[69] M. Brandbyge, and K. W. Jacobsen, NATO Advanced Studies Institute, Series E: Applied Sciences **340** (1997).

[70] N. Néel, J. Kröger, R. Berndt, and E. Pehlke, Phys. Rev. B **78**, 233402 (2008).

[71] D. T. Pierce, Phys. Scr. **38**, 291 (1988).

[72] S. F. Alvarado and P. Renaud, Phys. Lett. Lett **68**, 1387 (1992).

[73] E. C. Stoner, Proc. R. Soc. Lond. A **169**, 339 (1939).

[74] M. B. Stearns, J. Mag. Mag. Mat. **5**, 167 (1977).

[75] J. C. Slonczewski, Phys. Rev. B **39**, 6995 (1989).

[76] A. M. Bratkovsky, Phys. Rev. B **56**, 2344 (1997).

[77] M Bode Rep. Prog. Phys. **66**, 523 (2003).

[78] D. Wortmann, S. Heinze, Ph. Kurz, G. Bihlmayer, and S. Blügel, Phys. Rev. Lett. **86**, 4132 (2001).

[79] S. Blügel, D. Pescia, and P. H. Dederichs Phys. Rev. B **39**, 1392 (1989).

[80] M. Bode, M. Getzlaff, and R. Wiesendanger, Phys. Rev. Lett. **81**, 4256 (1998).

[81] R. Wiesendanger, D. Bürgler, G. Tarrach, T. Schaub, U. Hartmann, H. J. Güntherodt, I. V. Shvets, and J. M. D. Coey, Appl. Phys. A **53**, 349 (1991).

[82] A. Wadas and H. J. Hug, J. Appl. phys. **72**, 203 (1992).

[83] A. Kubetzka, M. Bode, O. Pietzsch, and R. Wiesendanger, Phys. Rev. Lett. 88, 057201 (2002).

[84] H. Jensen, Diploma thesis, Christian-Albrechts Universität zu Kiel (2003)

[85] T. v Hofe, PhD thesis, Christian-Albrechts Universität zu Kiel (2006)

[86] www.oaresearch.co.uk

[87] M. Bode, S. Krause, L. Berbil-Bautista, S. Heinze and R. Wiesendanger, Surf. Sci. **601**, 3308 (2007).

[88] H. Bethge, D. Heuer, Ch. Jensen, K. Reshöft, and U. Gradmann, Surf. Sci. **331**, 878 (1995).

[89] J. Hauschild, U. Gradmann, and H. J. Elmers, Appl. Phys. Lett. **72**, 3211 (1998).

[90] N. Weber, K. Wagner, H. J. Elmers, J. Hauschild, and U. Gradmann, Phys. Rev. B **55**, 14121 (1997).

[91] H. J. Elmers, J. Hauschild, H. Fritzsche, G. Liu, U. Gradmann, and U. Köhler, Phys. Rev. Lett. **75**, 2031 (1995).

[92] A. Kubetzka, O. Pietzsch, M. Bode, and R. Wiesendanger, Phys. Rev. B **63**, 140407 (2001)

[93] M. Bode, S. Heinze, A. Kubetzka, O. Pietzsch, X. Nie, G. Bihlmayer, S. Blügel, and R. Wiesendanger, Phys. Rev. Lett. 89, 237205 (2002)

[94] A. Hubert and R. Schäfer, *Magnetic Domains* (Springer, Berlin, 1998)

[95] S. N. Okuno, T. Kishi, and K. Tanaka, Phys. Rev. Lett. 88, 066803 (2002).

[96] T. K. Yamada, M. M. J. Bischoff, G. M. M. Heijnen, T. Mizoguchi, and H. van Kempen, Phys. Rev. Lett. 90, 056803 (2003).

[97] T. K. Yamada, M. M. J. Bischoff, T. Mizoguchi, and H. van Kempen, Appl. Phys. Lett. 82, 1437 (2003).

[98] L. Berbil-Bautista, S. Krause, M. Bode, and R. Wiesendanger, Phys. Rev. B 76, 064411 (2007).

[99] A. Cottet, T. Kontos, S. Sahoo, H. T. Man, W. Belzig, C. Bruder, and C. Schönenberger, Semicond. Sci. Technol. **21**, 578 (2006).

[100] L. E. Hueso, J. M. Pruneda, V. Ferrari, G. Brunell, J. P. Valdes-Herrera, B. D. Simmons, P. B. Littlewood, E. Artacho, A. Fert, and N. D. Mathur, Nature **445**, 410 (2007).

[101] G. Tatara, Y.-W. Zhao, M. Muñoz, and N. García, Phys. Rev. Lett. **83**, 2030 (1999).

[102] C. Untiedt, D. M. T. Dekker, D. Djukic, and J. M. van Ruitenbeek, Phys. Rev. B **69**, 081401 (2004).

[103] P. Grünberg, Rev. Mod. Phys., **80**, 1531 (2008).

[104] P. M. Levy, in *Solid State Physics*, edited by H. Ehrenreich and D. Turnbull (Cambridge, Academic, 1994), Vol. 47, p. 367.

[105] A. Barthélémy, A. Fert, and F. Petroff, in it Handbook of Ferromagnetic Materials, edited by K. H. J. Bushow (Amsterdam, Elsevier Science, 1999), Vol. 12, Chap. 1.

[106] E. Y. Tsymbal and D. G. Pettifor, in *Solid State Physics*, edited by H. Ehrenreich and F. Spaepen (Cambridge, Academic, 2001), Vol. 56, p. 113.

[107] N. García, M. Muñoz, and Y.-W. Zhao, Phys. Rev. Lett. **82**, 2923 (1999).

[108] N. García, H. Rohrer, I. G. Savelief, and Y.-W. Zhao, Phys. Rev. Lett. **85**, 3053 (2000).

[109] H. D. Chopra and S. Z. Hua, Phys. Rev. B **66**, 020403 (2002).

[110] S. Z. Hua and H. D. Chopra, Phys. Rev. B **67**, 060401 (2003).

[111] H. D. Chopra, M. R. Sullivan, J. N. Armstrong, and S. Z. Hua, Nature Mater. **4**, 832 (2005).

[112] G. Brumfiel, Nature **426**, 110 (2003).

[113] W. F. Egelhoff, Jr., L. Gan, H. Ettedgui, Y. Kadmon, C. J. Powell, P. J. Chen, A. J. Shapiro, R. D. McMichael, J. J. Mallett, T. P. Moffat, M. D. Stiles, and E. B. Svedberg, J. Appl. Phys. **95**, 7554 (2004).

[114] J. Velev, R. Sabirianov, S. S. Jaswal, and E. Y. Tsymbal, Phys. Rev. Lett. **94**, 127203 (2005).

[115] K. I. Bolotin, F. Kuemmeth, and D. C. Ralph, Phys. Rev. Lett. **97**, 127202 (2006).

[116] M. Viret, M. Gabureac, F. Ott, C. Fermon, C. Barreteau, G. Autes, and R. Guirado-Lopez, Eur. Phys. J. B **51**, 1 (2006).

[117] A. Sokolov, C. Zhang, E. Y. Tsymbal, J. Redepenning, and B. Doudin, Nature Nanotechnol. **2**, 171 (2007).

[118] S.-F. Shi and D. C. Ralph, Nature Nanotechnol. **2**, 522 (2007).

[119] G. Autès, C. Barreteau, M.-C. Desjonquères, D. Spanjaard, and M. Viret, EPL **83**, 17010 (2008).

[120] M. Häfner, J. K. Viljas, and J. C. Cuevas, Phys. Rev. Lett. **79**, 140410 (2009).

[121] N. Néel, J. Kröger, and R. Berndt, Phys. Rev. Lett. **102**, 086805 (2009).

[122] Y. Yayon, X. Lu, and M. F. Crommie, Phys. Rev. B **73**, 155401 (2006).

[123] Y. Yayon, V. W. Brar, L. Senapati, S. C. Erwin, and M. F. Crommie, Phys. Rev. Lett. **99**, 067202 (2007).

[124] R. Schmidt, C. Lazo, H. Hölscher, U. H. Pi, V. Caciuc, A. Schwarz, R. Wiesendanger, and S. Heinze, Nano Lett. **9**, 200 (2009).

[125] B. W. Heinrich, C. Iacovita, M. V. Rastei, L. Limot, and J. P. Bucher, Phys. Rev. B **79**, 113401 (2009).

[126] J. C. Cuevas, private communication.

[127] E. Zaremba, I. Nagy, and P. M. Echenique, Phys. Rev. Lett. **90**, 046801 (2003).

[128] F. E. Olsson, M. Persson, A. G. Borisov, J.-P. Gauyacq, J. Lagoute, and S. Fölsch, Phys. Rev. Lett. **93**, 206803 (2004).

[129] V. Madhavan, W. Chen, T. Jamneala, M. F. Crommie, and N. S. Wingreen, Science **280**, 567 (1998).

[130] J. Lambe and R. C. Jaklevic, Phys. Rev. **165**, 821 (1968).

[131] J. Lambe and R. C. Jaklevic, Phys. Rev. Lett. **17**, 1139 (1966).

[132] L. J. Lauhon and W. Ho, Phys. Rev. B **60**, R8525 (1999).

[133] J. R. Hahn, H. J. Lee, and W. Ho, Phys. Rev. Lett. **85**, 1914 (2000).

[134] L. J. Lauhon and W. Ho, J. Chem. Phys. A **104**, 2463 (2004).

[135] J. I. Pascual, J. J. Jackiw, Z. Song, P. S. Weiss, H. Conrad, and H.-P. Rust, Phys. Rev. Lett. **86**, 1050 (2001).

[136] Y. Kim, T. Komeda, and M. Kawai, Phys. Rev. Lett. **89**, 126104 (2002).

[137] N. A. Pradhan, N. Liu, and W. Ho, J. Phys. Chem. B **109**, 8513 (2005).

[138] D. J. Scalapino and S. M. Marcus, Phys. Rev. Lett. **18**, 459 (1967).

[139] J. A. Gupta, C. P. Lutz, A. J. Heinrich, and D. M. Eigler, Phys. Rev. B **18**, 115416 (2005).

[140] J. Kirtley and P. Soven, Phys. Rev. B **19**, 1812 (1979).

[141] J. Kondo, Prog. Theor. Phys. **32**, 37 (1964).

[142] A.C. Hewson, *The Kondo problem to heavy fermions*, Cambridge University Press (1993).

[143] M. Ternes, A. J. Heinrich, and W.-D. Schneider, J. Phys.: Condens. Matter **21**, 053001 (2009.)

[144] P. W. Anderson, Phys. Rev. **124**, 41 (1961).

[145] J. T. Li, W.-D. Schneider, R. Berndt, and B. Delley, Phys. Rev. Lett. **80**, 2893 (1998).

[146] Y. Kuk, P. J. Silverman, and F. M. Chua, J. Microscopy **152**, 449 (1988).

[147] J. K. Gimzewski, R. Berndt, and R. R. Schlittler, Surf. Sci. **247**, 327 (1991).

[148] R. Koch, M. Borbonus, O. Haase, and K. H. Rieder, Appl. Phys. A **55**, 417 (1992).

[149] U. Fano, Phys. Rev. **124**, 1866 (1961).

[150] V. Madhavan, W. Chen, T. Jamneala, and M. F. Crommie, Phys. Rev. B **64**, 165412 (2001).

[151] N. Knorr, M. A. Schneider, L. Diekhöner, P. Wahl, and K. Kern, Phys. Rev. Lett. **88**, 096804 (2002).

[152] T. Balashov, T. Schuh, A. F. Takács, A. Ernst, S. Ostanin, J. Henk, I. Mertig, P. Bruno, T. Miyamachi, S. Suya, and W. Wulfhekel, Phys. Rev. Lett. **102**, 257203 (2009).

[153] K. Tao, V. S. Stepanyuk, W. Hergert, I.Rungger, S. Sanvito, and P.Bruno, Phys. Rev. Lett. **103**, 057202 (2009).

[154] K. Liu and S. Gao, Phys. Rev. Lett. **95**, 226102 (2005).

[155] K. Liu and S. Gao, Phys. Rev. B **74**, 195433 (2006).

[156] J. Konig, H. Schoeller, and G. Schon, Phys. Rev. Lett. **76**, 1715 (1996).

[157] J. Paaske and K. Flensberg, Phys. Rev. Lett. **94**, 176801 (2005).

[158] Z. Chen, H. Lu, R. Lü, and B. Zhu, J. Phys. Condens. Matter **18**, 5435 (2006).

[159] L. H. Yu, Z. K. Keane, J. W. Ciszek, L. Cheng, M. P. Stewart, J. M. Tour, and D. Natelson, Phys. Rev. Lett. **93**, 266802 (2004).

[160] I. Fernández-Torrente, K. J. Franke, and J. I. Pascual, Phys. Rev. Lett. **101**, 217203 (2008).

[161] A.F. Voter *Introduction to the Kinetic Monte Carlo Method* (Springer, NATO Publishing Unit, Dordrecht, 2005).

[162] N. Metropolis, A.W. Rosenbluth, M.N. Rosenbluth, A.H. Teller, E. Teller J. Chem. Phys. **21**, 1087 (1953).

[163] D. R. Cox and H. D. Miller, *The Theory of Stochastic Processes* (Methuen, London, 1965).

[164] W. M. Young and E. W. Elcock, Proc. Phys. Soc. **89**, 735 (1966).

[165] A.B. Bortz and M.H. Kalos and J.L. Lebowitz, J. Comp. Phys. **17** (1975).

[166] A.F. Voter Phys. Rev. B **34**, 6819 (1986).

[167] K. A. Fichthorn and W. H. Weinberg, J. Chem. Phys. **95**, 1090 (1991).

[168] K. A. Fichthorn and M. Scheffler, Phys. Rev. Lett. **84**, 5371 (2000).

[169] P. A. Maksym Senicond. Sci. Technol. **3**, 594 (1988)

[170] T.P. Schulze Phys. Rev. E **65**, 036704 (2002).

[171] J.C. Slater, and G.F. Koster, Phys. Rev. **94**, 1498 (1954).

[172] R.P. Gupta, Phys. Rev. B **23**, 6265 (1985).

[173] D. Tomànek, A.A. Aligia, and C.A. Balseiro Phys. Rev. B **32**, 5051 (1985).

[174] F. Cyrot-Lackmann, M.C. Desjonquères, and J.P. Gaspard, J. Phys. C.: Solid State Phys. **7**, 925 (1974).

[175] F. Cleri, and V. Rosato Phys. Rev. B **48**, 22 (1993).

[176] F. Montalenti, and R. Ferrando Phys. Rev. B **58**, 3617 (1998).

[177] J. I. Martın, J. Nogués, K. Liu, J. L. Vicent, I. K. Schuller, J. Magn. Magn. Mater. **256**, 449 (2003).

[178] D. M. Eigler, E. K. Schweizer, Nature (London) **344** (1990) 524.

[179] P. Gambardella, M. Blanc, H. Brune, K. Kuhnke, K. Kern, Phys. Rev. B **61** (2000) 2254.

[180] J.-L. Lin, D. Y. Petrovykh, A. Kirakosian, H. Rauscher, F. J. Himpsel, Appl. Phys. Lett. **78** (2001) 829.

[181] V. Repain, G. Baudot, H. Ellmer, S. Rousset, Europhys. Lett. **58** (2002) 730.

[182] N. Néel, J. Kröger, R. Berndt, Adv. Mater. **18** (2006) 174.

[183] N. Néel, J. Kröger, R. Berndt, Appl. Phys. Lett. **88** (2006) 163101.

[184] J. Kröger, N. Néel, R. Berndt, R. Rurali, N. Lorente, J. Phys.: Condens. Matter **18** (2006) S51.

[185] J. Kröger, H. Jensen, N. Néel, R. Berndt, to be published.

[186] U. Harten, A. M. Lahee, J. P. Toennies, Ch. Wöll, Phys. Rev. Lett. **54** (1985) 2619.

[187] Ch. Wöll, S. Chiang, R. J. Wilson, P. H. Lippel, Phys. Rev. B **39** (1989) 7988.

[188] J. V. Barth, H. Brune, G. Ertl, R. J. Behm, Phys. Rev. B **42** (1990) 9307.

[189] B. Voigtländer, G. Meyer, N. M. Amer, Phys. Rev. B **44** (1991) 10354.

[190] S. Padovani, I. Chado, F. Scheurer, J. P. Bucher, Phys. Rev. B **59** (1999) 11887.

[191] R. Koch, M. Borbonus, O. Haase, K.-H. Rieder, Appl. Phys. A **55** (1992) 417.

[192] M. B. Hugenschmidt, A. Hitzke, R. J. Behm, Phys. Rev. Lett. **76** (1996) 2535.

[193] S. Padovani, F. Scheurer, J. P. Bucher, Europhys. Lett. **45** (1999) 327.

[194] G. Binnig, H. Rohrer, Ch. Gerber, E. Weibel, Surf. Sci. **131** (1983) L379.

[195] C. Massobrio, F. Patthey, H.-V. Roy, W. D. Schneider, Phys. Rev. B **52** (1995) 2063.

[196] H.-V. Roy, P. Fayet, F. Patthey, W. D. Schneider, B. Delley, C. Massobrio, Phys. Rev. B **49** (1994) 5611.

[197] L. P. Nielsen, F. Besenbacher, I. Stensgaard, E. Lægsgaard, C. Engdahl, P. Stoltze, K. W. Jacobsen, J. K. Nørskov, Phys. Rev. Lett. **71** (1993) 754.

[198] V. S. Stepanyuk, W. Hergert, Phys. Rev. B **62** (2000) 7542.

[199] C. Goyhenex, and H. Bulou, Phys. Rev. B **63** 235404 (2001).

[200] N. A. Levanov, V. S. Stepanyuk, W. Hergert, D. I. Bazhanov, P. H. Dietrichs, A. Ktsnelson, and C. Massobrio Phys. Rev. B **61** 2230 (2000).

[201] O. V. Stepanyuk, N. N. Negulyaev, A. M. Saletsky, and W. Hergert, Phys. Rev. B **78** 113406 (2008).

[202] H. Bulou and J. P. Bucher, Phys. Rev. Lett. **96** 076102 (2006).

[203] G.Ł. Kellog, Phys. Rev. Lett. **76** 98 (1996).

[204] R. D. Diehl and R. McGrath, Surf. Sci. Rep. **23**, 43 (1996).

[205] R. B. Grant and R. M. Lambert, Langmuir **1**, 29 (1985).

[206] C. T. Campbell, J. Phys. Chem. **89**, 5789 (1985).

[207] G. M. Lamble, R. S. Brookes, D. A. King, and D. Norman, Phys. Rev. Lett. **61**, 1112 (1988).

[208] G. S. Leatherman and R. D. Diehl, Phys. Rev. B **53**, 4939 (1996).

[209] S. Å. Lindgren, L. Walldén, J. Rundgren, P. Westrin, and J. Neve, Phys. Rev. B **28**, 6707 (1983).

[210] W. C. Fan and A. Ignatiev, Phys. Rev. B **37**, 5274 (1988).

[211] Z. Y. Li, K. M. Hock, and R. E. Palmer, Phys. Rev. Lett. **67**, 1562 (1991).

[212] Th. von Hofe, J. Kröger, and R. Berndt, Phys. Rev. B **73**, 245434 (2006).

[213] S.-Å. Lindgren and L. Walldén, Phys. Rev. B **38**, 3060 (1988).

[214] N. Fischer, S. Schuppler, R. Fischer, Th. Fauster, and W. Steinmann, Phys. Rev. B **47**, 4705 (1993).

[215] Th. Fauster and W. Steinmann, in *Electromagnetic Waves: Recent Developments in Research*, edited by P. Halevi, Photonic Probes of Surfaces Vol. 2 (Elsevier, Amsterdam, 1995).

[216] A. Carlsson, B. Hellsing, S.-Å. Lindgren, and L. Walldén, Phys. Rev. B **56** 1593 (1997).

[217] M. Bauer, S. Pawlik, and M. Aeschlimann, Phys. Rev. B **55**, 10040 (1997).

[218] S. Ogawa, H. Nagano, and H. Petek, Phys. Rev. Lett. **82**, 1931 (1999).

[219] B. Hellsing, J. Carlsson, L. Walldén, and S.-Å. Lindgren, Phys. Rev. B **61**, 2343 (2000).

[220] T.-C. Chiang, Surf. Sci. Rep. **39**, 181 (2000).

[221] M. Milun, P. Pervan, and D. P. Woodruff, Rep. Prog. Phys. **65**, 99 (2001).

[222] J. Kliewer and R. Berndt, Phys. Rev. B **65**, 035412 (2002).

[223] A. K. Kazansky, A. G. Borisov, and J. P. Gauyacq, Surf. Sci. **577**, 47 (2005).

[224] C. Corriol, V. M. Silkin, D. Sánchez-Portal, A. Arnau, E. V. Chulkov, P. M. Echenique, T. von Hofe, J. Kliewer, J. Kröger, and R. Berndt, Phys. Rev. Lett. **95**, 176802 (2005).

[225] J. Kröger, L. Limot, H. Jensen, R. Berndt, S. Crampin, and E. Pehlke, Prog. Surf. Sci. **80**, 26 (2005).

[226] J. Koutecký, Trans. Faraday Soc. **54**, 1038 (1958).

[227] T. B. Grimley, Proc. Phys. Soc. (London) **90**, 751 (1967).

[228] D. N. Newns, Phys. Rev. **178**, 1123 (1969).

[229] T. L. Einstein and J. R. Schrieffer, Phys. Rev. B **7**, 3629 (1973).

[230] T. T. Tsong, Phys. Rev. Lett. **31**, 1207 (1973).

[231] K. H. Lau and W. Kohn, Surf. Sci. **75**, 69 (1978).

[232] H. Brune, J. Wintterlin, G. Ertl, and R. J. Behm, Europhys. Lett. **13**, 123 (1990).

[233] M. M. Kamna, S. J. Stranick, and P. S. Weiss, Science **274**, 118 (1996).

[234] E. Wahlström, I. Ekvall, H. Olin, and L. Walldén, Appl. Phys. A **66**, S1107 (1998).

[235] J. Repp, F. Moresco, G. Meyer, K.-H. Rieder, P. Hyldgaard, and M. Persson, Phys. Rev. Lett. **85**, 2981 (2000).

[236] N. Knorr, H. Brune, M. Epple, A. Hirstein, M. A. Schneider, and K. Kern, Phys. Rev. B **65**, 115420 (2002).

[237] F. Silly, M. Pivetta, M. Ternes, F. Patthey, J. P. Pelz, and W.-D. Schneider, Phys. Rev. Lett. **92**, 016101 (2004).

[238] N. N. Negulyaev, V. S. Stepanyuk, L. Niebergall, W. Hergert, H. Fangohr, and P. Bruno, Phys. Rev. B **74**, 035421 (2006).

[239] V. S. Stepanyuk, N. N. Negulyaev, L. Niebergall, R. C. Longo, and P. Bruno, Phys. Rev. Lett. **97**, 186403 (2006).

[240] SAES Getters SpA, Viale Italia 77, 20020 Lainate, Italy (http://www.saesgetters.com).

[241] P. Hyldgaard and M. Persson, J. Phys. Condens. Matter **12**, L13 (2000).

[242] H. P. Bonzel, Surf. Sci. Rep. **8**, 43 (1987).

[243] S.-Å. Lindgren and L. Walldén, Phys. Rev. B **22**, 5967 (1980).

[244] J. Kröger, D. Bruchmann, S. Lehwald, and H. Ibach, Surf. Sci. **449**, 227 (2000).

[245] L. D. Schmidt and R. Gomer, J. Chem. Phys. **45**, 1605 (1966).

[246] M. Breitholz, V. Chis, B. Hellsing, S.-Å. Lindgren, and L. Walldén, Phys. Rev. B **75**, 155403 (2007).

[247] A. Chatterjee and D. G. Vlachos, J. Computer-Aided Mater. Des. **14**, 253 (2007).

[248] G. Voronoï, J. Reine Angew. Math. **133**, 97 (1907).

[249] P. Ludwig, S. Kosse, and M. Bonitz, **71**, 046403 (2005).

[250] P. Hyldgaard and T. L. Einstein, J. Cryst. Growth **275**, e1637 (2005).

[251] J. Repp, PhD Thesis (Freie Universität Berlin, 2002).

[252] K. E. Johnson, R. J. Wilson, and S. Chiang, Phys. Rev. Lett. **71**, 1055 (1993).

[253] S. Marchini, C. Sachs, and J. Wintterlin, Surf. Sci. **592**, 58 (2005).

[254] P. M. Echenique, R. Berndt, E. V. Chulkov, Th. Fauster, A. Goldmann, and U. Höfer, Surf. Sci. Rep. **52**, 219 (2004).

[255] E. V. Chulkov, A. G. Borisov, J. P. Gauyacq, D. Sánchez-Portal, V. M Silkin, V. P. Zhukov, and P. M. Echenique, Chem. Rev. **106**, 4160 (2006).

[256] L. Bürgi, H. Brune, O. Jeandupeux, and K. Kern, J. Electron Spectrosc. Relat. Phenom. **109**, 33 (2000).

[257] H. Jensen, J. Kröger, R. Berndt, and S. Crampin, Phys. Rev. B **71**, 155417 (2005).

[258] S. Crampin, H. Jensen, J. Kröger, L. Limot, and R. Berndt, Phys. Rev. B **72**, 035443 (2005).

[259] S. Crampin, J. Kröger, H. Jensen, and R. Berndt, Phys. Rev. Lett. **95**, 029701 (2005).

[260] Ch. Reuß, I.L. Shumay, U. Thomann, M. Kutschera, M. Weinelt, Th. Fauster, and U. Höfer, Phys. Rev. Lett. **82**, 153 (1999).

[261] K. Boger, M. Weinelt, and Th. Fauster, Phys. Rev. Lett. **92**, 126803 (2004).

[262] F. E. Olsson, A. G. Borisov, M. Persson, N. Lorente, A. K. Kazansky, and J. P. Gauyacq, Phys. Rev. B **70**, 205417 (2004).

[263] F. E. Olsson, M. Persson, A. G. Borisov, J.-P. Gauyacq, J. Lagoute, and S. Fölsch, Phys. Rev. Lett. **93**, 206803 (2004).

[264] L. Limot, E. Pehlke, J. Kröger, and R. Berndt, Phys. Rev. Lett. **94**, 036805 (2005).

[265] V. S. Stepanyuk, A. N. Klavsyuk, L. Niebergall, and P. Bruno, Phys. Rev. B **72**, 153407 (2005).

[266] S. Lounis, P. Mavropoulos, P. H. Dederichs, and S. Blügel, Phys. Rev. B **73**, 195421 (2006).

[267] B. Lazarovits, L. Szunyogh, and P. Weinberger, Phys. Rev. B **73**, 045430 (2006).

[268] N. Fischer, S. Schuppler, Th. Fauster, and W. Steinmann, Surf. Sci. **314**, 89 (1994).

[269] M. Bauer, S. Pawlik and M. Aeschlimann, Phys. Rev. B **60**, 5016 (1999)

[270] M. Wessendorf, C. Wiemann, M. Bauer, M. Aeschlimann, M. A. Schneider, H. Brune, and K. Kern, Appl. Phys. A **78**, 183 (2004).

[271] P. Nordlander and J. C. Tully, Phys. Rev. B **42**, 5564 (1990).

[272] A. G. Borisov, A. K. Kazansky, and J. P. Gauyacq, Surf. Sci. **430**, 165 (1999).

[273] J. P. Gauyacq, A. G. Borisov, and A. K. Kazansky, Appl. Phys. A **78**, 141 (2004).

[274] B. Simon, Ann. Phys. (NY) **97**, 279 (1976).

[275] N. Néel, J. Kröger, R. Berndt, and E. Pehlke, Phys. Rev. B **78**, 233402 (2008).

[276] A. G. Borisov, A. K. Kazansky, and J. P. Gauyacq, Phys. Rev. B **59**, 10935 (1999).

[277] E. V. Chulkov, V. M. Silkin, and P. M. Echenique, Surf. Sci. **437**, 330 (1999).

[278] A. K. Kazansky, A. G. Borisov, and J. P. Gauyacq, Surf. Sci. **544**, 309 (2003).

[279] J. P. Gauyacq and A. K. Kazansky, Surf. Sci. **601**, 5473 (2007).

[280] A. K. Kazansky and I. Yu. Sergeeva, J. Phys. B **27**, 3217 (1994).

[281] L. Limot, T. Maroutian, P. Johansson, and R. Berndt, Phys. Rev. Lett. **91**, 196801 (2003).

[282] J. Kröger, L. Limot, H. Jensen, R. Berndt, and P. Johansson, Phys. Rev. B **70**, 033401 (2004).

[283] F. Reinert, G. Nicolay, S. Schmidt, D. Ehm, and S. Hüfner, Phys. Rev. B **63**, 115415 (2001).

[284] M. Becker, S. Crampin, and R. Berndt, Phys. Rev. B **73**, 081402 (R) (2006).

[285] V. Simic-Milosevic, M. Heyde, N. Nilius, M. Nowicki, H.-P. Rust, and H.-J. Freund, Phys. Rev. B **75**, 195416 (2007).

[286] S.-Å. Lindgren and L. Walldén, Phys. Rev. B **22**, 5967 (1980).

[287] Jiutao Li, W.-D. Schneider, R. Berndt, O. R. Bryant, and S. Crampin Phys. Rev. Lett. 81, 4464 - 4467 (1998).

[288] J. Kliewer, R. Berndt, E.V. Chulkov, V. M. Silkin, P. M. Echenique, and S. Crampin, Science **288**, 1399 (2000).

[289] A. Eiguren, B. Hellsing, F. Reinert, G. Nicolay, E. V. Chulkov, V.M. Silkin, S. Hüfner, and P.M. Echenique, Phys. Rev. Lett. **88**, 066805 (2002).

[290] K. Watanabe, N. Takagi, and Y. Matsumoto, Chem. Phys. Lett. **366**, 606 (2002).

[291] R.W. Gurney, Phys. Rev. **47**, 479 (1935).

[292] D.M. Newns, Phys. Rev. **178**, 1123 (1969).

[293] Y. Hasegawa, and P. Avouris, Phys. Rev. Lett., 71 (1993).

[294] K. Morgenstern, K.-F.Braun, and K.-H. Rieder, Phys. Rev. Lett. **89**, 226801 (2002).

[295] H. Beckmann, and G. Bergmann Phys. Rev. Lett., 83 2417 (1999).

[296] E. N. Economou, in, *Green's Functions in Quantum Physics*, edited by M. Cardona, P. Fulde, and H.-J. Queisser, Springer Series in Solide-State Sciences Vol. 7 (Springer, Berlin, 1983).

[297] S. Crampin, J. Kröger, H. Jensen and R. Berndt, Phys. Rev. Lett. **95**, 029701 (2005).